First and second principles study of magnetic and multiferroic properties of rare-earth orthoferrites

Ali reza Sasani

Supervisors:
Dr. Eric Bousquet
Prof. Jorge Íñiguez

Jury members:
Prof. Philippe Ghosez (President)
Dr. Bertrand Dupé (secretary)
Prof. Andrea Caviglia
Prof. Andrés Cano

A Thesis Submitted for the Degree of Doctor of Philosophy at
University of Liege in Dec. 2021
Department of Physics

Acknowledgements It has been more than 4 years that I have started my Ph.D. studies, and now I am at the end of this chapter of my life. Although I had lots of ups and downs during these 4 years, in the end, I am happy with the results, since, besides scientific knowledge, I learned many things that have improved me personally and will affect all aspects of my life. During these years I have had the support and help of many people to whom, and I would like to give my gratitude.

First and foremost, I would like to give my special thanks to my supervisors, Eric Bousquet and Jorge Íñiguez. I am grateful to you both for your helpful discussions, support, and patience throughout my Ph.D. studies, thank you. I like to thank Philippe Ghosez for his discussions and help with my thesis and for creating such a great group. I also would like to give my gratitude to the members of the Phythema group, William, Sergei, Marcus, Jordan, Fabio, Daniel, Louis, Hamideh, Danila, Sebastien, Yajun, Camilo, Alexander, Wenyi. My special thanks go to He Xu for all his help during my Ph.D., especially with the TB2J code.

I spent 6 months in Luxembourg in Jorge's group. I thank him again for supporting me during this time and for all the help with administrative affairs. During this time, I met very welcoming and nice people and I like to thank them for making staying in Luxembourg much pleasant thank you, Hugo, Cosme, Monica, Mauro, Constance, Sangita, Diana, and Mael.

I would like to acknowledge my collaborators from Delft University. We have had a very good collaboration and I learned a lot. Thank you, Andrea, Jorrit, and Dima.

I also want to say special thanks to my financial support from FRS-FNRS FRIA. I also acknowledge the CECI supercomputer facilities.

I would like to give my gratitude to my parents and my family, without the help and emotional support of whom I would not be able to start and finish this journey.

Thank you all.

Abstract In this thesis, we have studied the magnetic and multiferroic properties of rare-earth orthoferrite perovskites. The main goal has been addressing the magnetic properties of this family of materials and explaining some magnetic behaviors observed in them (i.e., spin reorientation and magnetization reversal). We have started from a Heisenberg model and developed an analytical model which includes exchange interactions, Dzyaloshinskii–Moriya interactions, and SIA which is then fitted against the first-principles calculations. Using our model and classical spin dynamics we can reproduce the unique magnetic behaviors which allow us to study the origin of these behaviors. From these considerations, we have concluded that the Dzyaloshinskii–Moriya interactions between the rare-earth atoms and the transition metal atoms play the main role in creating the spin reorientation and magnetization reversal.

We have also used our model to study the magnetoelectric response in GdFeO3. Having a large and nonlinear magnetoelectric response, GdFeO3 has gained a lot of attention recently. Using our model, we can reproduce the large and nonlinear response of GdFeO3. This model was then used to study the origin of this behavior. In this study, we have shown that the non-linear nature of the magnetoelectric response in these materials comes from the fact that antiferromagnetic order changes nonlinearly under an applied magnetic field. Since the antiferromagnetic ordering of the rare-earth site creates the electric polarization, its nonlinear changes with the applied magnetic field will create a nonlinear magnetoelectric response.

Finally, we (a collaboration with Andrea Caviglia's group) have studied the magnetic phase transition in $DyFeO_3$(a member of rare-earth orthoferrites) from a completely antiferromagnetic state to a weakly ferromagnetic state induced by ultra-short laser pulses. This phase transition is very fast (in the picosecond time scale) and could have lots of technological interest, especially in the spintronics domain. In this study, we have shown that the mechanism behind this phase transition is the so-called non-linear phononics which is faster than other mechanisms like heat dissipation. In non-linear phononics, using laser pulses, it is possible to excite infra-red active phonons with a large amplitude which due to the coupling with low-frequency Raman modes, can create a magnetic phase transition.

Résumé Dans cette thèse de doctorat, nous avons étudié les propriétés magnétiques et multiferroïques des pérovskites d'orthoferrite de terres rares. L'objectif principal a été d'aborder les propriétés magnétiques de cette famille de matériaux et d'expliquer certains comportements magnétiques qui y sont observés (c'est-à-dire la réorientation de la direction des spins et l'inversion de l'aimantation en fonction de la température). Nous sommes partis d'un modéle de Heisenberg et avons développé un modéle analytique qui inclut les interactions d'échange, les interactions Dzyaloshinskii-Moriya et l'anisotropie magnétique qui sont ensuite ajustés sur des calculs ab-initio. En utilisant notre modéle et la dynamique de spin classique, nous avons pu reproduire les comportements magnétiques uniques qui nous permettent d'étudier l'origine de ces comportements. à partir de ces considérations, nous avons conclu que les interactions Dzyaloshinskii-Moriya entre l'atome de terre rare et l'atome de métal de transition jouent le rôle principal dans la création de la réorientation du spin et de l'inversion de l'aimantation.

Nous avons également utilisé notre modèle pour étudier la réponse magnétoélectrique dans $GdFeO_3$. Ayant une réponse magnétoélectrique importante et non linéaire, le $GdFeO_3$ a récemment attiré beaucoup d'attention. En utilisant notre modèle, nous pouvons reproduire la réponse large et non linéaire de $GdFeO_3$. Ce modèle a ensuite été utilisé pour étudier l'origine de ce comportement. Dans cette étude, nous avons montré que la nature non linéaire de la réponse magnétoélectrique dans ces matériaux vient du fait que l'ordre antiferromagnétique change de manière non linéaire avec un champ magnétique. Etant donné que l'ordre antiferromagnétique du site de terres rares créé la polarisation électrique, ses changements non linéaires sous champ magnétique appliqué créent une réponse magnétoélectrique non linéaire.

Enfin, nous (en collaboration avec le groupe d'Andrea Caviglia) avons étudié la transition de phase magnétique dans $DyFeO_3$ (un membre des orthoferrites de terres rares) d'un état complètement antiferromagnétique à un état faiblement ferromagnétique induit par des impulsions laser ultra-courtes. Cette transition de phase est très rapide (à l'échelle de la picoseconde) et pourrait avoir un grand intérêt technologique, notamment dans le domaine de la spintronique. Dans cette étude, nous avons montré que le mécanisme à l'origine de cette transition de phase est ce qu'on appelle la phononique non linéaire, c'est pourquoi elle est plus rapide que d'autres mécanismes comme la dissipation thermique. En phononique non linéaire, en utilisant des impulsions laser il est possible d'exciter des phonons actifs infrarouges avec une grande amplitude qui, en raison du couplage avec des modes Raman basse fréquence, peuvent créer une transition de phase magnétique. Nous avons montré que dans $DyFeO_3$, la rectification des modes Raman en conséquence du

mode d'excitation infrarouge actif modifie les interactions magnétiques entre les terres rares et le fer et crée une transition de phase magnétique.

Contents

Acknowledgements ii

Abstract iii

Résumé iv

1 Theoretical considerations 1
- 1.1 Magnetism . . . 1
  - 1.1.1 Intra-atomic exchange and atomic magnetic moments . . . 3
  - 1.1.2 Inter atomic exchange models . . . 7
  - 1.1.3 Other types of exchange interactions . . . 10
  - 1.1.4 Magneto crystalline anisotropy . . . 12
  - 1.1.5 Dzyaloshinskii–Moriya interaction . . . 14
  - 1.1.6 Magnetization in materials . . . 15
  - 1.1.7 Modeling magnetic materials . . . 17
- 1.2 Many body interacting particles . . . 19
  - 1.2.1 Solving Schrödinger equation . . . 20
  - 1.2.2 Density functional theory (DFT) . . . 23
  - 1.2.3 Exchange and correlations . . . 25
  - 1.2.4 Orbital dependent functionals: LDA +U . . . 27
  - 1.2.5 Relativistic interactions in DFT . . . 28
  - 1.2.6 Density functional perturbation theory (DFPT) . . . 29
  - 1.2.7 Practical implementation of DFT . . . 30
- 1.3 Calculation of magnetic interactions . . . 31
  - 1.3.1 Total energy mapping . . . 32
  - 1.3.2 Calculation of the magnetic interactions using the local force theorem 34
- 1.4 Conclusion . . . 35

2 Physics of rare-earth orthoferrites 37
- 2.1 Introduction . . . 37
- 2.2 Atomic structure of orthoferrites . . . 38
- 2.3 Magnetic properties . . . 41
  - 2.3.1 Magnetic structures . . . 41
  - 2.3.2 Magnetization reversal . . . 44
  - 2.3.3 Spin reorientation . . . 44
  - 2.3.4 Magnetization hysteresis loops . . . 48
- 2.4 Magnetoelectric and multiferroic properties . . . 49
- 2.5 Conclusion . . . 55

3 Magnetic phase diagram of rare-earth orthorhombic perovskite oxides 56
3.1 Introduction . . . 56
3.2 Analytical model . . . 57
3.2.1 Symmetry-adapted spin representation . . . 57
3.2.2 Heisenberg model . . . 59
3.3 Calculation of the magnetic interaction parameters . . . 61
3.3.1 Superexchange and DMI parameters . . . 61
3.3.2 Origin of ordering on R site . . . 64
3.4 Spin dynamics . . . 65
3.4.1 Γ_4 to Γ_2 reorientation . . . 66
3.4.1.1 Parameters affecting the Γ_4 to Γ_2 SR . . . 70
3.4.1.2 The Γ_4 to Γ_2 rotation in finite temperature window . . . 73
3.4.1.3 Effect of SIA on Γ_4 to Γ_2 SR . . . 75
3.4.1.4 Summary for the Γ_4 to Γ_2 transition . . . 75
3.4.2 Γ_4 to Γ_1 reorientation: . . . 76
3.5 Conclusion . . . 79

4 Origin of nonlinear magnetoelectric response in GdFeO3 81
4.1 Introduction . . . 81
4.2 Theoretical derivation . . . 82
4.3 Simulations . . . 87
4.3.1 Magnetic fields perpendicular to the Gd G-type order direction . . . 87
4.3.2 ME response for magnetic field parallel to the Gd G-type order . . . 90
4.4 Conclusion . . . 91

5 Light-driven ultrafast phonomagnetism in $DyFeO_3$ 94
5.1 Introduction . . . 94
5.2 Ground state calculation . . . 96
5.3 Phonons . . . 97
5.4 Laser phonon interaction . . . 100
5.5 Phonon-phonon interaction . . . 101
5.6 Phonon dynamics . . . 104
5.7 Phonon-magnetism interaction . . . 106
5.8 Nature of spin reorientation . . . 108
5.9 Conclusion . . . 112

6 Concluding remarks 113

Publications list 116

A Derivation of Heisenberg model 117

B Technical details 125
B.1 Chapter 3 . . . 125
B.2 Chapter 4 . . . 126
B.3 Chapter 5 . . . 127

C f electrons ground state **129**

D Phonons **131**
D.1 Phonons of $GdFeO_3$ for different magnetic ordering of Fe 131
D.2 Phonons of $DyFeO_3$ 131

Bibliography **135**

Chapter 1

Theoretical considerations

1.1 Magnetism

Magnetism was discovered in the ancient world when people noticed the attraction of iron to Lodestone [1], since then, this phenomenon has been a mystery. In 1820, Ørsted accidentally found an interaction between electricity and magnetism and discovered that an electric current can create a magnetic field[2]. Following Ørsted's discovery, several other scientists discovered different relations between electricity and magnetism. By the second half of the nineteenth century, Maxwell's equations established a solid foundation to explain most of the phenomena that we observe in nature by uniting all the knowledge that mankind had regarding electricity and magnetism thus far[3].

Although mankind had a great understanding of electricity and magnetism, the origin of magnetism in materials was still a mystery. The first attempt to explain the magnetism in the material was based on the dipole moments that are resulted from circular electronic current, and the dipole-dipole interaction between these moments. This model was not successful in explaining the high-temperature magnetism observed in materials (since these interactions are very weak to survive in observed magnetic ordering temperature). A correct explanation of magnetism in materials had to wait until the twentieth century and the formulation of quantum mechanics. Since magnetism has a quantum origin, quantum mechanics is needed for it to be explained.

Magnetic interactions in the material have different origin and these become important at various temperatures and result in different properties. These interactions can be divided into different groups based on their magnitude. In Fig. 1.1 we are showing different magnetic interactions magnitudes. The exchange energy that creates the magnetic moments in atoms (with a magnitude of $\sim$1 eV) shown on the right-hand side of the

Fig. 1.1, is one order of magnitude larger than the interactions that order these moments in materials (with a magnitude of ∼0.1 eV shown on the middle part of the Fig. 1.1). The interactions that have a relativistic origin, like magnetocrystalline anisotropy, are in the μeV range (These are at the left-hand side of the Fig. 1.1). Since the interactions that create atomic moments are very large, we can consider the magnetic moments of the atoms as constant in the temperature range that we are interested in. The magnetic behaviors and properties that we study are coming mainly from the rotation and ordering of these atomic moments.

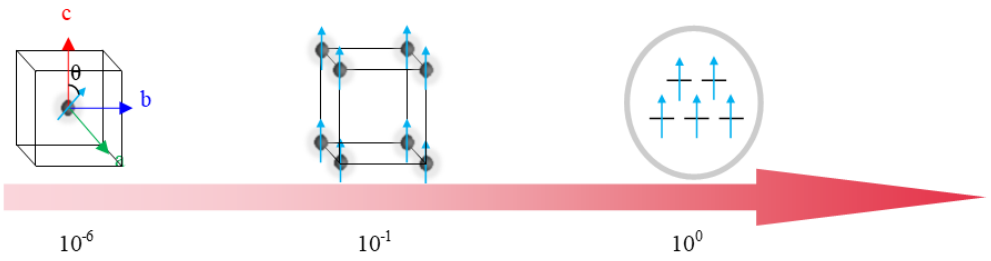

FIGURE 1.1: Magnitude of different magnetic interactions (the units are eV). On the right hand side there is magnetic moment formation in atoms where the exchange interaction magnitude is in ∼eV order. In the middle, there is the exchange interaction between atoms with ∼0.1 eV order. At the left hand side, the interactions which have spin orbit coupling as their origin are positioned with ∼ μeV order.

We need to mention that, although we are considering atomic magnetic moments constant in this work, there are structures and atoms in which this is not the case. In these structures, the crystal field splitting (Crystal field is a static electric field produced by a surrounding charge of anion atoms) of the atomic levels are larger compared to exchange interactions. For such compounds, the high spin ordering which is favored by exchange interaction has higher energy due to the large energy difference created by the crystal field of the structure. In these structures, the electrons transform from high spin to low spin, which changes the total magnetic moment of the atoms [see Fig. 1.2].

In this section, we are going to give a brief overview of magnetism and its quantum mechanical origin. To develop the models to describe the magnetic behaviors of the materials, we will start from intra-atomic exchanges to explain the origin of the formation of magnetic moments in atoms. Then we will continue to present exchange interaction models in materials that can be used to describe Long-range order and different magnetic properties of the materials resulting from atomic magnetic moments. In this section, the main idea is to define different terminology and parameters that we need and the simple derivation and origin of these parameters, since already there is a good number of literature devoted to complete derivation of these parameters.

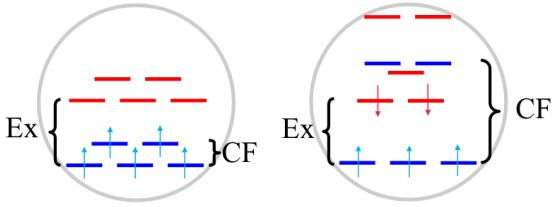

FIGURE 1.2: Schematic presentation of high spin (left) to low spin (right) transition for d^5 orbitals. The red lines show the energy levels for down spins while the blue lines show the energy levels for up spins. On the left, the atom is in the high spin state with all the spins ordering in the same direction (Splitting of the energy levels due to exchange interaction and crystal field are shown by Ex and CF respectively). On the right, the crystal field has split the levels more than exchange interaction between electrons and has made a transition from high spin to low spin state.

1.1.1 Intra-atomic exchange and atomic magnetic moments

To study the origin of atomic magnetic moments, we are going to start by introducing atomic energy levels and orbitals. The simplest model to describe atomic levels and orbitals is the hydrogenic atom. In this model, we need to solve the Schrödinger equation for a hydrogenic atom. The Schrödinger equation for hydrogenic atom can be developed as Eq. 1.1 (we are considering the equation in atomic units):

$$-\frac{1}{2}\nabla^2\phi_n(r) - \frac{Z}{r}\phi_n(r) = E_n\phi_n(r) \tag{1.1}$$

Where Z is an effective nuclear charge and ∇^2 is the second derivative with respect to space coordinates and $\phi_n(r)$ is a single particle wave function. Solving this equation will give the spatial distribution of electronic wave functions (i.e., $\phi_n(r)$) and their corresponding energy levels (i.e., E_n).

Solving this equation will give the wavefunction of the following form:

$$\phi_n(r,\Theta,\varphi) = R_{nl}(r)Y_{lm}(\Theta,\varphi) \tag{1.2}$$

where n, l, m are quantum numbers describing the wavefunctions. The $R_{nl}(r)$ describes the radial dependence of the wavefunctions and the $Y_{lm}(\Theta,\varphi)$ gives the angular dependence of the wavefunctions.

Eigenvalues of this equation are atomic shells with principal quantum number n with energy:

$$E_n \propto -\frac{1}{n^2} \qquad (n = 1, 2, 3, ...) \tag{1.3}$$

and each energy level has a shell with n^2 degeneracy. To label these degenerate levels, l and m quantum numbers are used. Each shell has n sub shells (e.g., n=3 : s($l = 0$), p($l = 1$), d($l = 2$)) and each of these sub shells in turn has $2l + 1$ states ($m = -l, -l + 1, ..., l + 1, l$). The values of m in these wave functions are proportional to the orbital angular magnetic moment of the electron.

In Fig .1.3, we are presenting schematics of atomic wave functions with different l and m. For $l = 0$ (s orbitals), there is only $m = 0$ for which the orbital angular momentum is zero (red orbital in Fig. 1.3). For $l = 1$ (p orbitals), m can have $m = -1, 0, 1$ which is presented by p_y, p_z, p_x corresponding to orbitals with angular momentum of -1,0,1 (yellow orbitals in Fig. 1.3). The same principle applies to other shells such as d and f orbitals as shown in Fig. 1.3. These orbitals and shells are the basis on which more complex and multi-electron atoms can be described. Filling these orbitals with more than one electron follows the Pauli exclusion principle. This principle is guaranteed if the many-particle wavefunctions are written anti-symmetric with respect to the exchange of particles (i.e, the sign of the wavefunctions will change if we exchange two particles).

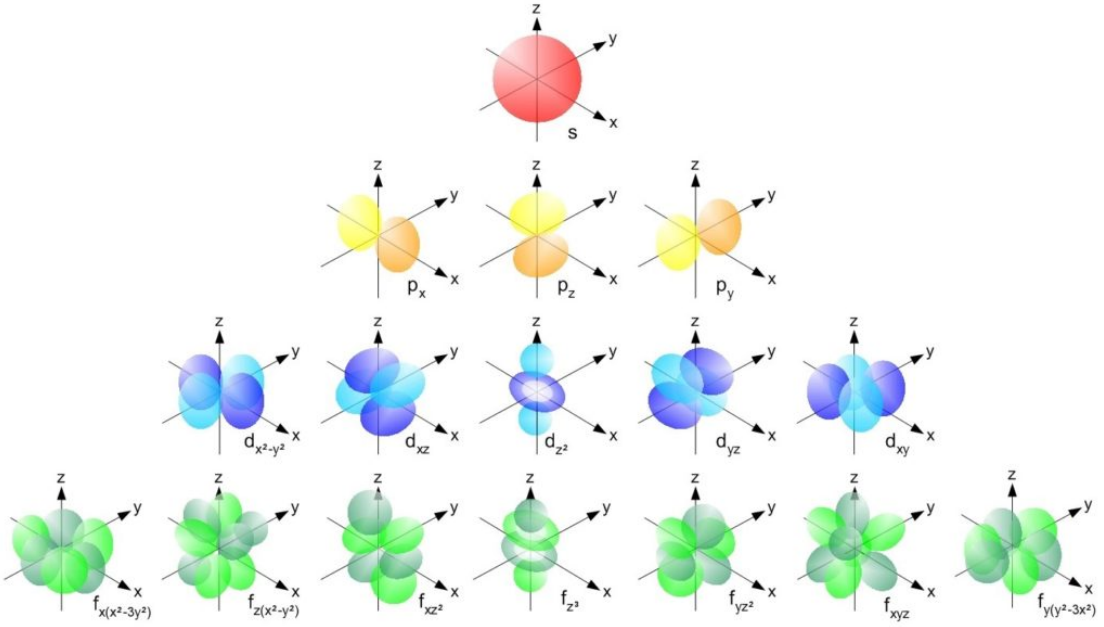

FIGURE 1.3: Schematic presentation of atomic orbitals for s (red sphere), p (yellow orbitals), d (blue orbitals) and f (green orbitals) (Figure adapted from [4]).

When there are more than one electron in an atom, the Schrödinger equation must include the coulomb interaction between electrons too. So the Schrödinger equation for a two electron atom is written as:

$$-\frac{1}{2}\nabla^2\psi(r_1, r_2) + V_c(r_1, r_2)\psi(r_1, r_2) - \frac{Z}{r}\psi(r_1, r_2) = E\psi(r_1, r_2) \tag{1.4}$$

where V_c is the Coulomb interaction between two electrons. Solving this equation is a demanding and most of the time impossible task. The first step to solve this equation is to use approximation to many-particle wavefunction (i.e., $\psi(r_1, r_2)$). One common method is to consider $\psi(r_1, r_2)$ as a product of single-particle wavefunctions (i.e., $\psi(r_1, r_2) = \phi_1(r_1)\phi_2(r_2)$). Since this product should agree with the Pauli exclusion principle, these products should be symmetrized. Writing Slater determinant of the single-particle wavefunctions solves this inconsistency and gives wavefunctions that are consistent with the Pauli exclusion principle (to be discussed in sec 1.2).

According to the Pauli exclusion principle, no electrons can have the same quantum numbers in an atom. This means that there can be two electrons in the same orbital only with different spins. So, for a two-electron atom, When one electron fills an orbital, the second electron can have two possible choices. How the electrons fill the orbitals [either Fig. 1.4 (a) or Fig. 1.4 (b)] is determined by exchange interaction between electrons. This interaction is coming from the fact that the wave function describing these states should be antisymmetric (Pauli exclusion principle). The energy difference between two cases (i.e., Fig. 1.4 (a) and Fig. 1.4 (b)) is called exchange interaction and it is defined as:

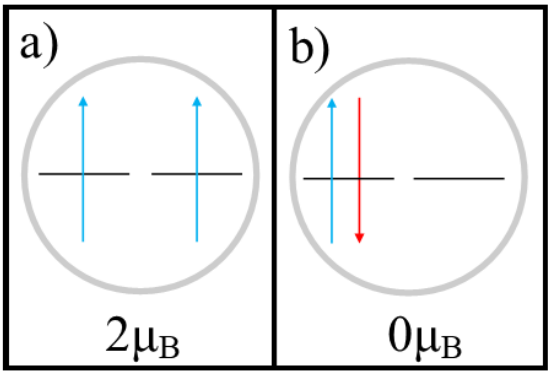

FIGURE 1.4: Schematic representation of the electrons filling degenerate orbitals in an atom. a) Parallel spins (↑↑) state. b) Antiparallel spins (↑↓)

$$E_{ex} = (E\uparrow\uparrow - E_{\uparrow\downarrow})/2 \tag{1.5}$$

Because each electron has an intrinsic magnetic moment (i.e., spin), this shows that either the magnetic moment from two electrons in an atom would be $2\mu_B$ ($E_{ex} < 0$, Fig. 1.4 (a)) or zero ($E_{ex} > 0$, Fig. 1.4 (b)). To calculate the exchange interaction for a two electron system, we need to solve Schrödinger equation for two particle system (i.e., Eq.1.4) in two electronic configurations (i.e., ↑↑ and ↑↓). In this case the exchange interaction in an atom (as defined in 1.5) with two electron can be written as:

$$J_{ex}^{at} = \iint \phi_1^*(r,\sigma)\phi_2^*(r',\sigma')V_c\phi_1(r',\sigma')\phi_2(r,\sigma)dVdV' \tag{1.6}$$

Where V_c is the Coulomb repulsion between two electrons and $\phi_i(r,\sigma)$ is a single particle state for an electron at position r with spin σ. This interaction is coming from considering the electronic wavefunction as Slater determinants. This interaction is zero for electrons with opposite spin direction while non zero for the electrons with spins in the same direction. This interaction has an opposite sign compared to Coulomb interaction and lowers the energy which forces the electrons to fill different orbitals with the same spin. This interaction is at the origin of observed magnetic moments in atoms. So, when electrons fill the orbitals, they will fill different degenerate levels (e.g., for l=2, $m_l = -2,-1,0,1,2$) with the same spin direction, and then the magnetic moment will be the sum of the spin magnetic moments and orbital magnetic moments of all the electrons.

The magnetism of the atoms is mainly coming from d ($l=2$) or f ($l=3$) orbitals. Each electron occupying these levels will have an orbital angular magnetic moment m and a spin magnetic moment s. Since these two have angular momentum characters, we can use vector algebra to define a total magnetic moment for an atom coming from the sum of orbital and spin magnetic moments. There are two approaches to calculate the total magnetic moment of an atom that has more than one electron (i.e., Russel-Saunders coupling and jj coupling). Depending on the magnitude of the spin-orbit interaction (SOI), either of these two schemes can be used. SOI is an interaction with relativistic origin and couples l and s magnetic moments through a term which is proportional to $l.s$ [see 1.2.5]. When SOI is not very strong, the first coupling scheme is used (i.e., the L-S or Russel-Saunders coupling scheme). In this scheme, the total orbital moments and spin moments of an atom are calculated separately and summed to give the atomic magnetic moment. The total orbital moment is $L = \sum_i l_i$ for electrons filling this orbital and the total spin moment is $S = \sum_i s_i$, from which the total atomic moment can be calculated as $J = L + S$.

For heavy atoms, where there is a strong SOI, the Second method is used to calculate the moments of the atoms (i.e., jj scheme). The total moment of the atoms in this model is $J = \sum_i j_i$ where j_i is the total magnetic moment of each electron in the atom with $j_i = \sum_i L_i \pm \frac{1}{2}\hbar$ for each electron ($\pm$ shows the direction of spin with respect to orbital angular momentum).

Studying material has shown that for most of the structures we have $J \approx S$. This shows that the J of an atom does not have any L component. This phenomenon is called angular momentum quenching. This is arising from the fact that the crystal field will mix the wave functions to form standing waves. These standing waves are linear combinations of different orbitals with different angular momentum. This mechanism

forces wave functions of the form $|+2> + |-2>$ to be formed for electrons where $|\pm 2>$ are wave functions with angular momentum ± 2. This would make the expectation value of angular momentum for this wave function zero since its angular momentum will be the sum of the angular momentum of the two components of the wave function (i.e., $|\pm 2>$). This quenching competes with the spin-orbit coupling which can cause unquenching of the angular momentum.

When put in a magnetic field, the electrons will behave according to the Zeeman interaction. The Zeeman theory states that the energy of the electron in a magnetic field is:

$$E_z = g\mu_0\mu_r S.H_{ext} \tag{1.7}$$

where g is called the *landé g* factor, μ_0 is the vacuum permeability and μ_r is the relative permeability of the material. The g is a proportionality constant between the Zeeman energy and the applied magnetic field (H_{ext}) multiplied by magnetic moment (S) as:

$$g = \frac{E_z}{\mu_0\mu_r S H_{ext}} \tag{1.8}$$

The g is equal to 2 for pure spins and 1 for pure orbital moment. But when we consider coupled spin and orbital moment (i.e J), the *landé g* factor for J should be projected to $L + S$. The *landé g* factor for atomic moment $J = L + S$ is equal to:

$$g_J = \frac{3}{2} + \frac{1}{2}\frac{S(S+1) - L(L+1)}{J(J+1)} \tag{1.9}$$

So that the energy of an atom with J moment in the magnetic field would be

$$H_z = g_J\mu_0\mu_r J H_{ext} \tag{1.10}$$

In this part, we have presented the origin of ionic magnetic moment and how to calculate the total magnetic moment of an atom, we will continue by presenting models that describe the interactions of these moments in materials that create long-range orders in materials.

1.1.2 Inter atomic exchange models

To develop a model to describe the exchange interaction between atomic moments in a material, we will start by introducing appropriate Hamiltonian and wave functions to

be used in deriving the formulas for a two-atom model. If we consider our model to be as represented in Fig. 1.5 (a), we can write the Schrödinger equation for this model as:

$$\begin{aligned} &-\sum_{i=1}^{2}\frac{1}{2}\nabla_i^2\psi(r_1,r_2)+V_c(r_1-r_2)\psi(r_1,r_2)\\ &+\sum_{I,i}V_{eI}(r_i-R_I)\psi(r_1,r_2)=E\psi(r_1,r_2) \end{aligned} \tag{1.11}$$

Where V_c is the electron electron Coulomb interaction and V_{eI} is the nuclei electron interaction. $\psi(r_1, r_2)$ is the two electron wave function and it can be written as a linear combination of the products of two single electron wave function (i.e., $\phi_i(r)$). If we consider our single electron wave functions to be orthonormal (i.e., $< \phi_1(r_1)|\phi_2(r_2) >= \delta_{1,2}$, Wannier like wave functions), then we can write our state as:

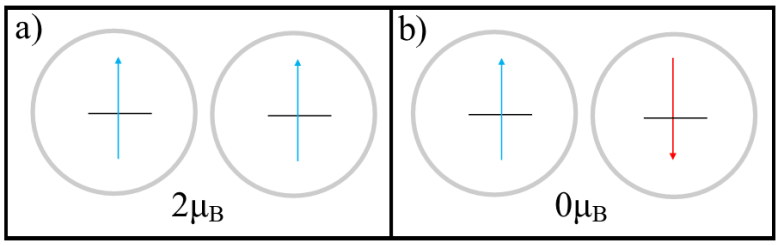

FIGURE 1.5: Schematic representation of magnetic ordering in a two atom model. a) Ferromagnetic ordering, b) Antiferromagnetic ordering

$$\psi(r_1,r_2)=c_1\phi_1(r)\phi_1(r')+c_2\phi_1(r)\phi_2(r')+c_3\phi_2(r)\phi_1(r')+c_4\phi_2(r)\phi_2(r') \tag{1.12}$$

In this equation $\phi_1(r)\phi_1(r')$ and $\phi_2(r)\phi_2(r')$ represent electrons in the same orbital with opposite spins (Fig. 1.5 (b)), while $\phi_1(r)\phi_2(r')$ and $\phi_2(r)\phi_1(r')$ represent two electrons in different atoms (Fig. 1.5 (a)). To solve the Schrödinger equation for this system we will define following parameters: The on-site Coulomb interaction between two electrons is defined as:

$$U=\iint \phi_1(r)^*\phi_1(r')^*V_c(r,r')\phi_1(r)\phi_1(r')dVdV' \tag{1.13}$$

while the exchange interaction is defined by J_D as:

$$J_D=\iint \phi_1(r)^*\phi_2(r')^*V_c(r,r')\phi_2(r)\phi_1(r')dVdV' \tag{1.14}$$

and we define the transfer integral or hopping integral as:

$$t = -\frac{1}{2}\iint \phi_1(r)^*\phi_2(r')^*\nabla^2\phi_1(r)\phi_2(r')dVdV' \tag{1.15}$$

If we solve the Schrödinger equation, Eq. 1.11, with Eq. 1.12 as wavefunction, and using the parameters Eq. 1.13, Eq. 1.14 and Eq. 1.15 we can write it as:

$$H = 2E_0 + \begin{pmatrix} U & t & t & J_D \\ t & 0 & J_D & t \\ t & J_D & 0 & t \\ J_D & t & t & U \end{pmatrix} \tag{1.16}$$

By diagonalising this Hamiltonian (Eq.1.16) we can write its eigenstates as:

$$|1>= \frac{1}{\sqrt{2}}\left(\phi_1(r)\phi_2(r') - \phi_2(r)\phi_1(r')\right) \tag{1.17}$$

Where electron one is in one atom and electron two is on the other one. Since the wavefunction is antisymmetric we will have symmetric spin functions (i.e., ferromagnetic)

$$|2>= \frac{1}{\sqrt{2}}\left(\phi_1(r)\phi_1(r') - \phi_2(r)\phi_2(r')\right) \tag{1.18}$$

In this state, electron one and electron two are located on the same atom and the wave function is symmetric which forces the electrons to have an antiferromagnetic state (due to Pauli's exclusion principle).

$$\begin{aligned} |3> \; &= \frac{sin(\chi)}{\sqrt{2}}\left(\phi_1(r)\phi_1(r') + \phi_2(r)\phi_2(r')\right) \\ &+ \frac{cos(\chi)}{\sqrt{2}}\left(\phi_1(r)\phi_2(r') + \phi_2(r)\phi_1(r')\right) \end{aligned} \tag{1.19}$$

$$\begin{aligned} |4> \; &= \frac{cos(\chi)}{\sqrt{2}}\left(\phi_1(r)\phi_1(r') + \phi_2(r)\phi_2(r')\right) \\ &- \frac{sin(\chi)}{\sqrt{2}}\left(\phi_1(r)\phi_2(r') + \phi_2(r)\phi_1(r')\right) \end{aligned} \tag{1.20}$$

with $tan(2\chi) = -4t/U$. In the states $|3>$ and $|4>$, since the wavefunctions are symmetric the spins are going to be antisymmetric (i.e., antiferromagnetic states) . The corresponding eigenvalues for these states are:

$$E_1 = 2E_0 - J_D \tag{1.21}$$

$$E_2 = 2E_0 + U - J_D \tag{1.22}$$

$$E_3 = 2E_0 + \frac{U}{2} + J_D - \sqrt{4t^2 + \frac{U^2}{4}} \tag{1.23}$$

$$E_4 = 2E_0 + \frac{U}{2} + J_D + \sqrt{4t^2 + \frac{U^2}{4}} \tag{1.24}$$

Now that we have the energies for different states, we can calculate the exchange according to its definition (i.e $\frac{1}{2}(E_3 - E_1)$):

$$J_{ex}^{dir} = J_D + \frac{U}{4} - \sqrt{t^2 + \frac{U^4}{16}} \tag{1.25}$$

Although a very simple model is used to derive the exchange interaction, it explains quite well the exchange interaction in more complex systems. This exchange is called *direct exchange* interaction.

In the equation 1.25, among the parameters defining the exchange interaction between two atoms, J_D is small compared to U and t, while, U and t are on the same order. This is because J_D is proportional to the overlap of the orbitals on two different atoms (i.e., $\phi_1(r)^*\phi_2(r)$) while U and t are proportional to the square of the wavefunctions (i.e., charge density $\phi_1(r)^*\phi_1(r)$). Since U and t are on the same order, their relative magnitude can determine the magnetic ordering of the system. Fig. 1.6 shows the relative change of different eigenstates energies of the model as a function of the t parameter. As can be seen in the figure 1.6, for low values of t, the model prefers to be in Ferromagnetic state (state $|1>$), while as t value increases, we can see a particular transition point where the antiferromagnetic state (state $|3>$) becomes lower in energy and becomes the stable state of the model.

1.1.3 Other types of exchange interactions

The exchange interaction developed in the previous section describes the exchange interaction when two atoms are neighbors and it is a direct exchange. *Superexchange* (SE) interaction is the exchange interaction between magnetic ions separated by a ligand atom [see Fig. 1.8]. This exchange was discovered by Kramers in 1934 [6]. The superexchange

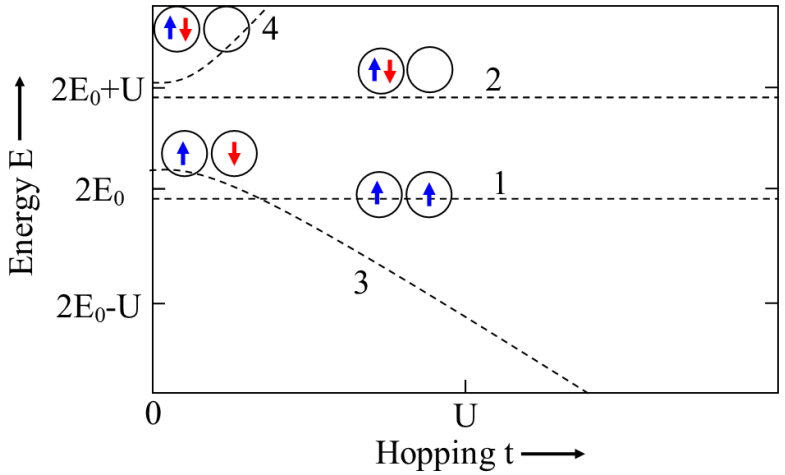

FIGURE 1.6: Energy of different states as a function of Hopping parameter t. The states $|1>$ and $|2>$ are independent of the t parameter, while for states $|3>$ and $|4>$ the energy changes. The two spheres showing the state of the spin in the two atoms model [5].

interaction has been derived analytically by Anderson using second-order perturbation of the exchange [7]. In his work he has shown that this interaction can be written as:

$$J_{ex}^{SE} = \frac{2t^2}{U} \tag{1.26}$$

where t is the transfer between two orbitals defined as:

$$t = -\frac{1}{2}\iint \phi_1(r)^*\phi_2(r')^*\nabla^2\phi_1(r)\phi_2(r')dVdV' \tag{1.27}$$

and U is the on-site Coulomb repulsion of the electrons or Hubbard interaction defined as:

$$U = \iint \phi_1(r)^*\phi_1(r')^*V_c(r,r')\phi_1(r)\phi_1(r')dVdV' \tag{1.28}$$

The U and t in this exchange are similar to direct exchange but the difference is in the single-particle wavefunctions that Anderson has defined. These wave functions are mixed with ligand atoms wave functions and are orthonormal to each other. Superexchange is antiferromagnetic when there is overlap between orbitals and becomes ferromagnetic when the overlap is zero; in this case, the exchange is of direct exchange type (Kanamori-Goodenough-Anderson rules).

Double exchange is also a different mechanism of exchange. This type of exchange is responsible for the magnetization of systems with different valence charge (e.g., Fe^{+2}

and Fe^{+3} in Fe_3O_4). This interaction is coming from an extra electron that can move from one atom to another, hence creating a direct interaction between atoms which results in ferromagnetic exchange interaction. This interaction is similar to the exchange interaction proposed by Zener [8].

Similar to double exchange, there are also interactions of magnetic ions placed into a conducting electrons gas with Fermi wavevector k_F. This mechanism is studied by Ruderman, Kittel, Kasuya, and Yosida [9–11]. They have shown that this interaction can result in an exchange with the following relation:

$$J(R)^{rkky} = J_0 \frac{2K_F R cos(2k_F R) - sin(2k_F R))}{(2k_F R)^4} \tag{1.29}$$

Where R is the distance between two magnetic ions. This interaction has an oscillatory dependence on the distance between two atoms.

1.1.4 Magneto crystalline anisotropy

The models that have been developed in the previous part are not complete and they are not capable of describing some of the magnetic properties of materials that have been observed experimentally (Hysteresis and coercivity). To extend the model we need to include some other interactions. One such interaction is the magnetocrystalline anisotropy (MCA) (i.e the dependence of the magnetic energy on the direction of the magnetization with respect to crystalline direction). The main mechanism responsible for MCA is the interaction between crystal field and the spin through spin-orbit coupling [12]. The same mechanism is also explaining the orbital moment and magnetoelasticity and magnetoresistance.

A model to study the directional dependence of magnetism in materials is through the phenomenological modeling of MCA. The simplest phenomenological model to capture directional dependence of the magnetism in materials is using the following equation:

$$E_a = K_1 Sin^2(\theta) \tag{1.30}$$

Where K is the anisotropy constant and θ gives the angle between the easy axis in crystalline direction and spin direction [see fig. 1.7]. In this model, $K_1 > 0$ gives easy-axis type material in which the magnetic direction is in $\theta = 0$, while $K_1 < 0$ gives easy plane type magnetization where the magnetic moments of the materials order in a plane in $\theta = \pi/2$ and it is free to rotate in this plane.

To make the model more complete, we can include the dependence of the magnetic energy on azimuths angle [See figure 1.7 for the definition of the angles]. The Eq. 1.30 that is describing the MCAs has uniaxial symmetries and to extend this model to include non-uniaxial symmetries we can use the equation:

$$E_a = (K_1 sin^2(\theta) + K_1' sin^2(\theta) cos(2\phi) \tag{1.31}$$

This equation is more general 2nd order phenomenological MCA model and can be used to describe crystal structures with lower symmetries. In this equation also for $K_1 > 0$, the system will be of easy axis type while $K_1 < 0$ would result in anisotropy in the basal plane.

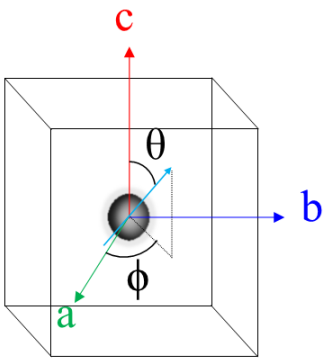

FIGURE 1.7: Caricature of the SIA direction and definition of the angles (θ and ϕ) with respect to crystallographic direction.

The Eq. 1.30 and Eq. 1.31 are the lowest order of the MCA. By including higher orders, we can describe more complicated MCA's. By including terms to order 6 we will have the following equation as a model to describe the MCA.

$$E_a = K_1 Sin^2(\theta) + K_2 Sin^4(\theta) + K_3 Sin^6(\theta) \tag{1.32}$$

A point to notice in these equations is that the functions are not orthogonal and if we transform these to orthogonal functions (ex. spherical harmonics) we will have different orders.

In addition to mentioned anisotropy sources, we can also have anisotropy in exchange interaction. This anisotropy is due to spin-orbit coupling and would result in having $J_{xx} S_i^x . S_j^x$, $J_{yy} S_i^y . S_j^y$, and $J_{zz} S_i^z . S_j^z$ with different energy, which would make the spins to order in the energetically favored direction.

Finally, magnetic dipole interaction also can result in anisotropy. This anisotropy is called shape anisotropy and would cause a directional dependence of the magnetism on the macroscopic scale.

1.1.5 Dzyaloshinskii–Moriya interaction

In the 1950s, scientists were confused by the presence of a weak magnetism in some of the antiferromagnetic compounds. The first explanations for this weak magnetization were made to be originating from impurities [13]. In 1958 Dzyaloshinskii showed that free energy and symmetry allow some interactions of the following from [14]:

$$E_{\mathrm{DMI}} = D_{ij}.(S_i \times S_j) \tag{1.33}$$

and using this mechanism he proved that the weak magnetic present in antiferromagnetic compounds is due to interactions of this type.

In 1960 Moriya used perturbation theory and extended the formalism of Anderson in which he included second-order perturbation of bi-linear form of spin-orbit interactions and exchange [15]. In this work, he showed that the interaction proposed by Dzyaloshinskii can be written as:

$$\begin{aligned} E_{DMI} =& 2i\lambda \left(\sum_{m} \frac{J(nn'n'm) < n|l_1|m >}{E_n - E_m} - \sum_{m'} \frac{J(nn'm'n) < n'|l_2|m' >}{E_{n'} - E_{m'}} \right) \\ & .[S_1 \times S_2] \end{aligned} \tag{1.34}$$

Which can be written as Eq. 1.33 with D_{ij} between atom 1 and 2 as:

$$D_{12} = 2i\lambda \left(\sum_{m} \frac{J(nn'n'm) < n|l_1|m >}{E_n - E_m} - \sum_{m'} \frac{J(nn'm'n) < n'|l_2|m' >}{E_{n'} - E_{m'}} \right) \tag{1.35}$$

This equation is written for a model like the one presented in Fig. 1.8 in which n and n' are filled states and m and m' are empty states of the atom 1 and atom 2. l_i is the orbital magnetic moment of the atom i and $J(nn'm'n)$ can be written in terms of hopping parameter t and coulomb repulsion U as:

$$J(nn'n'm) = t_{nn'}t_{m'n}/U \tag{1.36}$$

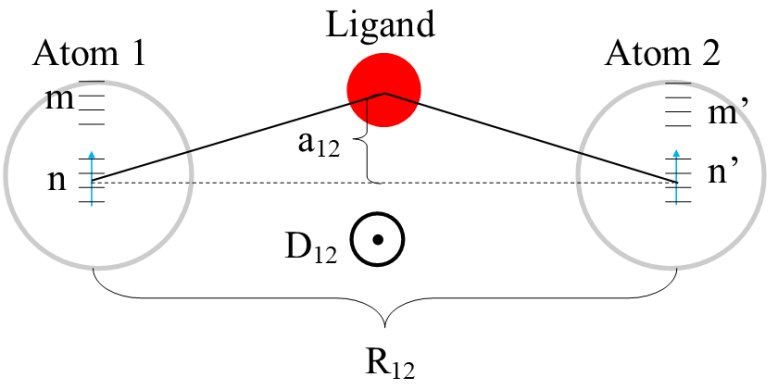

FIGURE 1.8: Schematic presentation of two atom model to calculate superexchange and DMI. n and n' showing filled states in atom 1 and atom 2 while m and m' are presenting empty states. R_{12} is a vector from atom 1 to atom 2 and a_{12} is a vector presenting displacement of the ligand atom from the center of bond. D_{12} is the DMI vector direction coming out of the plane.

This interaction is named after Dzyaloshinskii and Moriya as Dzyaloshinskii–Moriya interaction (DMI). The DMI is another source of magnetic anisotropy in magnetic materials.

Using symmetry, it is also possible to determine D_{ij} from Eq. 1.33 up to a proportionality constant. From this analysis, it is shown that this parameter can be written as:

$$D_{ij} = \eta R_{ij} \times a_{ij} \tag{1.37}$$

Where R_{ij} is a vector from atom i to atom j and a_{ij} is the vector from center of the R_{ij} to ligand atom and η determines magnitude of this interaction [See Fig. 1.8]. This interaction favors putting spins perpendicular to each other and is in competition with exchange interaction.

1.1.6 Magnetization in materials

Magnetic materials are classified based on their response to an external magnetic field. When exposed to magnetic field H, magnetic induction B is the response of a material. The H and B, both vector fields, are proportional to each other as:

$$B = \mu_0(H + M) \tag{1.38}$$

In this equation, M is the average magnetic moment per unit volume of the material and it is defined as:

$$M(r) = \frac{\langle m \rangle_V}{V} \tag{1.39}$$

where the average indicates that we average over all atomic magnetic moments in a small volume V around position r.

The response of a magnetic material, i.e., magnetization M and induction B, can be written as the following equations with magnetic susceptibility χ and the permeability μ as constants of proportionality:

$$M = \chi H \tag{1.40}$$

$$B = \mu H \tag{1.41}$$

where we are considering the simplest expressions for the case where all fields are collinear, static (that is, independent of time), and homogeneous in space (q=ω=0). In general, however, the response functions are tensor, i.e. $M_i = \sum_j \chi_{ij} H_j$, and depend on frequency ω. From Eq. 1.38, we can write the relation between susceptibility and permeability as:

$$\mu_r = \frac{\mu}{\mu_0} = 1 + \chi \tag{1.42}$$

μ_r, the relative permeability, is dimensionless and equals unity in free space.

The quantities defined in Eq. 1.40 and Eq. 1.41, can be functions of temperature and magnetic field H. Based on how the χ changes as a function of magnetic field, the materials are classified as being:

- Diamagnetic
- Paramagnetic
- Antiferromagnetic
- Ferromagnetic and Ferrimagnet

In diamagnetic materials χ has a negative value and magnetization is in opposite direction to the applied magnetic field. In paramagnetic and antiferromagnetic materials the χ is linear and the magnetization is in the same direction with the applied magnetic field and the magnetization disappears when the magnetic field is removed. In paramagnetic

materials, the atomic magnetic moments are ordered randomly, and upon application of the magnetic field, they start to order. In antiferromagnetic materials, the atomic magnetic moments are ordered in an anti-parallel fashion and upon application of magnetic field, they will rotate to the direction of the applied magnetic field. In the fourth class of materials, magnetization is a nonlinear function of the magnetic field. For ferromagnets (materials where the atomic moments are aligned in the same direction) and ferrimagnets (where magnetic moments are aligned in opposite directions with different magnetic moments), the magnetization increases nonlinearly by increasing the magnetic field and becomes constant when reaches saturation. For these materials when the magnetic field is lowered to zero, a remnant magnetization survives with finite value (This is called Hysteresis Behavior).

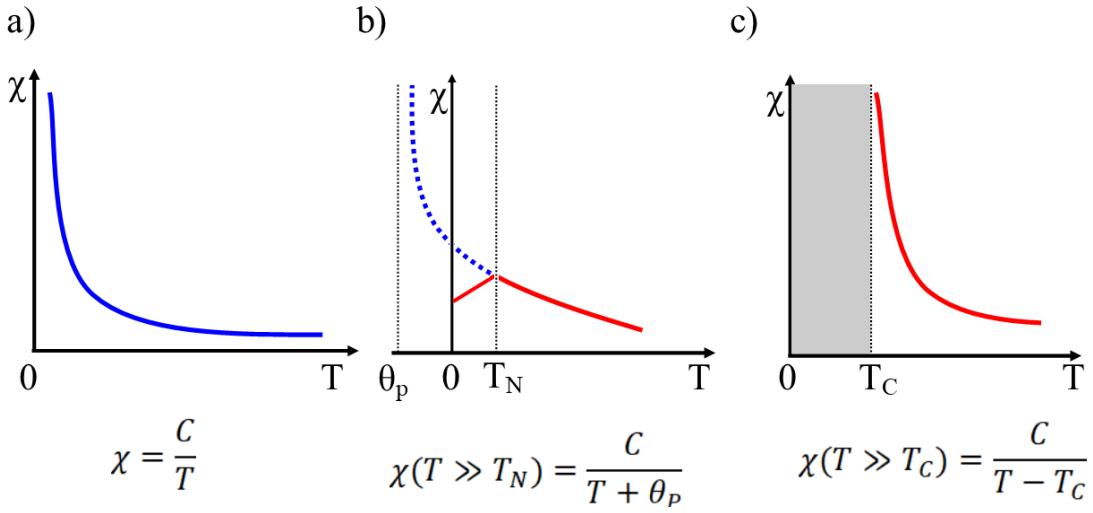

FIGURE 1.9: Temperature dependence of χ for paramagnetic material a. antiferromagnetic materials b. and ferromagnetic materials c.

Depending on the class of the material, the magnetic susceptibility changes with temperature differently. In the case of paramagnets, Fig. 1.9 (a), the susceptibility increases nonlinearly as the temperature goes down. For antiferromagnetic materials, Fig. 1.9 (b), the behavior is nonlinear above Néel temperature (T_N where the magnetic moments of atoms order anti-parallel) and it shows a nonlinear behavior at Néel temperature. For ferromagnetic materials, Fig. 1.9 (c), the magnetic susceptibility diverges at Curie temperature (T_C where the magnetic moments of the atoms order in parallel) and it shows a complex nonlinear behavior below T_C (shown by gray area in Fig. 1.9 (c)).

1.1.7 Modeling magnetic materials

We have developed the exchange interaction through a simple two-electron system and for two atom, now we will derive a model for more complex structures. We can use

the spin algebra to drive Heisenberg model. We consider Hamiltonian as $H = -2Js.s'$ between two spins s and s'. The total S where $S = s + s'$, will be 0 and 1 for antiferromagnetic and ferromagnetic ordering of spins, respectively. Since $S^2 = S(S+1)$ for any spin, both s and s' with $\frac{1}{2}$ moments, would give $s^2 = \frac{1}{2}(1+\frac{1}{2}) = \frac{3}{4}$ and $s'^2 = \frac{1}{2}(1+\frac{1}{2}) = \frac{3}{4}$ and for total S we will have $S^2 = 0$ and $S^2 = 2$ for antiferromagnetic and ferromagnetic orderings. From the relations $S^2 = 2s.s' + s^2 + s'^2$ for $S = 0$ (AFM case) and $S = 1$ (FM case) we can calculate $2s.s' = \frac{3}{2}$ and $2s.s' = \frac{7}{2}$, respectively. From these we can write the Hamiltonian for AFM ordering as

$$H_{AFM} = -\frac{3}{2}J$$

and for FM ordering as

$$H_{FM} = -\frac{7}{2}J$$

and the energy difference between AFM and FM ordeing will be:

$$\Delta H = H_{AFM} - H_{FM} = 2J \tag{1.43}$$

From this we can see that the energy difference between two states is $2J$. From this result, we can write Hamiltonian of the system of spins as:

$$H = 2\sum_{ij} J_{ij} s_i.s_j - g\mu_b\mu_0 \sum_i H_i^{ext}.s_i \tag{1.44}$$

Where H^{ext} is the external magnetic field on spin site i. This model describes a spin-lattice model.

In this model, the atomic moments are considered to be localized and interatomic repulsion to be very big i.e $U \to \infty$. In this approximation, if we consider electronic hopping integral (t) as a perturbation, then we can write the exchange as:

$$J_{ij} = J_{ij,D} - \frac{2t_{ij}^2}{U_{ij}} \tag{1.45}$$

The model in Eq. 1.44 is the simple Heisenberg model. Solving this equation is not feasible for most of the systems and to solve this, normally a mean filed approach or numerical approach is used.

To have a model that includes all the interactions discussed so far, which can capture properties of the real material with localized magnetic moments, we need to extend the Heisenberg model (Eq. 1.44) by including MCA and also DMI. The extended Heisenberg model can be developed as:

$$H_{His} = 2\sum_{ij} J_{ij} S_i.S_j - g\mu_b\mu_0 \sum_i H_i^{ext}.S_i + \sum_{ij} D_{ij}.(S_i \times S_j) + K\sum_i (n_i.S_i)^2 \tag{1.46}$$

In which we have included the MCA to second-order and of easy axis type.

To use this model, we need to calculate its different parameters (i.e J, D, and K). To do so, we need to solve many-body equations describing the electrons and nuclei in the materials. In the next section, we will present a method that is used widely by people interested in the properties of the material, in particular their magnetic properties, to solve the many-body equations.

1.2 Many body interacting particles

Many-body physics has been a big challenge for scientists for a long time. The difficulty in these systems arises from the interaction between particles which makes even solving simple classical Newtonian equations difficult for a three-body system. Description of the matter as a many-body problem for scientists besides its large numbers of interacting particles has some other difficulties that arise from the quantum nature of the system under study.

To understand and describe the physics of the many-body systems, we need to solve the Schrödinger equation (Eq. 1.47) for that system [16, 17]. Solving this equation for many-body problems encountered in physics is not feasible (apart from some simple two-body systems), which obliges scientists to resort to approximations in solving the problem and in describing the system under study.

The Schrödinger equation for many body system of interacting particles is written as:

$$i\frac{\partial\psi(\{r\},\{R\},t)}{\partial t} = \hat{H}\psi(\{r\},\{R\},t) \tag{1.47}$$

In this equation $\psi(\{r\},\{R\},t)$ presents many particles wavefunction as a function of time t and set of electron positions $\{r\}$ and nuclei positions $\{R\}$ where $\hat{H}$ is the Hamiltonian of the many particle system.

To solve the Schrödinger equation (Eq. 1.47), two approaches can be taken. The first one is through solving the Hamiltonian of the system with no empirical parameter. This

method is called ab-initio or first principles since we do not need to tune any parameter to describe the system. Solving Schrödinger equation using density functional theory (DFT) or Hartree-Fock method to have energies of the electrons and its properties is one such method.

While in the second method (empirical or semi-empirical), we adjust some parameters to study the behavior of the system. In this method, we give some parameters to the model to study it. The Heisenberg model is one such model in which we feed to the model exchange interactions and all the other degrees of freedom are neglected.

In this section, we will address the difficulties in solving Schrödinger equation. We will present a very popular method to overcome these challenges. We also present different approximations used in this method to make simulating these systems feasible.

1.2.1 Solving Schrödinger equation

In our studies, we are mainly interested in the ground state of the system. This brings in the first simplification to the Schrödinger equation by making it time independent [17]. We can describe the ground state of the system using Eq. 1.48. The ground state can be used to determine most of the properties of the materials, besides, it is also a good starting point to study excited states of the system as well.

$$\hat{H}\psi\left(\{r\},\{R\}\right) = E\psi\left(\{r\},\{R\}\right) \tag{1.48}$$

Eq. 1.48 shows the time independent Schrödinger equation. In this equation the Hamiltonian ($\hat{H}$) is a many body Hamiltonian and in general it is written as:

$$\begin{aligned}\hat{H} = &\sum_i \hat{T}_i + \sum_{ij} \hat{V}_e(r_i, r_j) + \sum_{i,n} \hat{V}_n(r_i, R_n) \\ &+ \sum_n \hat{T}_n + \sum_{nm} \hat{V}_{nm}(R_n, R_m)\end{aligned} \tag{1.49}$$

In this equation, $\hat{T}_i$ is the kinetic energy of the electrons and it is written as:

$$T_i = -\frac{1}{2}\nabla_i^2 \tag{1.50}$$

Where ∇_i^2 presenting $\frac{\partial^2}{\partial r_i^2}$, which is the second order derivative of the wavefunction with respect to position of particle i. $\hat{V}_e(r_i, r_j)$ is the Coulomb interaction between electrons at position r_i and r_j and can be developed as:

$$\hat{V}_e(r_i, r_j) = \frac{1}{|r_i - r_j|} \tag{1.51}$$

$\hat{V}_n(r_i - R_n)$ is the Coulomb interaction between ionic nuclei and electron at positions R_n and r_i respectively and it is:

$$\hat{V}_n(r_i - R_n) = \frac{Z_n}{|R_n - r_i|} \tag{1.52}$$

$\hat{T}_n$ is the kinetic energy of the nuclei and it is written as:

$$\hat{T}_n = -\frac{1}{2M_n}\nabla_n^2 \tag{1.53}$$

and $\hat{V}_{nm}(R_m - R_n)$ is the Coulomb interaction between ionic nuclei at position R_m and R_n as:

$$\hat{V}_{nm}(R_m - R_n) = \frac{Z_n Z_m}{|R_n - R_m|} \tag{1.54}$$

in which Z_n and Z_m presenting the nuclear charge of the atoms.

This equation, even though time-independent, is not yet soluble, so the next step is to use approximations to make it more simple. To this end, the equations for the electors and ions are separated. This simplification is coming from the fact that the mass of the ions is more than ≈ 2000 times the mass of the electrons which makes the motions of these particles much slower compared to electrons. This approximation is called Born-Oppenheimer or adiabatic approximation [18] and for most of the materials, this is a acceptable approximation. For this approximation, the wave function $\psi(\{r\}, \{R\})$ can be written as:

$$\psi(\{r\}, \{R\}) = \psi_e(\{r\})\psi_N(\{R\}) \tag{1.55}$$

and the Hamiltonian operator of electronic part is written as:

$$\hat{H}_E = \hat{H}_e + \hat{H}_{eI} \tag{1.56}$$

The electronic part can be solved by considering the ionic part to be constant. So we can write the Schrödinger equation for electrons as:

$$\begin{aligned}\hat{H}_E\psi_e(\{r\}) = \sum_i \hat{T}_i\psi_e(r_i) + \sum_{ij}\hat{V}_e(r_i,r_j)\psi_e(r_i,r_j) \\ + \sum_{i,n}\hat{V}_n(r_i - R_n)\psi_e(r_i)\end{aligned} \tag{1.57}$$

Where r presents spin and position degrees of freedom of N electrons in space and R_n are parameters.

The ionic part (i.e., H_I) can be solved using the Hellmann-Feynman theorem [see Eq. 1.58]. Using this theorem, forces on the atoms can be calculated in the field of electrons and using the classical equation of the motion, ions can be moved [19, 20].

$$F_I = - < \psi_e(\{r\})|\frac{\partial \hat{H}}{\partial R_I}|\psi_e(\{r\}) > \tag{1.58}$$

According to this theorem, a force on the ions can be calculated using Eq. 1.58. In this equation, we only need the expectation value of the derivative of the Hamiltonian with respect to the ionic positions with the wave functions calculated for the electrons in the ground state. Once the forces are calculated, we can move the ions according to the classical equation of the motion and find the minimum of the energy for the ionic structure.

Now all one needs to be able to describe the system, is the electronic wave functions. Among the first approaches to find the solution to electronic wave function is to use single particle wave function and build multiparticle wave function as [21]:

$$\psi_e(\{r\}) = \prod_i \phi_i(x_i,\sigma_i) \tag{1.59}$$

But later it was shown that these wave functions are not appropriate to describe the electrons [22], Since these do not show the Pauli exclusion principle. To solve the electronic part, we need to impose some restrictions on the form of the wave functions. These wave functions should be antisymmetric with respect to the exchange of the electrons [22]. This guarantees the Pauli exclusion principle. A common method to build such wave function is using Slater determinant as:

$$\psi_e(\{r\}) = \begin{pmatrix} \phi_1(x_1,\sigma_1) & \phi_2(x_1,\sigma_1) & ... & \phi_N(x_1,\sigma_1) \\ \phi_1(x_2,\sigma_2) & ... & ... & ... \\ ... & ... & ... & ... \\ \phi_1(x_N,\sigma_N) & \phi_2(x_N,\sigma_N) & ... & \phi_N(x_N,\sigma_N) \end{pmatrix} \tag{1.60}$$

Different methods have been developed to solve the electronic part of the Schrödinger equation including Hartree-Fock, DFT, and quantum Monte-Carlo. The DFT is the method that has good speed while it also gives acceptable accuracy. In the next section, we will present the DFT and present approximations used in this method. The idea behind DFT is to make it possible to perform computation on many-body systems.

1.2.2 Density functional theory (DFT)

DFT is the most common approach used today to study quantitatively the molecules, finite and periodic structures. This approach owes its success to the local density approximation (LDA) and the generalized gradient approximations (GGA) in Hohenbrg-Kohn and Kohn-Sham independent particle approach. The original idea of DFT is the method proposed by Thomas [23] and Fermi [24] in the 1920s. In their approach, kinetic energy is approximated as a functional of the density and in their theory, they used the local density approximation to describe exchange energies. But the method of Thomas-Fermi was missing many important features to describe correctly the physics and chemistry of the many-body systems besides not having solid mathematical proof. The modern DFT started in 1964 by Hohenbrg and Kohn (HK) [25], when HK showed that the density (n(r)) of the many-body particles can be considered as a basic variable from which all the properties of the materials can be calculated. This method is very efficient due to its ability to map a many-body Schrödinger equation to one equation for the density. In 1964 HK based the DFT on a mathematical foundation and show that DFT can be considered as an exact theory for any interacting many-body system.

The work of HK was proving two theorems. These theorems are as follows [25]:

Theorem one:

"For any system of interacting particles in an external potential $V_{ext}(r)$ the potential is uniquely determined except for a constant, by ground state particle density $n(r)$."

This means that there is one to one correspondence between density $n(r)$ and external potential $V_{ext}(r)$ and hence Hamiltonian of the system, which shows that the density can be used to describe all the properties of the system as the wave function of the system does.

Theorem two:

"A universal functional for the energy $E[n(r)]$ in terms of density $n(r)$ can be defined, valid for any external potential $V_{ext}(r)$. For any potential V_{ext}, the exact ground state energy of the system is the global minimum value for this functional, and the density $n(r)$ that minimizes the functional is the exact ground state density $n(r)$."

This theorem is equivalent to the Virial theorem in quantum mechanics and gives the ability to find the ground state of the system variationally.

These two theorems by HK, although put the DFT on a solid mathematical basis, they do not give a method to how to find the universal functional and the density. To resolve the problem, Kohn-Sham (KS) in 1965 proposed a method in which they replaced the many-body interacting problem with an auxiliary independent particle problem [26]. This independent particle problem can be solved exactly with all the difficult many-body terms described by an exchange-correlation functional of the density. The method proposed by KS has led to the useful approximation that are the basis of the modern first-principles or ab-initio methods. This theorem assumes that the ground state (GS) density can be represented by the ground state density of an auxiliary system of non-interacting particles. In this ansatz the calculations are done on an auxiliary system which can be presented by following Hamiltonian:

$$\hat{H}^{\sigma}_{aux} = \frac{1}{2}\nabla^2 + V^{\sigma}(r) \tag{1.61}$$

where $V^{\sigma}(r)$ is to be determined. The density for this system is :

$$n(r) = \sum_{\sigma} n(r,\sigma) = \sum_{\sigma}\sum_{i} |\psi^{\sigma}_{i}(r)|^2 \tag{1.62}$$

with kinetic energy as :

$$T_s = -\frac{1}{2}\sum_{\sigma}\sum_{i} < \psi^{\sigma}_{i}|\nabla^2|\psi^{\sigma}_{i} >= \frac{1}{2}\sum_{\sigma}\sum_{i} |\nabla\psi^{\sigma}_{i}|^2 \tag{1.63}$$

and the classical Coulomb interaction defined as :

$$V_c[n] = \frac{1}{2}\int d^3r d^3r' \frac{n(r)n(r')}{|r-r'|} \tag{1.64}$$

then the full KS approach is written as:

$$E_{KS} = T_s[n] + \int dr V_{ext}(r)n(r) + E_c[n] + E_{II} + E_{xc} \tag{1.65}$$

Here $V_{ext}(r)$ is an external potential from nuclei and any other external fields. All the many body effects are grouped into E_{xc}. This energy is written as:

$$E_{xc}[n] =< \hat{T} > -T_s[n]+ < \hat{V}_{int} > -E_c[n] \tag{1.66}$$

In this equation, $< \hat{V}_{int} >$ and $< \hat{T} >$ are the true interactions and kinetic energy of the interacting system. This $E_{xc}[n(r)]$ is defined to be universal and once determined it can be used in all the systems.

The KS equation can be minimized by constraining the wavefunctions to be orthonormal which leads to a Schrödinger like an equation as:

$$(H^{\sigma}_{KS} - \varepsilon^{\sigma}_i)\psi^{\sigma}_i = 0 \tag{1.67}$$

where ε^{σ}_i are the eigenvalues of the system and H^{σ}_{ks} is:

$$H^{\sigma}_{KS} = \frac{1}{2}\nabla^2 + V^{\sigma}_{KS}(r) \tag{1.68}$$

with

$$\begin{aligned} V^{\sigma}_{KS}(r) &= V_{ext}(r) + \frac{\delta E_c[n(r)]}{\delta n(r,\sigma)} + \frac{\delta E_{xc}[n(r)]}{\delta n(r,\sigma)} \\ &= V_{ext}(r) + V_c(r) + V^{\sigma}_{xc} \end{aligned} \tag{1.69}$$

Where δ represents functional derivative.

1.2.3 Exchange and correlations

The exchange-correlation (XC) approximation is the main part that makes this approach different from exact many-particle systems. As shown in Eq. 1.66, this energy is the difference between the independent particle and interacting particle kinetic energy and also the energy difference between Coulomb interaction in independent and interacting particles. The first approximation used in exchange-correlation functional was using local density approximation (LDA). In this approximation, the exchange-correlation energy is assumed to be equal to the exchange-correlation functional of a homogeneous electron gas with the same density. This XC is calculated for electron gas with very high accuracy. For this XC functional, the exchange-correlation energy is.

$$
\begin{aligned}
E_{xc}^{LSDA}[n^{\uparrow}(r), n^{\downarrow}(r)] &= \int d^3r n(r) \epsilon_{xc}^{hom}(n^{\uparrow}(r), n^{\downarrow}(r)) \\
&= \int d^3r n(r) \left[\epsilon_{x}^{hom}(n^{\uparrow}(r), n^{\downarrow}(r)) + \epsilon_{c}^{hom}(n^{\uparrow}(r), n^{\downarrow}(r)) \right]
\end{aligned}
\tag{1.70}
$$

Where the arrows show the spin Chanel of the density. The exchange energy in this functional can be calculated theoretically and the correlation part has been calculated using quantum Monte-Carlo method [27]. There are different parametrization for this functional including, Ceperley-Alder [27], Perdew-Zunger [28], Perdew-Wang [29] and Vosko-Wilk- Nusair [30].

Since this XC is written for homogeneous electron gas, it is expected to work well for systems that are close to homogeneous electron gas but it fails to give a good result for systems where the homogeneity is not held. This method underestimates the electronic gaps and interatomic distances by ∼30% to 100% and ∼3%, respectively. The main problem is the self-interaction that is included in this XC functional. In the Hartree-Fock method, the self-interaction energy is subtracted from the equation by exact exchange energy while in approximate XC only part of this interaction is subtracted. Hence, this method gives larger self-interactions for localized electrons which fails this approach in systems with high localization.

To improve the LDA approximation to XC, the first approach was to include ∇n^{σ} in the XC functional. This XC functional called generalized gradient approximation (GGA) and this is written as:

$$
\begin{aligned}
E_{xc}^{GGA}[n^{\uparrow}(r), n^{\downarrow}(r)] &= \int d^3r n(r) \epsilon_{xc}(n^{\uparrow}(r), n^{\downarrow}(r), |\nabla n^{\uparrow}|, |\nabla n^{\downarrow}|, ...) \\
&\equiv \int d^3r n(r) \epsilon_{xc}^{hom} F_{xc}(n^{\uparrow}(r), n^{\downarrow}(r), |\nabla n^{\uparrow}|, |\nabla n^{\downarrow}|, ...)
\end{aligned}
\tag{1.71}
$$

Where F_{xc} is dimensionless and ϵ_{xc} is the exchange-correlation energy of the unpolarized gas.

GGA XC improves the results compared to LDA. But still overestimates the lattice constants to ∼3% and the Bandgap not well reproduced. For GGA also there are different parametrizations among which we can name, Perdew-Wang91 [29], Perdew-Burke-Ernzerhof [32].

To further improve the performance of the XC functional, higher-order derivatives of the density are also included in the XC functional as well as the corrections to correlations

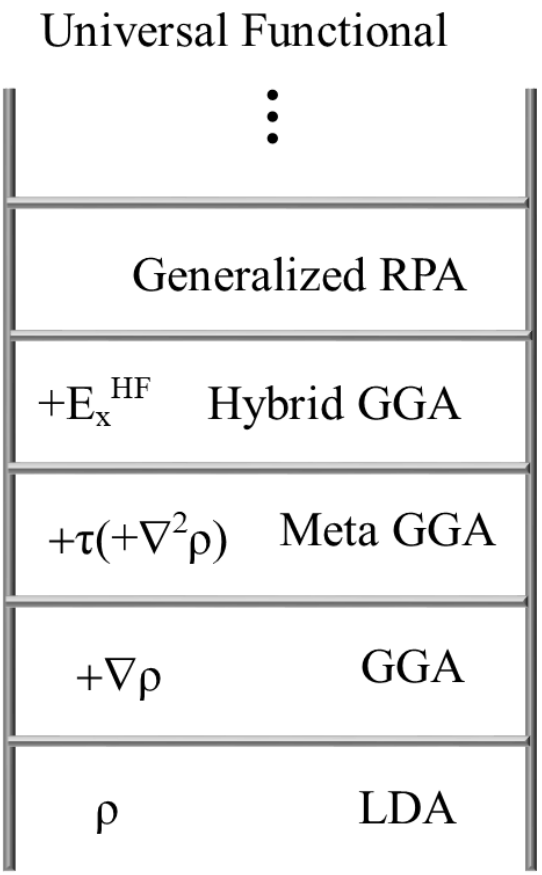

FIGURE 1.10: The figure (Jacob's ladder) presents different levels of improvements to the XC functionals [31]. Beyond meta GGA, the improvements are achieved by including hybrid functionals where some portion of the exchange interaction are computed exactly using Hartree-fock method. Further improvements are achieved using more complex methods such as random phase approximation(RPA)

coming from kinetic energy part [33]. This XC is called meta-GGA. The Proposed further improvements to XC functionals are shown in Fig. 1.10 by Perdew. Although there have been many works devoted to improving the XC functionals, these still fail to correctly describe the properties of the strongly correlated materials (materials with localized electronic orbitals).

1.2.4 Orbital dependent functionals: LDA +U

As mentioned in the previous part, the simplest XC functionals are not good for systems with large electronic localization due to self-interaction. These problems are more severe in systems with a transition metal or rare earth elements (highly correlated systems). One approach to alleviate this problem is the use of the so-called LDA+U method [34, 35]. This method is inspired by Hubbard model [36]. In this method, an additional interaction is considered only for highly localized orbitals. In the Hubbard model the Hamiltonian is written as:

$$\hat{H} = -\sum_{ij}\sum_{\sigma} t_{ij}\hat{c}^{\dagger}_{i\sigma}\hat{c}_{j\sigma} + U\sum_{i}\hat{n}_{i\uparrow}\hat{n}_{i\downarrow} \tag{1.72}$$

where t_{ij} is the electron transfer which decreases kinetic energy and tends to delocalize electrons while U is the repulsion between opposite spin electrons and favors localization of the electrons.

In LDA+U similar interaction to Hubbard interaction is added to the calculations to correct the tendency of the LDA for delocalization of the orbitals. This interaction makes the orbitals more localized. This method improves the results of the calculations for the cases where the results are wrong with respect to the experiment especially the band gaps and magnetic moments.

1.2.5 Relativistic interactions in DFT

So far we have neglected relativistic effects in the discussions. In this part, we will show how the relativistic effects are included in the model. The main contribution from considering relativity in DFT is coming from spin-orbit interactions (SOI). This interaction, from the classical point of view, can be seen as the interaction of the electron's spin magnetic moments with the magnetic field created by the electron's motion in the electric field of the nucleus. In this picture we can describe the magnetic field felt by electron moving with momentum p in a radial electric field $E = \frac{1}{e}\frac{\partial V(r)}{\partial r}$ as:

$$B = \frac{r \times p}{m_e e c^2}\frac{1}{r}\frac{\partial V(r)}{\partial r} \tag{1.73}$$

By considering the $r \times p$ as L (orbital magnetic moment of the electron), and magnetic moment of the electron as $\mu_s = 2\mu_b\frac{S}{\hbar}$ we can write:

$$\hat{H}^{SOI} = \mu_s.B = \frac{2\mu_B}{\hbar m_e e c^2}\frac{1}{r}\frac{\partial V(r)}{\partial r}L.S \tag{1.74}$$

Considering this in DFT, the energy of this term will be:

$$E_{SOI} \approx \left\langle \psi_i | \lambda_i(r_i)\hat{L}_i.\hat{S}_i | \psi_i \right\rangle \tag{1.75}$$

This interaction plays a very important role in anisotropy of a magnetic structure.

1.2.6 Density functional perturbation theory (DFPT)

Some of the properties of materials arise from perturbing the system. These perturbations can be described by calculating the energy change of the structure due to a perturbation. The energy of the system can be expanded in terms of the perturbations and the response come from different orders of the expansion (i.e., $\frac{\partial E}{\partial \tau_i}$, $\frac{\partial^2 E}{\partial \tau_i \partial \tau_j}$, $\frac{\partial^3 E}{\partial \tau_i \partial \tau_j \partial \tau_k}$ where τ is the perturbation). For example, the polarization is $P_i = \frac{\partial E}{\partial \varepsilon_i}$, and the electronic susceptibility is $\epsilon_{ij} = \frac{\partial P_i}{\partial \varepsilon_j} = \frac{\partial^2 E}{\partial \varepsilon_i \partial \varepsilon_j}$ where ε_i represent an electric field perturbation in direction i. Examples of other properties that can be calculated using perturbation, include polarisabilities, phonons, Raman intensities and infra-red absorption cross-sections, just name a few.

In the following we are presenting different properties that can be calculated from second order perturbation of the energy:

$$\begin{array}{c} \\ \tau \\ \eta \\ \varepsilon \\ B \end{array} \begin{array}{c} \begin{array}{cccc} \tau & \eta & \varepsilon & B \end{array} \\ \begin{pmatrix} \Phi & \gamma & Z^* & Z_m^* \\ \gamma & C & e & q \\ Z^* & e & \epsilon & \alpha \\ Z_m^* & q & \alpha & \mu_m \end{pmatrix} \end{array} \tag{1.76}$$

Physical properties related to second energy derivatives with respect to atomic displacement (τ) and homogeneous strain (η), electric (ε) and magnetic(B) fields give: force constant matrix (Φ), elastic tensor (C), dielectric permittivity (ϵ), magnetic permeability (μ_m), Born effective charge (Z^*), magnetic effective charge (Z_m^*) piezoelectric (e) and piezomagnetic (q) tensors, magneto-electric tensor (α) and atom-strain coupling constant (γ).

To calculate these properties, two different schemes are used: direct method and density functional perturbation theory (DFPT). In the direct method, the energy of the system is calculated by including perturbation in the DFT calculations, and using finite differences the response can be extracted. This method is widely used to calculate phonons in materials, where the $\Phi_{ij} = \frac{\partial^2 E}{\partial \tau_i \partial \tau_j}$ terms are calculated, with τ_i is an atomic displacement that is clamped in the structure. The first derivative is zero since the calculations are being done in the ground state where the forces (first derivative) are zero. From the inter-atomic fore constants (Φ_{ij}), the phonon modes and eigenvectors can be determined.

In the second scheme, i.e, DFPT, the Sternheimer equations are solved self consistently [37–39]. This method is superior to the direct method in the sense it allows the calculations of the perturbations in reciprocal space and, hence, calculations of the perturbations with different wave vectors. Such calculations in the direct method need large super-cells, which limits the use of the method. In calculating the responses from DFPT, we need to calculate the different derivatives of the wave functions. Another advantage of DFPT is the use of the *"2n+1"* theorem where to calculate (2n+1)th order of perturbation in energy, we need to calculate nth order derivative of the wavefunctions [40, 41].

We have used DFPT to calculate effective charges (i.e., Z^*), and interatomic force constants (i.e., Φ) in this work.

1.2.7 Practical implementation of DFT

Solving the KS equation in practice is presented in Fig. 1.11. The method, in practice is solving the Eq. 1.67 subject to consistency of density ($n(r)$) and effective potential (V^{σ}_{eff}). The procedure for solving this equation starts with an initial guess for density by choosing some random independent particle wavefunctions ($n^{\sigma} = \sum_i c_i|\psi^{\sigma}_i$). At the next step, the potential corresponding to this density is calculated by the selected XC functional. Solving the KS equation comes next. This step is the most time-consuming part of the calculations. At this step, a new set of wavefunctions are calculated based on the given density. At the next step, these new wavefunctions are used to calculate new density. The convergence test is done on the density where the difference between two densities is calculated and if this difference is lower than some tolerance the calculations are converged and at the next step, other properties are calculated. Otherwise, the new density is used to calculate the effective potential and solve the KS equation again until the convergence is reached.

Once the calculation at the self-consistent loop is converged, the calculation of the properties starts. At this step, the eigenvalues of the particles are calculated which gives the ability to calculate the total energy of the system [see Eq. 1.77].

$$\epsilon_i = \langle\psi^{\sigma}_i|H^{\sigma}_{KS}|\psi^{\sigma}_i\rangle \tag{1.77}$$

Having calculated the density of the ground state, it can be used to calculate the forces on the atoms using the Hellmann-Feynman theorem [19, 20] and to find the ground state structure of the system by minimizing the forces.

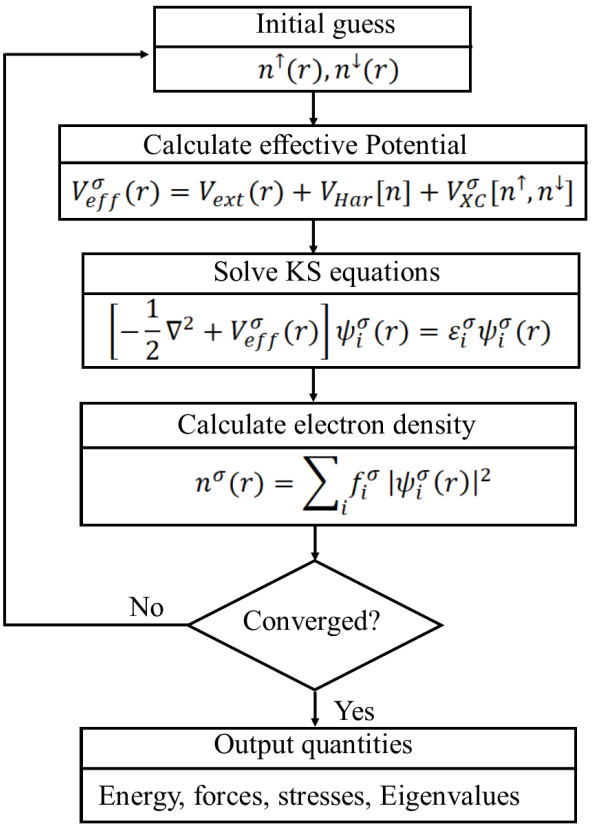

FIGURE 1.11: Schematic presentation of the self-consistent loop for calculating ground state density by solving KS equations.

The HK method only considers the ground state of the system, but there have been some other works that have extended the method beyond ground state including the work of Mermin [42] who extended the model to include finite temperature effects (although it has not been as popular as DFT) and also some works have included time-dependent external potentials and made it possible to study excited states and time evolution of the system as well [43].

1.3 Calculation of magnetic interactions

In this section, we are going to present the methods that have been used to calculate the magnetic parameters of our Heisenberg model. Since the magnetic interactions are small, the energy levels are very close and a robust method is needed to calculate the magnetic interactions introduced in section 1.1. We have used the method that was introduced by Xiang *et. al.* [44]. This method is called the 4 spin method (4SM) and it gives the exchange interactions pair-wise. Xiang has also extended the method to calculate other parameters than exchange such as DMI and single-ion anisotropy. Sabani *et.al* corrected the 4SM by considering anisotropic interaction compared to Xiang [45]. In this work, the

parameters are calculated using both the method of 4SM proposed in references [44–46] and, in some cases, a local force theorem method that we will describe after.

1.3.1 Total energy mapping

In this part, we will show 4SM that we have used to calculate the magnetic interaction including exchange, DMI, and single-ion anisotropy. The most general model to be considered for the magnetic interactions at second order of spins can be written as [6, 47]:

$$\begin{aligned} H &= H_{ex} + H_{SIA} \\ H &= \frac{1}{2}\sum_{i\neq j} S^i.J^{ij}.S^j + \sum_i S^i.A^{ii}.S^i \end{aligned} \tag{1.78}$$

Where i and j are lattice sites. J^{ij} and A^{ii} are 3×3 matrices in Cartesian coordinates. From these matrices, we can calculate the parameters presented in our Heisenberg models as in Eq. 1.46 according to reference [47]. The symmetric exchange or the exchange for our model is the diagonal elements of the $J^{ij}_{\alpha\alpha}$ matrices, and the parameters for DMI vector in γ direction are calculated as :

$$D^{ij}_{\gamma} = \frac{1}{2}\left(J^{ij}_{\alpha\beta} - J^{ij}_{\beta\alpha}\right) \tag{1.79}$$

And we can also calculate anisotropic symmetric exchange interaction as:

$$M^{ij}_{\gamma} = \frac{1}{2}\left(J^{ij}_{\alpha\beta} + J^{ij}_{\beta\alpha}\right) \tag{1.80}$$

with α, β and γ represent the Cartesian coordinates and i and j counts the lattice sites. We can calculate different components of the interactions by cycling the α, β and γ parameters.

Now that we have a general definition for the Hamiltonian, and the relation between the parameters of the general Hamiltonian and the extended Heisenberg model introduce in section 1.1, we continue with the procedure to calculate the parameters.

The method introduced in [44–46] uses the calculation of 4 different spin structures to have the parameters introduced. In this method, to calculate the magnetic interaction between sites 1 and 2, the energy of the system for these sites is considered to be:

$$E_{spin} = S^1.J^{12}.S^2 + K^1.S^1 + K^2.S^2 + E_{other} \tag{1.81}$$

with $K^1 = \sum_{i\neq 1,2} S_i.J_{i1}$ presenting interaction of the site 1 spin with spin sites other than site 2 and K_2 is $K^2 = \sum_{i\neq 1,2} S_i.J_{i2}$. To calculate the $J^{12}_{\alpha\beta}$, 4 different spin ordering should be considered with all the other site spin constant as:

$$1)S^1_\alpha = S,\ S^2_\beta = S \qquad 2)S^1_\alpha = S,\ S^2_\beta = -S,$$

$$3)S^1_\alpha = -S,\ S^2_\beta = S \qquad 4)S^1_\alpha = -S,\ S^2_\beta = -S$$

these four spin structure can be used in energy expression 1.81, for which we can have:

$$\begin{aligned} E_1 &= E_0 + J^{12}_{\alpha\beta}S^2 + K_1S + K_2S \\ E_2 &= E_0 - J^{12}_{\alpha\beta}S^2 + K_1S - K_2S \\ E_3 &= E_0 - J^{12}_{\alpha\beta}S^2 - K_1S + K_2S \\ E_4 &= E_0 + J^{12}_{\alpha\beta}S^2 - K_1S - K_2S \end{aligned} \tag{1.82}$$

and using the following expression we can calculate the $J^{12}_{\alpha\beta}$:

$$J^{12}_{\alpha\beta} = \frac{E_1 + E_4 - E_2 - E_3}{4S^2} \tag{1.83}$$

To calculate the SIA constants, we have used the 4SM too. In this method, the following spin structures are considered to calculate the anisotropies:

$$1)S^1_\alpha = S \qquad 2)S^1_\alpha = -S \qquad 3)S^1_\beta = S \qquad 4)S^1_\beta = -S$$

and then using the energy corresponding to each of these states we have calculated the $A^{11}_{\alpha\alpha}$ as:

$$A^{11}_{\alpha\alpha} = \frac{E_1 + E_2 - E_3 - E_4}{2S^2} \tag{1.84}$$

1.3.2 Calculation of the magnetic interactions using the local force theorem

To calculate isotropic exchange interactions, we have also used Green's function approach. In this approach, the local force theorem [48, 49] is used. According to the local force theorem, if we perturb the system locally, the force components can be determined from the change in single-particle energies and the change in the electrostatic field. When the spins are rotated by $\delta\phi$, change in total energy can be calculated according to local force theorem [48]. To do this, atomic localized orbitals are required. Since the calculations in this work are mainly done using a plane-wave basis set, we have used Wannier projection to get localized orbitals from the plane-wave basis set as suggested by Dm. M. Korotin *et. al.* [50] and as implemented in TB2J code [51].

According to ref [50], the localized wavefunctions for band n at site T of the system can be written using Wannier functions as:

$$\left|W_n^T\right\rangle = \frac{1}{\sqrt{N_k}} \sum_k |W_{nk}\rangle \, e^{-ikT} \tag{1.85}$$

Where the summation is over the Brillouin zone for band n and N_k is the number of k points and T is the lattice translation vector. In this equation W_{nk}:

$$|W_{nk}\rangle = \sum_{\mu=N_1}^{N_2} |\Psi_{\mu k}\rangle \, \langle \Psi_{\mu k}|\phi_{\mu k}\rangle \tag{1.86}$$

is the projection of plane wave to $\phi_{\mu k}$ atomic-like orbitals. Using these, the matrix elements of single-particle Hamiltonian in localized basis set can be developed as:

$$H^{WF}_{nm,\sigma}(k) = \langle W_{nk}| \left(\sum_{\mu=N_1}^{N_2} |\Psi_{\mu k}\rangle \, \varepsilon^{\sigma}_{\mu}(k) \, \langle \Psi_{\mu k}| \right) |W_{nk}\rangle \tag{1.87}$$

where σ represents the spin. Using this Hamiltonian, we can write the reciprocal Green's functions corresponding to k point in this system as:

$$G^{mm'}_{ij,\sigma}(\varepsilon, k) = \left[\, \varepsilon + E_F - H^{WF}_{mm',ij,\sigma}(k) \, \right]^{-1} \tag{1.88}$$

where E_F is the Fermi energy of the system under study and m, m' are orbitals on atoms on lattice sites i and j. By integrating the Brillouin zone (BZ), the two-particle Green's function will be:

$$G^{mm'}_{i'j',\sigma}(\varepsilon) = \int_{BZ} dk\ G^{mm'}_{ij,\sigma}(\varepsilon, k) e^{ik[(R_{i'} - R^0_i) - (R_{j'} - R^0_j)]} \tag{1.89}$$

From these, we can then calculate symmetric exchange interaction as:

$$J_{ij} = -\frac{1}{2\pi} \int_{-\infty}^{E_F} d\varepsilon \sum_{\substack{mm' \\ m''m'''}} Im \left(\Delta^{mm'}_i G^{m'm''}_{ij,\downarrow} \Delta^{m''m'''}_j G^{m'''m}_{ji,\uparrow} \right) \tag{1.90}$$

where:

$$\Delta^{mm'}_i = \int_{BZ} \left[H^{mm'}_{ii,\uparrow}(k) - H^{mm'}_{ii,\downarrow}(k) \right] dk. \tag{1.91}$$

Since in this approach the calculations of exchange interactions are done in the reciprocal space, it can calculate the interaction of an atom with all of its neighbors. Some of the calculated interactions are compared to 4SM calculations to ensure consistency of the method. This method also makes it possible to calculate exchange per orbitals.

To use the method presented in this section we have used it as implemented in TB2J code [51]. In this method, we first calculate the Wannier functions using Wannier90 code [52, 53]. Then by feeding the results of Wannier 90 code (tight-binding Hamiltonian's) to TB2J code, we can calculate symmetric exchange interaction. The TB2J code is extended to calculate the anisotropic magnetic interaction as well. But in this work, we have used the 4SM approach to calculate anisotropic magnetic interactions.

1.4 Conclusion

In section 1.1 of this chapter, we have discussed the origin of magnetic moments in atoms and the exchange interactions between these magnetic moments that create long-range magnetic ordering. We have presented direct exchange, superexchange, and also RKKY exchange interaction. We have also discussed magnetocrystalline anisotropy. We then described the DMI and its origin. By having all the relevant magnetic interactions, we have presented an extended Heisenberg model that can describe quite well the magnetic properties of materials.

In section 1.2, we have given an introduction to DFT. We have discussed different approximations used in this method as well as their deficiencies.

In the last section, we have introduced two different methods that we will use in our work to calculate the parameters that we need for our extended Heisenberg model including DMI, SIA, and anisotropic symmetric exchange interactions.

In the following chapters, we are going to first give an introduction to the physical properties of the compounds that we are interested in (i.e., rare-earth perovskites RMO_3), including their magnetic properties. Beyond this chapter, we will present our results concerning the magnetic properties and the origin of some unique behaviors present in these materials. In Chapter 4, we will use the model developed in chapter 3 to study the magnetoelectric response of $R\mathrm{MO}_3$s. At last, we will present the results of the works which are done in collaboration with A. Caviglia group on "Ultrafast control of magnetic interactions via light-driven phonons of DyFeO_3".

Chapter 2

Physics of rare-earth orthoferrites

2.1 Introduction

Rare-earth orthorhombic transition-metal perovskites oxides (RMO_3s where R is a rare-earth element and M is a transition-metal element) are a big family of materials. Each member of this family has different entangled degrees of freedom that make this group of structures an interesting playground to manipulate different functional properties [54]. Transition-metal sites in these structures can pose charge ordering, orbitals ordering, as well as magnetic ordering [54]. On top of these, Rare-earth elements can also magnetically order and interact with transition-metal sites and create a complex phase diagram. $R\mathrm{MnO_3}$s structures have attracted large attention due to their multiferroicity and considerable magnetoelectric (ME) responses [55–60]. $\mathrm{TbMnO_3}$, in particular, is among the materials that have been studied to a large extent due to its rich magnetic phase diagram which creates a large ME response. In these materials, the competing ferromagnetic and antiferromagnetic interactions between the first and second nearest neighbors of the transition-metal site create a frustrated spiral and cycloidal spin ordering [55, 56, 59]. The frustrated magnetic orders in these structures break the inversion symmetry and create ferroelectricity [56, 57, 60–62]. Such behavior is either present in most of $R\mathrm{MnO_3}$ structures or it can be induced by doping [58, 63–68]. $R\mathrm{NiO_3}$ have been under investigation due to their metal-insulator transition. In this family of materials, there are orbital ordering, charge ordering, and spin ordering which makes them have different functional properties including metal-insulator phase transition and multiferroicity [69–71]. $R\mathrm{VO_3}$ is not an exception in this group and it poses a rich phase diagram [72, 73]. In this group, due to strong spin-orbit entanglement, Jahn-Teller distortion, and magnetic ordering, the magnetic phase diagram is very rich, and to describe their behavior, one should go beyond Heisenberg model [73–76]. $R\mathrm{TiO_3}$ show interesting magnetic behavior [77].

These structures, besides being Jahn-Teller active, have a very sensitive magnetic phase diagram as a function of the rare-earth atoms radios [77, 78]. In these structure, the $LuTiO_3$ is ferromagnetic while, $DyTiO_3$ shows a C-type antiferromagnetic order [77, 78].

The rare-earth orthoferrite perovskites (RFeO$_3$s, which is the focus of this study), another family member of these structures, were discovered in the 1940s. These structures quickly attracted tremendous interest due to their unique magnetic properties [79–83]. RFeO$_3$s present non-collinear canted spins of the transition-metal (TM) atom, which often induces weak-ferromagnetism; they can exhibit two genuine magnetic phase transitions due to the presence of two different magnetic cations (TM and rare-earth); they can display temperature-driven spin reorientation (SR) and magnetization reversal (MR) [81]. Addressing the origin of these properties has been of scientific interest, besides being important for practical applications.

Along with their interesting magnetic properties, another appealing property of the RFeO$_3$ crystals, which has been the focus of numerous recent studies is their bulk multiferroism [80, 83]. Indeed, multiferroism in RFeO$_3$ compounds was first proposed based on simple symmetry arguments [47, 82]. For some specific combinations of the spin orders of the Fe and R sub-lattices, the space inversion symmetry is broken such that a ferroelectric polarization is induced. By construction, this magnetically-induced ferroelectricity has a high potential to yield large ME responses, as it can be expected to be very sensitive to magnetic-field-induced perturbations of the spin arrangement. This has been measured in $DyFeO_3$ and $GdFeO_3$, where the ME response appeared to be 2 orders of magnitude larger than the most common ME materials [80, 83].

In this chapter, we are going to present the properties of RFeO$_3$. In the first section, we will discuss the structure of these materials. Then we will present their magnetic properties and different magnetic phases and phase transitions present in these materials. Finally, we discuss some of the magnetoelectric and multiferroic properties of this family.

2.2 Atomic structure of orthoferrites

The RFeO$_3$'s belong to perovskite family. Perovskites have ABX_3 general formula and the high temperature structure is cubic [see Fig. 2.1(a)]. The name perovskite has its origin in the mineral perovskite, $CaTiO_3$. This family of structures, at high temperatures, adapts a cubic unit cell with five atoms and has $Pm\bar{3}m$ space group (No 221). For most of the perovskites, the cubic structure is not the ground state structure. In these structures, there is a phase transition that lowers the symmetry of the structures. The

type of phase transition is usually determined using the Goldschmidt tolerance factor which is defined as:

$$t = \frac{r_A + r_X}{\sqrt{2}\,(r_B + r_X)} \tag{2.1}$$

Where r_A is the ionic radius of the A site atom (rare-earth in our case), r_X is the ionic radius of the cation, which is Oxygen in rare-earth perovskites, and r_B is the ionic radius of the B site atoms (i.e., Fe here). In structures with t=1, the cubic structure is stable down to very low temperatures. When t >1, the structure goes through a phase transition of ferroelectric type [see Fig. 2.2(a)]. In this phase transition, the atomic displacements create a ferroelectric polarization in the structure by breaking inversion symmetry. When $r_A < r_B$ (i.e., $t < 1$), the ground state structure pose Oxygen octahedral tilts [see Fig. 2.1(b) and (c)]. These two distortions are not exclusive and for some structures, they both are present [84, 85]. The Oxygen octahedral rotations (OOR) are quite common in perovskites structures. To describe the OOR, the Glazer notation is used commonly [86]. In this notation, for OOR around the a axis, the notations $\overset{+}{a}\overset{0}{b}\overset{0}{b}$ or $\overset{-}{a}\overset{0}{b}\overset{0}{b}$ are used where 0, +, and − superscripts represent the no OOR, in-phase, and anti-phase OOR respectively, [see Fig. 2.1(a), (b), and (c)].

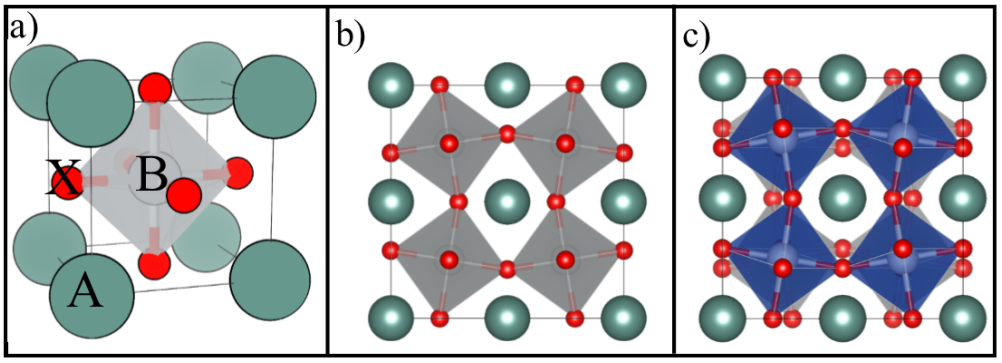

FIGURE 2.1: Schematic representation of cubic structure (a) where A, B and X site atoms are shown by corresponding letters. Oxygen octahedral rotations in-phase (b) and anti-phase (c). In (b) the Oxygen octahedral rotations are in the same direction between the planes parallel to the page and in (c) the Oxygen octahedral rotations in two planes are rotating in opposite directions.

Besides the mentioned structural distortions, perovskites also show other types of distortions like Breathing mode and Jahn-Teller mode [87, 88]. These distortions are not observed in rare-earth orthoferrites, so we will not discuss them here.

In 1956 Geller studied $GdFeO_3$ and determined the structure of this material as *Pbnm* [79]. For rare-earth orthoferrites, the Goldschmidt tolerance factor is less than one (i.e., t <1) which causes the Oxygen octahedral to rotate and lower the symmetry of the structure. In the case of RFeO$_3$ structures, the OOR is presented by $\overset{-}{a}\overset{-}{a}\overset{+}{c}$ notation, which shows

that there are three OOR in the structure. Two anti-phase rotations in a and b direction, and one in-phase rotation in c direction.

The three OOR ($\overset{-00}{abb}$, $\overset{0-0}{aba}$, and $\overset{00+}{aac}$), are represented by R_5^-, R_5^-, and M_2^+ irreducible representations respectively. These distortions are primary order parameters that lower the symmetry of the structure. These symmetry lowering distortions allow for the other distortions that are consistent with OOR to be allowed in the structure. These later distortions, that are coupled to the primary order parameters are called second order parameters. Two such distortions are present in RFeO$_3$s and are displacements of the rare-earth atoms (A-site atoms), namely X_5^+ and R_5^+ [see Fig. 2.2(b) and (c)]. The X_5^+ is larger in amplitude due to couplings with both OOR distortions compared to R_5^+.

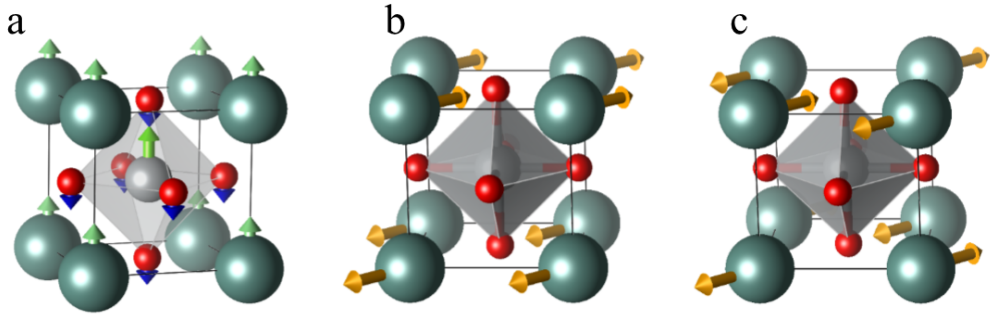

FIGURE 2.2: Caricature of distortions in prerovskites structure for polar distortions (a), X_5^+ antipolar motion of A site atoms (b), and R_5^+ antipolar motions of A site atoms (c).

The OOR are very important in determining the properties of these materials, and their amplitude depends on the size of R atoms in RFeO$_3$ structure [89]. The angle of OOR is defined according to [86]:

$$\Theta_{tilt} = \frac{180 - \widehat{BOB}}{2} \tag{2.2}$$

Where $\widehat{BOB}$ presents the angle between two neighboring B site atoms.

The OORs lower the symmetry of the structure for rare-earth orthoferrites and cause the unit cell to become 4 times the cubic unit cell, i.e., the cell becomes a 20-atom cell [see Fig. 2.3]. For this structure, the magnetic ordering of the Fe sublattice does not break any symmetry and it is consistent with the chemical unit cell ($Pbnm$ 20-atom cell). On the other hand, some of the magnetic ordering of rare-earth sublattice breaks inversion symmetry and reduces the number of symmetries but the cell still is a 20-atom cell with $Pna2_1$ space group [47].

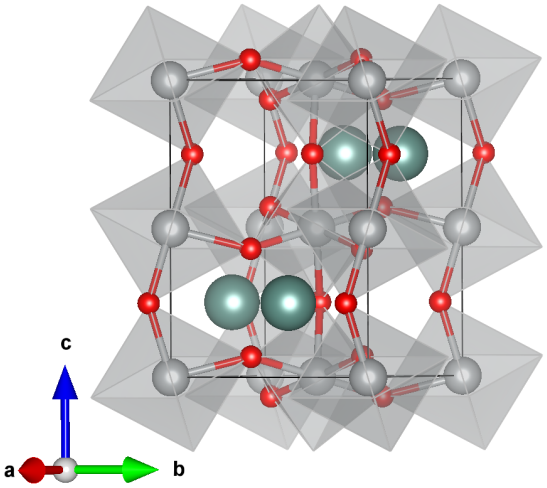

FIGURE 2.3: Schematic presentation of *Pbnm* structure with 20 atoms in the unit cell. Gray sphere representing Fe atoms, green spheres showing R atoms and Oxygen atoms shown with red spheres.

These materials have also been shown to be stable in different structures like $P2_1am$, $P4mm$, and hexagonal under epitaxial strain [90, 91]. These structures of the rare-earth ferrites families are shown to be ferroelectric and antiferromagnetic [90, 91].

2.3 Magnetic properties

The main motivation behind studying RFeO$_3$s has been their unique magnetic properties [79]. The rare-earth orthoferrites exhibit a great, and sometimes bewildering array of magnetic properties. A member of this family is typically a canted antiferromagnet, which displays two genuine first-order phase transitions as the iron and rare-earth magnetic moments order. These materials also have a compensation point where the two sublattices with different M(T) behavior cancel. These also show a spin reorientation transition during which the ordered spin systems rotate with respect to the crystal axes. The unique magnetic properties of the rare-earth perovskites are linked to the presence of both R and Fe magnetic cations [92].

2.3.1 Magnetic structures

The structure of RFeO$_3$s ($Pbnm$) has 20 atoms from which four Fe and four R atoms are magnetic. Néel in his studies separated the magnetic interactions of these atoms to Fe-Fe, Fe-R, and R-R interactions [93]. These interactions make the magnetic phase diagram of rare-earth perovskites quite rich and complex. To study magnetic behaviors of these compounds, Bertaut introduced symmetry-adapted irreducible representations

TABLE 2.1: Irreducible representation of magnetic states present in the *Pbnm* phase of RMO_3 for both transition-metal M-site and R site [47].

Irrep	M site	R site
Γ_1	$(A_x,\bar{G}_y,C_z)$	$(0,0,C_z)$
Γ_2	$(F_x,C_y,\bar{G}_z)$	$(F_x,C_y,0)$
Γ_3	(C_x,F_y,A_z)	$(C_x,F_y,0)$
Γ_4	$(\bar{G}_x,A_y,F_z)$	$(0,0,F_z)$

(IRREP) for the magnetic structure of these materials [47]. In his work, he has shown that the symmetry adapted spin ordering for *Pbnm* space group can be presented by four IRREPs, namely, Γ_1, Γ_2, Γ_3, and Γ_4 [see Tab. 2.1]. Each of these IRREPs is a linear combination of simpler magnetic orders (A, C, G, and F orders see Fig. 2.4) in different directions, that transforms according to the same IRREP of the *Pbnm* space group.

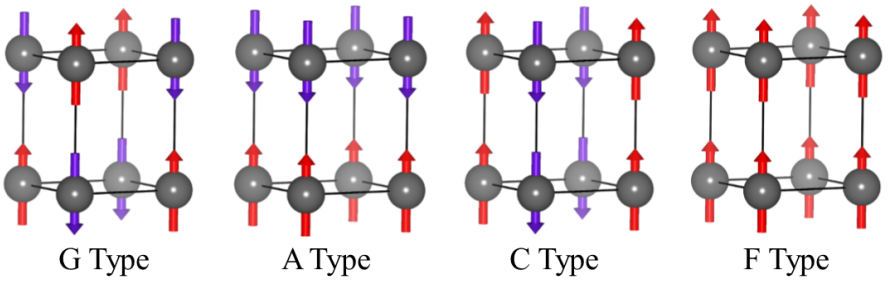

FIGURE 2.4: G-, A-, C-, and F-type magnetic ordering in *Pbnm* structures.

In these structures the dominant magnetic interactions are the exchange interaction between iron sublattices, that orders Fe atoms in G-type at temperatures of higher than 650 K. The G-type is the main spin direction (which is shown by a bar in Table. 2.1) and other letters in the notation show the cantings that are originating from Dzialoshinskii-Moriya interactions (DMI). Since the main magnetic interactions are iron antiferromagnetic, only Γ_1, Γ_2, and Γ_4 are observed in this family of materials, since the Γ_3 phase does not have a G-type ordering.

These structures are such that the Fe sublattice is not completely antiferromagnetic but is slightly canted to create a small ferromagnetic (wFM) order. Fig. 2.5 shows the schematic of the Γ_1, Γ_2, and Γ_4 IRREPs in these structures, where we can see a small ferromagnetic order for Γ_2 and Γ_4 in the x and z directions in Fig. 2.5(b) and (c). The wFM in these materials is particularly interesting. This property can be used in constructing magnetic memory devices, since, these would have a small depolarizing field. Before Dzialoshinskii's discovery on the origin of wFM in αFe_2O_3 [94], the origin of wFM in RFeO$_3$ structures was believed to be coming from different magnetic moments in Fe [93] sublattice. Latter Bozorth and Treves [95, 96], following Dzialoshinskii's discovery, showed that the origin of wFM in these structures is due to DMI. Recently

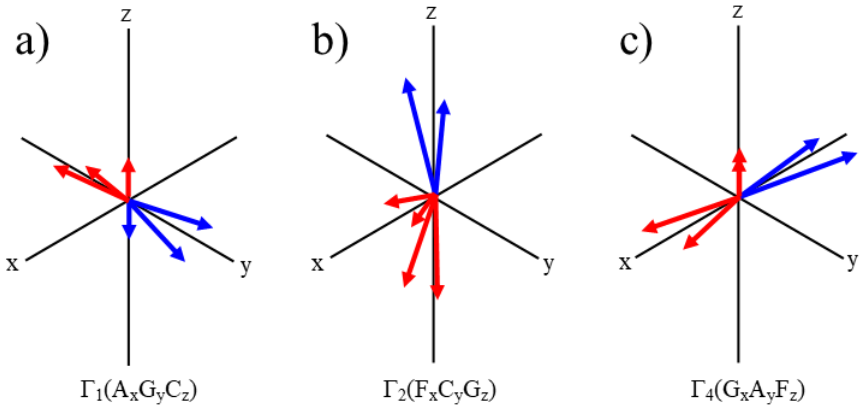

FIGURE 2.5: Schematic representation of Γ_1 (a), Γ_2 (b), and Γ_4 (c), spin configurations. Long arrows showing the main G-type spin direction for four sublattices and small arrows representing the canting of the spins where we can see small magnetization in panels (b) and (c). Figure taken from ref [92].

Bellaiche *et. al* [97] has written some energy expressions to describe these cantings. In this formulations, Energy from cantings due to the DMI can be written as:

$$\Delta E = K \sum_{ij} (\omega_i - \omega_j).(S_i \times S_j) \tag{2.3}$$

where ω_i presents the OOR around i magnetic site. For *Pbnm* structure the ω_i can be developed as:

$$\omega_i = (-1)^{n_x(i)+n_y(i)+n_z(i)}\omega_R + (-1)^{n_x(i)+n_y(i)}\omega_M \tag{2.4}$$

Where ω_R and ω_m are anti-phase and in-phase OOR amplitudes, respectively. From these, the following relations between different magnetic ordering are written [97] :

$$\begin{aligned} \Delta E = {} & 24NK\omega_R.(G \times F) + 16NK\omega_M.(C \times F) \\ & + 16NK\omega_M.(G \times A) + 8NK\omega_R.(C \times A) \end{aligned} \tag{2.5}$$

where this can be seen that the wFM (F) is arising from DMI interaction with G-type order. The interactions resulting in other cantings are also presented. This shows that the OOR plays a very important role in determining the magnetic properties of these structures. Specifically, Weingart *et. al* [98] has shown that the magnitude of canting and wFM in these structures has direct correlations with the magnitude of OOR [see Fig. 2.6].

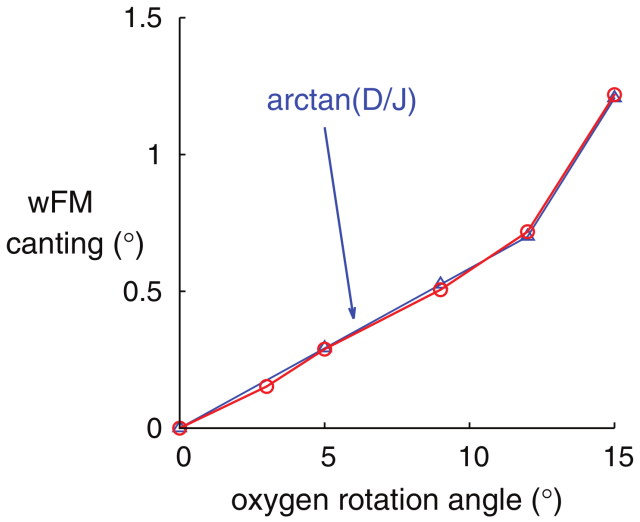

FIGURE 2.6: Change in magnitude of wFM as a function of OOR in $BiFeO_3$. The figure shows the calculated wFM (red circles) compared to arctan($\frac{D}{J}$) of the DMI (D) and exchange (J) interaction (blue line). Figure taken from ref [98]).

2.3.2 Magnetization reversal

Magnetization reversal (MR or compensation point) is another property of interest in RFeO$_3$s. In this behavior, the net magnetization of the material, which is originating from canting of the Fe sublattice at high temperatures, reverses its sign at lower temperatures [see Fig. 2.7 and Fig. 2.8]. This behavior is present in some of these materials, while it is not the case for some others [see Fig. 2.7 and Fig. 2.8]. First attempt to explain this behavior, came up with the idea that the rare-earth sites get polarized under the field of Fe atoms and it is polarized parallel to the Fe wFM for some of these materials, while in antiparallel direction to wFM for others; hence, causing MR. Although the explanation was given a long time ago for this behavior, the microscopic mechanism of the interactions between the two sublattices was not clear. In 2016 Zhao *et. al.* from the symmetry of the structure showed that the DMI between two sublattices can polarize the R site [99]. In Zhao's work, it was not clear why the sign of the interaction is positive for some of these materials, while it is negative for other ones. The microscopic mechanism for this behavior is still a question.

2.3.3 Spin reorientation

Most of the literature on RFeO$_3$s is devoted to studying and explaining the spin reorientation (SR) in these materials. This behavior is the rotation of the spins direction from one crystalline direction to another one. During the Γ_4 to Γ_2 SR, the spins direction changes from the a crystallographic direction to the c direction by slowly rotating as a function of temperature in ac plane [see Fig. 2.9]. The Γ_4 to Γ_2 SR can develop at

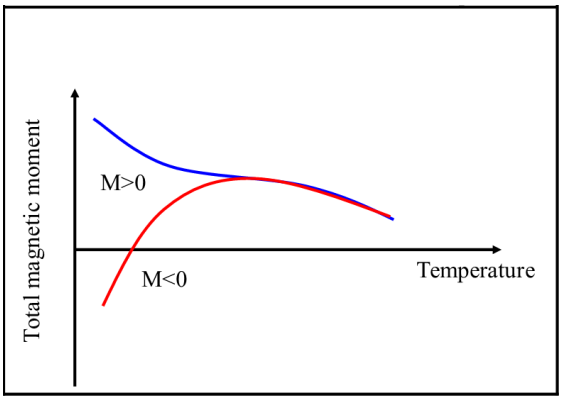

FIGURE 2.7: Schematic plot of the evolution of the total magnetization of the crystal and showing two possible cases: (i) MR effect (red line) where the magnetization changes sign below a critical temperature (compensation point) due to the fact that the paramagnetic rare-earth atom magnetizes in opposite direction to the wFM of the transition-metal atom. (ii) Absence of MR (blue line) where the magnetization is amplified when the temperature is reduced and corresponding to the case where the rare-earth atom magnetizes in the same direction as to the wFM of the transition-metal atom.

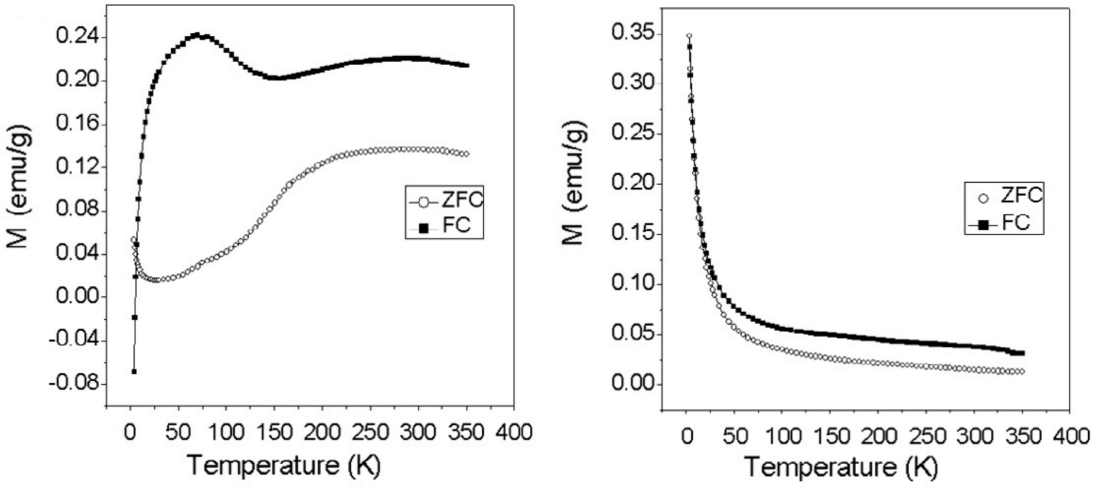

FIGURE 2.8: Change of weak magnetic order as a function of temperature for $NdFeO_3$ (left), where there is MR and for $GdFeO_3$ (right) where there is no MR in material [100].

different temperature window: for some materials it is rather fast (e.g., it spans through a 3 K temperature range [101] for $ErFeO_3$), while for others it can occur over a large temperature range (e.g., 70 K for $NdFeO_3$ [102]).

In the first explanation of the continuous rotation of spins as a function of temperature, a temperature-dependent anisotropy for Fe sublattice is defined phenomenologically in which the temperature width of SR is considered to be due to impurities in materials. In his studies, Gyorgy et. al using torque measurement showed the slow SR is intrinsic to these material [103]. So, the temperature-dependent model was not consistent with the slow rotation of the spins. Latter, a 4^{th} order anisotropy was added to the model

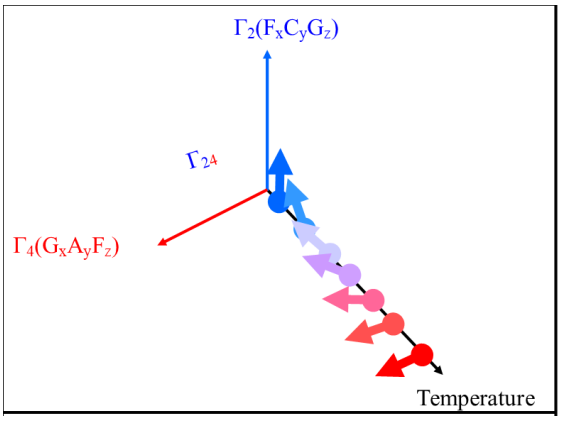

FIGURE 2.9: Schematic representation of the SR from Γ_4 (red color) to Γ_2 (blue color) as a function of temperature where the transition is smooth by passing through an intermediate mixed phase containing both states (Γ_{24}).

to account for the temperature width of SR in these materials [104]. In this model the potential energy surface for Fe sublattice is written as:

$$F = F_0 + K_1 sin^2\theta + K_2 sin^4\theta \tag{2.6}$$

Solving this equation to find the minimums of the free energy and stable states of the system will give:

$$\begin{aligned} \theta_1 &= \frac{\pi}{2} \\ \theta_2 &= 0 \\ sin^2\theta_3 &= \frac{-K_1}{2K_2} \end{aligned} \tag{2.7}$$

Where θ is the angle between c axis and magnetization. The solution θ_3, is real only between temperatures T_1 and T_2 given by $K_1(T_1) = -2K_2$ and $K_1(T_2) = 0$. In this model, there are two minimums of the spin structure free energy, and the slow rotation is captured in the model. Although, the model is still based on temperature-dependent anisotropy. Aring, following these studies, considered the effect of rare-earth ion on SR [105]. In this model, the temperature-dependent SIA of Fe sublattice was not considered and the SR is described to be due to interactions between R and Fe sublattices. Studies on $TbFeO_3$ show that there are two phase transitions, from Γ_4 to Γ_2 below 8.5 K and, then, at the ordering of Tb the Fe subsystem transforms back to Γ_4 [106]. This shows the importance of the R site ordering in this SR. It has also been shown that this SR is of second order [104, 107], and it could be associated with the softening of a low-frequency magnon mode [108, 109].

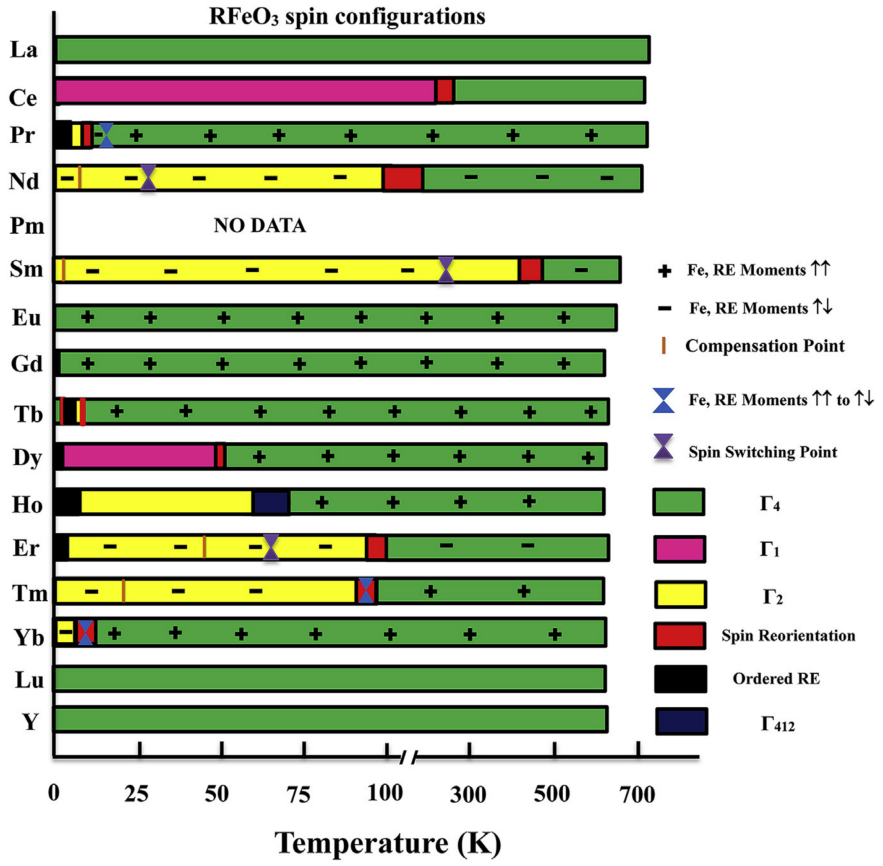

FIGURE 2.10: Summary of experimentally established spin configurations and magnetic phase transitions in the rare-earth orthoferrites. "+", "-" represent the parallel or antiparallel coupling moments of Fe^{3+} and R^{3+}, respectively. The orange line represents the position of temperature compensation. The blue triangles represent the moments of Fe^{3+} and R^{3+} undergo a parallel to antiparallel change. The spin switching point means the antiparallel coupling moments of Fe^{3+} and R^{3+} turn to the opposite direction simultaneously. The black part represents the ordering of rare-earth ions (Figure adapted from ref [110]).

Figure 2.10 shows the summary of the experimental results regarding magnetic properties of RFeO$_3$ from ref [110]. For most of the members of this family, the SR is from Γ_4 to Γ_2 as presented by green to yellow colors in the plot. Only two of the members show Γ_4 to Γ_1 SR (Ce and Dy). The figure also shows the MR point (shown by compensating point) which is below 50 K for all materials. As shown in Fig. 2.10 the rare-earth ordering temperature is quite low in these structures and their effect on the magnetic behaviors of these materials is negligible. Figure 2.10 shows the rare-earth ordering temperature for most of which the ordering temperature is below 6K.

Besides phenomenological models, some theoretical models have also been developed to describe the SR and magnetic interactions in RFeOs. Moskvin [111] has made a model to describe the magnetic interactions in RFeO$_3$ and RCrO$_3$. He has also made

use of the Anderson exchange model [7] to study superexchange and Dzyaloshinskii-Moriya interaction (DMI) in these materials [112]. A model developed and analyzed by Yamaguchi in the 70's [82] through a Heisenberg model featuring an effective exchange field of the Fe spins acting on the R spins. This model has been used as a reference work to explain the temperature-induced MR and SR and is often invoked to explain the multiferroic properties of RFeO$_3$ crystals. In his model, he has explained SR to be originating from the DMI between R and Fe sublattice, and the slow rotation is captured correctly. However, regarding theoretical or first-principles studies, only a little has been performed to understand the microscopic origin of the interactions between the two magnetic cations, as well as their role in the development of large magnetoelectric and multiferroic responses; hence, our current picture of these materials continues to be, to a large extent, speculative.

2.3.4 Magnetization hysteresis loops

Hysteresis in a ferromagnet refers to the history dependence of the magnetization upon sweeping an external magnetic field. RFeO$_3$s have also interesting magnetic Hysteresis loops. The behavior of these loops is shown to be dependent on the temperature where the MR happens [113]. These loops are rectangular close to MR point while they change their shape and show a s like shape at lower temperatures [see Fig. 2.11].

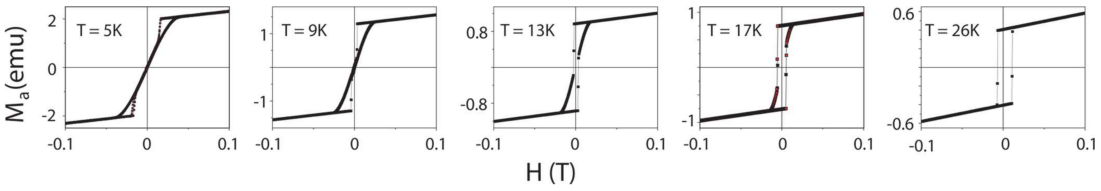

FIGURE 2.11: Magnetic Hysteresis Loops for ErFeO$_3$ from ref [113]. For temperatures close to MR (T=26) the Hysteresis loops are rectangular while for temperatures far from MR point the Hysteresis loops become s like.

Rare-earth orthoferrites also show an exchange bias effect. The exchange bias effect is a shift of magnetic hysteresis loop away from the center of symmetry, which has been used in a variety of magnetic storage and sensor devices [114] [see Fig. 2.12]. The basic mechanism of the exchange bias effect is that the magnetization direction in a ferromagnetic layer (free layer) can be pinned by an adjacent antiferromagnetic layer (pinning layer) [115].

The exchange bias effect has been observed in the single crystal ErFeO$_3$ [116]. This effect is particularly interesting since the behavior strongly depends on temperature. The ErFeO$_3$ has an MR temperature at 45 K. In ErFeO$_3$, it has been shown that the direction

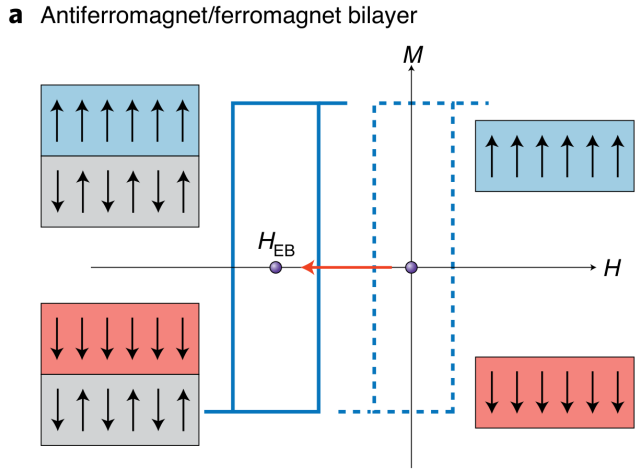

FIGURE 2.12: Schematic representation of exchange bias effect taken from ref [115]. The dashed hysteresis showing the behavior of the free ferromagnetic material. The solid blue line showing the hysteresis loop for ferromagnetic material on top of a antiferromagnet where we can see a shift (i.e., exchange bias effect).

of the exchange bias, changes sign at temperatures close to MR (T_{MR}) [116]. Fita *et.al.,* have shown that the direction of the exchange bias can change sign depending on its temperature history. The exchange bias sign may be changed to the opposite one by varying the field-cooling protocol, depending on whether T_{MR} is crossed with decreasing or increasing temperature [see Figure. 2.13] [116]. This behavior has also been observed in other RFeO$_3$ that have magnetization reversal like SmFeO$_3$ and NdFeO$_3$[117].

2.4 Magnetoelectric and multiferroic properties

Magnetoelectric (ME) materials are compounds in which there is a coupling between magnetic field (magnetization) and electric field (polarization) [118, 119]. Magnetoelectricity is an attractive material's response because it allows controlling of the magnetic properties using an external electric field or, the other way around, to control the polarization using an external magnetic field which can have a plethora of possible applications in spintronics, sensors, etc [114, 120, 121]. In particular, these materials can be used for memory devices and improve their performances by enhancing the speed of the device together with reducing its energy consumption [121, 122].

Since the first experimental observation of the ME effect by Astrov [123] there have been many attempts to find the ME effects in other materials but it appeared that most of these ME responses were very small to be considered practical [114, 121, 124, 125]. So far the discovered ME materials have either a small coupling [126], or a very low-performance temperature [56] which hinders putting them into applications. Different paths were introduced to enhance the ME response of materials. To name a few, we have

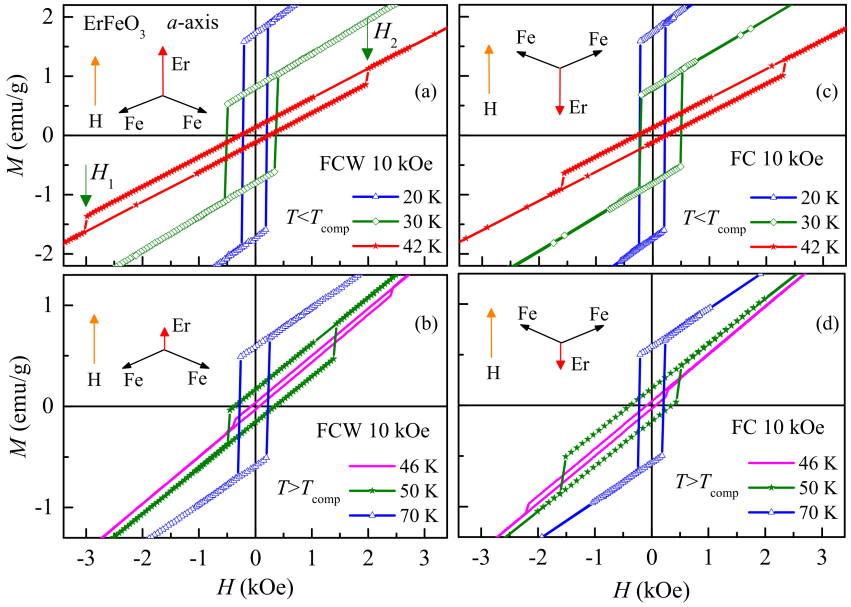

FIGURE 2.13: Magnetization hysteresis loops for $ErFeO_3$ for a magnetic field applied along a axis (direction of magnetization). (a) and (c) for $T < T_{MR}$ with $T_{MR} = 45K$ and (b) and (d) for $T > T_{MR}$ for different cooling procedures: FC in 10 kOe from 300 to 10 K and then warming to the given T (abbreviated in the figure as FCW), and FC in 10 kOe from 300 K to given T (abbreviated in the figure as FC). In the figure the possible magnetic ordering of the sublattice are also shown. Figure adapted from ref [116].

structural softness through epitaxial strain [127, 128], solid solutions [129], or making artificial structures and superlattices [90, 130].

Bulk multiferroic (MF) materials are a subclass of MEs in which there exist two ferroic orders in the same phase, i.e., ferroelectricity and ferromagnetism (or antiferromagnetism) [131]. This class of materials are divided into two groups, namely, type-I and type-II [132]. Type-II MFs are materials in which the magnetic ordering is the mechanism that breaks the inversion symmetry causing ferroelectricity. Hence, in type-II MFs a strong coupling between magnetism and polarization is present by construction, resulting in stronger ME responses compared to type-I MFs where the coupling is more indirect. The reported ME responses for these materials show that indeed the strongest ME responses are found in type-II MFs [56, 80, 83, 133, 134]. In a type-II MF, the ME response can result from either non-collinear spin ordering, in which we expect small polarization since it arises from spin-orbit coupling (SOC) ($10^{-2}\mu C/cm^2$); or it can result from inversion symmetry breaking due to collinear ordering of the spins. In the latter case, the mechanism can be other than SOC, like e.g. exchange striction, which typically yields large polarization (one to two orders of magnitude larger) compared to the first mechanism.

More than 50 years ago, Bertaut from a symmetry point of view showed that some of

TABLE 2.2: Rare-earth orderings that breaks the inversion center and the ME response matrix for these states from ref [47, 82]

Γ_5(G_x,A_y, 0)	Γ_6(0 , 0 ,A_z)	Γ_7(0 , 0 ,G_z)	Γ_8(A_x,G_y, 0)
$\begin{bmatrix} \alpha_{xx} & 0 & 0 \\ 0 & \alpha_{yy} & 0 \\ 0 & 0 & \alpha_{zz} \end{bmatrix}$	$\begin{bmatrix} 0 & 0 & 0 \\ 0 & 0 & \alpha_{yz} \\ 0 & \alpha_{zy} & 0 \end{bmatrix}$	$\begin{bmatrix} 0 & 0 & \alpha_{xz} \\ 0 & 0 & 0 \\ \alpha_{zx} & 0 & 0 \end{bmatrix}$	$\begin{bmatrix} 0 & \alpha_{yz} & 0 \\ \alpha_{zy} & 0 & 0 \\ 0 & 0 & 0 \end{bmatrix}$

the magnetic ordering on rare-earth sublattice in RFeO$_3$ structures would break the inversion symmetry [see Tab. 2.2] [47]. Yamaguchi also used symmetry and derived the magnetoelectric response matrices for these materials (the response matrices are shown in Tab.2.2) [82]. Indeed some of the rare-earth orthoferrites (e.g. GdFeO$_3$) are of type-II multiferroics, in which the collinear ordering of spins creates the polarization [80]. Hence, they have larger polarization compared to other type-II MFs as well as larger ME responses. Although the temperature at which the multiferroicity appears is very low (it requires that the rare-earth spins become ordered), their ME responses are among the highest reported in single-phase materials [80, 83] and, regarding the amplitude, they can compete with laminated composites (sandwiched structures of piezoelectric and magnetostrictive materials in which the strain coupling between the two materials is the mechanism creating large ME response) [135, 136]. These rare-earth orthoferrite materials have such a strong coupling that makes it possible to control ferroelectric order using magnetic fields or to control the magnetic ordering using electric fields [80]. However, the exact origin of their large responses has not been fully analyzed from first-principles or model Hamiltonian (fitted to first-principles) calculations due to the complexity associated with the presence of two different and coupled magnetic sublattices, and because the rare-earth magnetism comes from f electrons which are difficult to handle in density functional theory (DFT) calculations [137, 138].

In DyFeO$_3$, Dy atoms order in Γ_8 (see Tab. 2.2) at temperatures lower than 4 K. For this material Tokunaga *et. al* have shown that by applying a magnetic field of 25 kOe, the magnetic structure goes through an SR from Γ_8 to Γ_5 state [83]. Measuring the ME response in this material in these two states, they have found that this material shows a gigantic linear ME response when it rotates to the Γ_5 state. According to this report, DyFeO$_3$ becomes multiferroic, when it orders in the Γ_5 with a magnetization of 0.5 μB/f.u. and a polarization of 0.2 $\mu C/cm^{-2}$. The measured response is α_{zz} $\sim$2.4*10^{-2} esu [see Fig. 2.14]. The reported response for DyFeO$_3$ is large enough to be used in different applications but the low temperature of this response is a big hindrance. Following this work, using density functional theory Stroppa *et. al.* confirmed that the exchange striction mechanism is responsible for observed ME response [137].

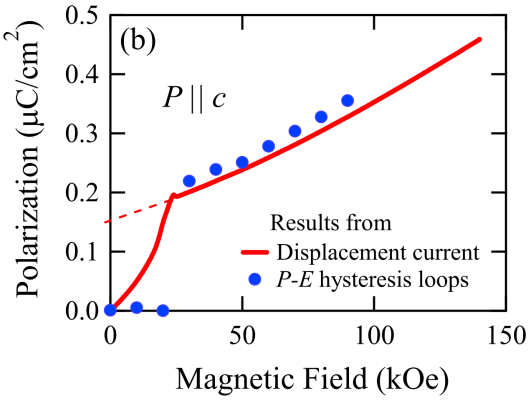

FIGURE 2.14: ME response for H||c dependence of the residual P obtained by P-E hysteresis loops (filled circles) and the displacement current measurement (solid line) [83].

Another family member of these structures that is worth mentioning is $GdFeO_3$. In this material, the Gd atoms order in Γ_5 at a temperature lower than 2.5 K. $GdFeO_3$ is both ferromagnetic and also ferroelectric at low temperatures [80]. For this material Tokunaga *et. al.* have reported a large nonlinear ME response, which originates from exchange striction between Gd and Fe atoms [see Fig 2.15]. Two different ME responses are observed in $GdFeO_3$, which are due to applied magnetic field in two different direction [see Fig. 2.16 and 2.15]. Due to this large ME response, it is shown that the magnetic ordering in this material can be controlled using an electric field [see Fig. 2.15] and ferroelectric ordering can be controlled by using a magnetic field. Zhao *et. al.* have used DFT and studied the general mechanism behind the ME responses in these materials [139]. In their studies, they have shown that relativistic effects are not important in the observed responses and the mechanism behind ME responses is exchange striction. They have also derived phenomenological and atomistic models that describe these couplings which can be used to predict and engineer these responses.

There have been some other works on the other family members of $RFeO_3$. In particular, we can name the work on $SmFeO_3$ by Lee *et. al*, who claim that $SmFeO_3$ is MF at room temperatures, a temperature that is higher than the ordering temperature of Sm ions [140]. The ferroelectricity is claimed to be due to the inverse DM effect. following this work Kou studied $SmFeO_3$s and found that there is no ferroelectricity in $SmFeO_3$ and explained previous ferroelectric observations to be due to spurious effect in the experiment. Their findings suggest that magnetoelastic effects may also lead to an artificial observation of pyrocurrents and, hence, the magnetoelastic coupling can easily be misinterpreted as a ferroelectric response [141]. But there is still conflict on this behavior and recently Dey et.al have reported a polarization in temperature close to room temperature in $HoFeO_3$ [142]. They claim that this ferroelectricity is coming from Oxygen atoms' displacements in the c direction and the space group is $Pb'n'2_1$.

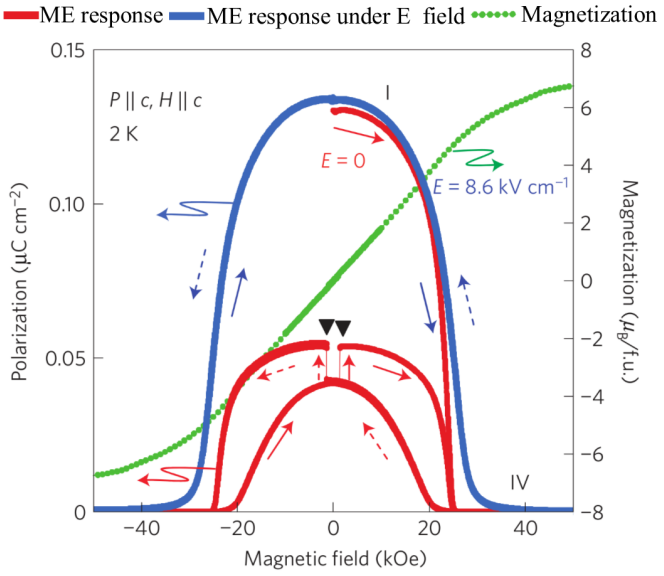

FIGURE 2.15: ME response of $GdFeO_3$. The change of polarization and weak magnetization of the material as a function of magnetic field. The magnetic field is applied in c direction (i.e., in the direction of weak ferromagnetic moment and perpendicular to G type order). The blue line shows the response under constant electric field of 8.6 $kVcm^{-1}$ while red line is the response with no electric field.(Figure taken from ref [80])

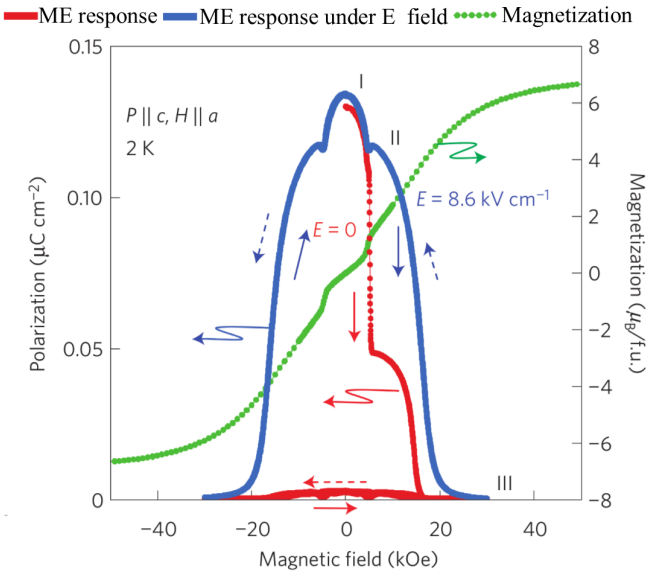

FIGURE 2.16: ME response of $GdFeO_3$. Change of polarization and weak magnetization of $GdFeO_3$ as a function of applied magnetic field. The magnetic field is applied in the x direction (i.e., in the direction of G type order). The blue line shows the response under constant electric field of 8.6 $kVcm^{-1}$ [80])

In ref [143], it has been shown that it is possible to induce ferroelectric and ferromagnetic orders in $DyFeO_3$ by applying uniaxial stress. In this work, it has been shown that the driven ferroelectric and ferromagnetic orders are coupled and they monotonically increase by increasing the uniaxial stress.

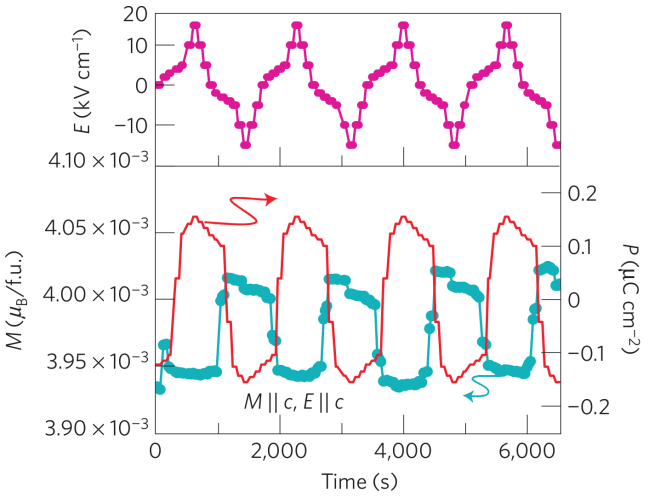

FIGURE 2.17: Top panel shows the applied time dependent electric field. Low panel, change of magnetization of the material as a function of the time dependent applied magnetic field (blue curve). Red curve showing the change in the polarization of the material as a function of applied magnetic. These results are for T=2 K [80].

This class of materials is also shown to be stable in different multiferroic structures. When the A site atom is small enough, the hexagonal structure can be stabilized too. $LaFeO_3$ has been grown in a hexagonal structure that is ferroelectric as well as antiferromagnetic [91]. In ref, [90] it is shown that applying large enough strain to these structures causes a phase transition to different noncentrosymmetric space groups. In this work, it is shown that by inducing high compressive strain, the structure transforms to a tetragonal state, even for large rare-earth ions, which have a giant polarization. By exerting a large tensile strain, it is shown to be possible to reach two different ferroelectric phases, one of which never observed in perovskites before, and both of which have large polarizations. Close to the phase transition points a multiphase boundary also occurs, which may lead to optimization of properties or unusual features. It is also concluded that the epitaxial strain allows tuning different properties of these predicted materials including polarization and magnetic ordering temperature [see Fig. 2.18].

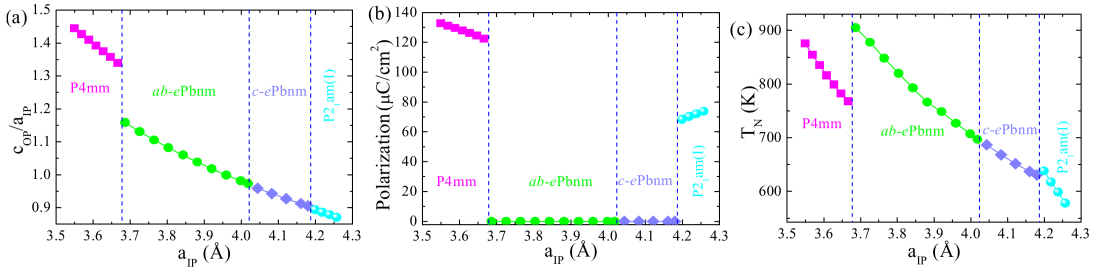

FIGURE 2.18: Figure shows different physical properties of the phases accessible to $CeFeO_3$ as a function of lattice parameter in (001) films. Panel (a), (b), and (c) showing the c/a ratio, polarization and Néel temperatures, respectively. [90].

2.5 Conclusion

To sum up, in this chapter we have given a brief overview of the properties of rare-earth orthoferrites. We have discussed their crystal structure and the lattice distortions present in them. We have also discussed their magnetic properties. In particular, we have discussed open questions regarding their magnetic properties (magnetization reversal and spin reorientation) and also some interesting magnetic properties observed in these structures, like hysteresis loops and exchange bias effect. Furthermore, we have discussed the magnetoelectric and multiferroic properties of $R\mathrm{FeO_3}$ and the most important reports regarding their ME responses. In the following chapter, we are going to answer the open questions regarding the magnetic properties of these materials and investigate their microscopic origin.

Chapter 3

Magnetic phase diagram of rare-earth orthorhombic perovskite oxides

3.1 Introduction

All the unique properties of $R\mathrm{FeO_3}$, rely on the presence of two magnetic sublattices, R and M with very different Néel temperatures such that for a wide range of temperatures the R spins are paramagnetic while the M spins are ordered. The associated magnetic interactions between these two sublattices have been proved to be the key ingredients for the origin of the SR, MR, and multiferroic properties [81, 144, 145], hence for their use in technological applications [97, 99, 146]. So, it is of paramount importance to understand the magnetic interactions and magnetic properties in these structures.

As discussed in chapter 2, there are still open questions regarding magnetic properties of $R\mathrm{FeO_3}$s (i.e., MR and SR). In this chapter, we shed some light on the magnetic properties of the $RM\mathrm{O_3}$s. We have used DFT [For the technical detail see Appendix B.1] to fit a microscopic Heisenberg model that includes the superexchange and the DMI interactions between the magnetic cations M-M and M-R (where M is Cr or Fe, and R is Gd). This model is then used as starting point, and we tune the different parameters to understand their specific role in the magnetic behaviors of the material using classical spin dynamics. The spin dynamics results are also compared with analytical solutions to confirm their consistency. Our work allows us to explain the origin of the SR and the parameters determining the SR temperature interval and how the R magnetism is affected while in its paramagnetic regime. We find that the occurrence of a slow SR comes from an original evolution of the Γ_4 and Γ_2 orders due to the presence of two different interacting

magnetic cations; this allows to have two magnetic phases to co-exist while no coupling exists between them in the Hamiltonian.

Before analyzing the fitted model, we start with an analytical model of the magnetic interactions present in RMO_3 systems.

3.2 Analytical model

To understand the mechanism behind SR and MR, we develop in this section the Heisenberg model and solve it analytically to understand the phase diagram of RMO_3 versus their microscopic magnetic interactions. This will also allow for comparison with the spin dynamics calculations to confirm that both give consistent results.

3.2.1 Symmetry-adapted spin representation

We develop an analytical model of RMO_3 using the symmetry-adapted spin representation. For each of the sub-lattices (M or R) in the $Pbnm$ unit cell, we have four magnetic sites that result in four different magnetic orders: A, C, G, and F type as presented in Fig. 3.1(b). Using these four magnetic orderings, we can define four symmetry adapted spin states, namely, Γ_1, Γ_2, Γ_3, Γ_4 that are a linear combination of the A, G, C, and F orderings in different directions (Fig. 3.1) [47]. Because the ground state of the M spin sub-lattice is a robust G-type antiferromagnetic ordering in the $Pbnm$ perovskite phase, the most relevant Γ_j states are those with $j = 1$, 2, and 4, which present a dominant G type in one of the three crystallographic directions with the presence of canted A, C, and F-type magnetic orders in the other directions. We summarize in Table 2.1 the different Γ_j states where $\bar{G}$ shows the main magnetic order and the components without a bar are small spin cantings.

Using these notations, we can write the symmetry-adapted magnetic states in terms of their modulation vectors for magnetic sub-lattice a as follows [Eq. (3.1) to Eq. (3.4)]:

$$S_{i,a}^{\Gamma_1} = A_{a,x}(-1)^{(n_z^i)} + \bar{G}_{a,y}(-1)^{(n_x^i+n_y^i+n_z^i)} + C_{a,z}(-1)^{(n_x^i+n_y^i)} \tag{3.1}$$

$$S_{i,a}^{\Gamma_2} = F_{a,x} + C_{a,y}(-1)^{(n_x^i+n_z^i)} + \bar{G}_{a,z}(-1)^{(n_x^i+n_y^i+n_z^i)} \tag{3.2}$$

$$S_{i,a}^{\Gamma_3} = C_{a,x}(-1)^{(n_y^i+n_z^i)} + F_{a,y} + A_{a,z}(-1)^{(n_z^i)} \tag{3.3}$$

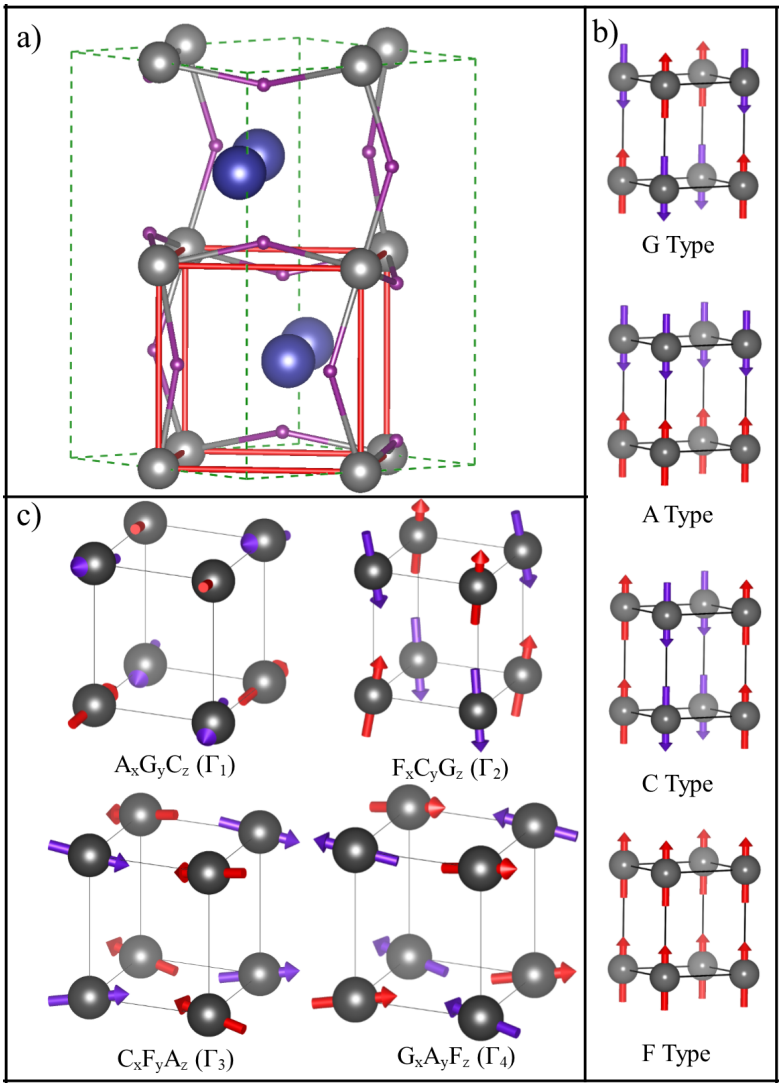

FIGURE 3.1: (a) Position of transition-metal ions (gray spheres) and rare-earth elements (blue spheres) in *Pbnm* structure, purple spheres represent oxygen atoms. (b) Schematic representation of the G, A, C and F magnetic orders for transition-metal sites present in *Pbnm* structure as highlighted by the red box in (a). Symmetry adapted representations Γ_1, Γ_2, Γ_3, and Γ_4 present in perovskites (c).

$$S_{i,a}^{\Gamma_4} = \bar{G}_{a,x}(-1)^{(n_x^i+n_y^i+n_z^i)} + A_{a,y}(-1)^{(n_z^i)} + F_{a,z} \tag{3.4}$$

Here $S_{i,a}^{\Gamma_j}$ is the spin of lattice site i for magnetic sub-lattice a (M or R) in irreducible representation Γ_j and the lattice site vector for lattice site i can be written as $n_x^i\hat{u}_1 + n_y^i\hat{u}_2 + n_z^i\hat{u}_3$ where $\hat{u}_1$, $\hat{u}_2$, and $\hat{u}_3$ are unit cell vectors while the coefficients G, A, F, and C represent the magnitude of spin canting in each direction, the G-type order being the main one. From now on, we will use these spin representations in our Heisenberg model.

3.2.2 Heisenberg model

In this section, we develop the Heisenberg Hamiltonian for RMO_3 in which we include the magnetic interactions between all the magnetic species: transition-metal atoms (M) and rare-earth atoms (R), which can be summarized as follows if one stays at the second-order of interactions (higher-order spin interactions like biquadratic or four-spin couplings are neglected):

$$H = H^{MM} + H^{RM} + H^{RR}, \tag{3.5}$$

where H^{MM} is the Hamiltonian of M-M interactions, H^{RR} the Hamiltonian of R-R interactions and H^{RM} the Hamiltonian of R-M interactions. H^{MM} can be written as follows:

$$H^{MM} = H_{ex}^{MM} + H_{\mathrm{DMI}}^{MM} + H_{\mathrm{SIA}}^{MM}, \tag{3.6}$$

where H_{ex}^{MM}, H_{DMI}^{MM} and H_{SIA}^{MM} represent the superexchange, DMI, and single-ion anisotropy (SIA) interactions of the M cations. In our simulations, we have neglected anisotropic symmetric exchange interactions since our DFT calculations show that they are two orders of magnitude smaller than DMIs (results not shown here).

For H^{RR} we have neglected the H_{ex}^{RR} and H_{DMI}^{RR} since we are interested in behaviors that take place at temperatures higher than the Néel temperature of the R spin sub-lattice. We will only keep the SIA interactions for this site.:

$$H^{RR} = H_{SIA}^{RR} \tag{3.7}$$

The Hamiltonian taking care of the R-M interactions can be written as follows:

$$H^{RM} = H_{ex}^{RM} + H_{DMI}^{RM} \tag{3.8}$$

The superexchange, DMI, and SIA terms can be developed as follows:

$$H_{ex}^{ab} = \frac{1}{2}\sum_{ij}^{N} \left(J_{ab,ij} S_{i,a}.S_{j,b}\right), \tag{3.9}$$

$$H_{\mathrm{DMI}}^{ab} = \frac{1}{2}\sum_{i,j} \left(D_{ab,ij} \times S_{j,a}\right).S_{i,b} \tag{3.10}$$

$$H_{\mathrm{SIA}}^{aa} = \sum_{i} K_a \left(S_{i,a}.\hat{e}_i\right)^2, \tag{3.11}$$

where ab could be $a = b = M$, $a = b = R$ or $a = M$ and $b = R$ and $\hat{e}_i$ is a unit vector pointing to the direction of the SIA axis, which, according to our DFT calculation for $GdFeO_3$ and $GdCrO_3$, is the easy axis.

We can show that there is no interaction between the different Γ_j magnetic orderings [see Appendix A] such that we can write the total energy of the system as the sum of the energy of each state. In this case we can write the total energy as:

$$H = H^{\Gamma_1} + H^{\Gamma_2} + H^{\Gamma_3} + H^{\Gamma_4} \tag{3.12}$$

In our analytical derivations, we have neglected the Γ_3 state since this state is much higher in energy than Γ_1, Γ_2 and Γ_4. This is related to the fact that the Γ_3 state does not contain G-type order, which is the order driving the lowest energy in the crystal through the strongest superexchange interactions between transition-metals.

By putting the spin states in the Hamiltonian we can derive the following expressions for each of the states [see Appendix A]:

$$\begin{aligned} H^{\Gamma_1} =& H^M_{ex} + H^M_{DMI} + H^{RM}_{ex} + H^{RM}_{DMI} \\ =& NJ^M(A_{M,x})^2 - 3NJ^M(\bar{G}_{M,y})^2 - NJ^M(C_{M,z})^2 \\ & - 6Nd^M_x \bar{G}_{M,y} C_{M,z} - 6Nd^M_y C_{M,z} A_{M,x} - 6Nd^M_z A_{M,x} \bar{G}_{M,y} \\ & - 8Nd^{RM}_x C_{R,z} \bar{G}_{M,y} - 8Nd^{RM}_y C_{R,z} A_{M,x} \end{aligned} \tag{3.13}$$

$$\begin{aligned} H^{\Gamma_2} =& H^M_{ex} + H^M_{DMI} + H^{RM}_{ex} + H^{RM}_{DMI} \\ =& 3NJ^M(F_{M,x})^2 - NJ^M(C_{M,y})^2 - 3NJ^M(\bar{G}_{M,z})^2 \\ & - 6Nd^M_x C_{M,y} \bar{G}_{M,z} - 6Nd^M_y \bar{G}_{M,z} F_{M,x} - 6Nd^M_z F_{M,x} C_{M,y} \\ & - 8NJ^{RM} F_{M,x} F_{R,x} - 8Nd^{RM}_x \bar{G}_{M,z} C_{R,y} - 8Nd^{RM}_y F_{R,x} \bar{G}_{M,z} \\ & - 8Nd^{RM}_z F_{R,x} C_{M,y} - 8Nd^{RM}_z C_{R,y} F_{M,x} \end{aligned} \tag{3.14}$$

$$\begin{aligned} H^{\Gamma_4} =& H^M_{ex} + H^M_{DMI} + H^{RM}_{ex} + H^{RM}_{DMI} + H^R_{SIA} + H^M_{SIA} \\ =& -3NJ^M(\bar{G}_{M,x})^2 + NJ^M(A_{M,y})^2 + 3NJ^M(F_{M,z})^2 \\ & - 6Nd^M_x A_{M,y} F_{M,z} - 6Nd^M_y \bar{G}_{M,x} F_{M,z} - 6Nd^M_z \bar{G}_{M,x} A_{M,y} \\ & - 8NJ^{RM} F_{M,z} F_{R,z} - 8Nd^{RM}_x F_{z,R} A_{M,y} - 8Nd^{RM}_y F_{R,z} \bar{G}_{M,x} \\ & - NK^M(\bar{G}_{M,x})^2 - NK^R(\bar{G}_{R,x})^2 \end{aligned} \tag{3.15}$$

TABLE 3.1: Calculated magnetic interactions from DFT of $GdFeO_3$ and $GdCrO_3$. J (average values between nearest neighbors) values are for the nearest neighbors and d_i are the DMI vector components along $i = x$, y and z. The units are in meV and to have the exchange and DMI parameters these values should be divided by the spin moment multiplication shown in last column. This from is convenient for comparing different systems with different spin amplitudes.

	d_x	d_y	d_z	J	$S_1.S_2$
Fe-Fe	0.00	-1.80	-1.10	38	25/4
Cr-Cr	-0.00	-0.81	-0.60	7.2	9/4
Gd-Fe	0.00	-0.06	0.03	1.85	35/4
Gd-Cr	-0.01	0.04	-0.02	2.15	21/4
Gd-Gd	–	–	–	0.19	49/4

Where J^M and J^{RM} are, respectively, the superexchange interaction magnitude for M sublattice and between R and M spins(J^a is considered as J_{ii} for isotropic exchange interaction); d_i^a is the magnitude of ith component of DMI vector for magnetic sub-lattice a; and N is the number of magnetic atoms while K^a represent the SIA magnitude of magnetic sublattice a.

With Eqs. (3.13)–(3.15) we have decomposed the Hamiltonian in terms of three independent representations Γ_1, Γ_2, and Γ_4, themselves decomposed into the superexchange, DMI and SIA of their constituent A, C, G, and F magnetic orderings. This form allows us to decompose the different microscopic contributions of the magnetic energy of the RMO_3 systems.

3.3 Calculation of the magnetic interaction parameters

In this section, we will present the parameters that we have calculated using DFT for $GdFeO_3$ and $GdCrO_3$, which will serve as a reference starting point in our spin dynamics simulations. These values will guide us to scan the magnetic phase diagram in regions that are relevant to these materials.

3.3.1 Superexchange and DMI parameters

The dominant interactions are the superexchange interaction between transitions metals. The DFT results for $GdFeO_3$ and $GdCrO_3$ show that the strongest superexchange interactions are between the nearest neighbors transition-metals; going further in distance gives very small values with respect to the nearest-neighbors such that they can be neglected. These interactions are 38 and 7.2 meV for nearest neighbors [see Table 3.1], in $GdFeO_3$ and $GdCrO_3$ respectively and 1 meV or below for the next nearest neighbors.

The *R-M* superexchange interactions are one order of magnitude smaller (approximately 2 meV) than the ones between transition metals. The *R-R* superexchange interactions are two orders of magnitude smaller than the transition-metals ones (around 0.2 meV) such that we have neglected the *R-R* interactions in our spin dynamics simulations. Calculated SIA for both sublattices in $GdFeO_3$ shows that these parameters are small around 72 μeV for Gd with easy axis along c direction and 75 μeV for Fe with easy axis along the b in the *Pbnm* structure; in $GdCrO_3$ the SIA constant for Cr in along c direction and it is 25 μeV.

The most relevant parameters for our behaviors of interest are the DMIs. Table 3.1 shows the obtained results, where the relation $d_y > d_z \gg d_x$ is always valid. It is the $\bar{a}\bar{a}^{+}c$ octahedral rotation pattern that breaks the bond inversion center of symmetry and creates the DMI [98]. Hence, we will have the biggest distortion in the [110] cubic direction (amplitude of the rotations in the y direction of the *Pbnm* structure) and the smallest one will be in the $[\bar{1}10]$ cubic direction (x direction of the *Pbnm* structure), (as shown in Fig. 3.2 the oxygen octahedral rotation has the same sign in the [110] direction and add up while in $[\bar{1}10]$ direction they have an opposite sign and subtract from each other), while the distortion in the [001] cubic direction (c direction of *Pbnm*) will be almost half of the one in the [110] cubic direction. The ratio between these distortions is close to being the same for any *Pbnm* crystal and this structural ratio also drives the key magnetic interactions as we will show below.

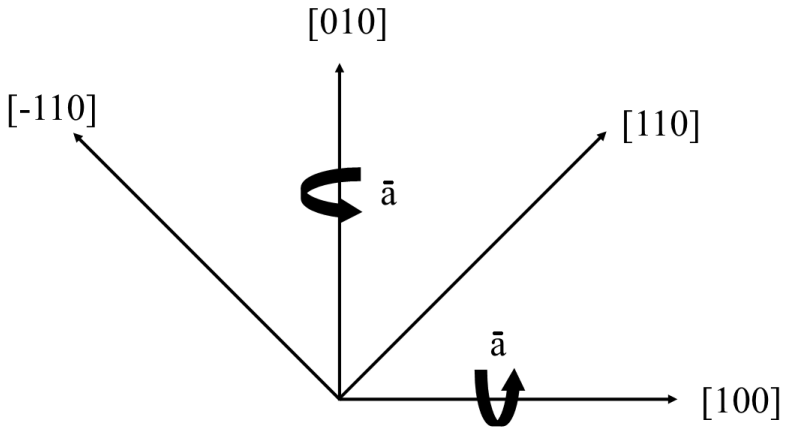

FIGURE 3.2: Schematic presentation of the cubic ([100] and [010]) and *Pbnm* ([110] and $[\bar{1}10]$) crystallographic directions with respect to each other. The curved arrows represent the oxygen octahedra rotations that are in the same direction when projected in the [110] direction while they are in opposite direction when projected in the $[\bar{1}10]$ direction.

At high temperatures, there is no magnetic ordering on R sites (paramagnetic phase) and the interactions between the R spins are negligible. Hence, at high temperatures, the SIA and DMI interactions of the M sites determine the magnetic equilibrium state. From the formulas 3.13,3.14 and 3.15 we can notice that both d_y^M and d_z^M, which have

the biggest components compared to d_x^M [see Table 3.1] in the Γ_4 state, are coupled with the main magnetic order and spin direction (i.e, $G_{M,x}$), making the energy of this state lower compared to Γ_1 and Γ_2. When comparing Γ_1 and Γ_2, we can observe that for the Γ_2 state we have the d_y^M terms that couple with the main spin direction, hence stronger than the d_z^M component present in Γ_1. This implies that the Γ_2 state is lower in energy than the Γ_1 state. Hence, we can have:

$$E_{\mathrm{DMI}}^{MM,\Gamma_4} < E_{\mathrm{DMI}}^{MM,\Gamma_2} < E_{\mathrm{DMI}}^{MM,\Gamma_1}$$

where $E_{\mathrm{DMI}}^{MM,\Gamma_j}$ is the energy from DMI between M atoms in the Γ_j state, i.e., the DMI between M cations favour the Γ_4 state [111].

We can also see the effect of these interactions in $R\mathrm{CrO_3}$ structures. According to Table 3.1, the DMIs and superexchanges in these structures are smaller than for $R\mathrm{FeO_3}$, which makes the energy difference between different spin orders (Γ_1, Γ_2, Γ_4) smaller. This is consistent with the fact that the Γ_2 and Γ_4 states are both presents at high temperature for the $R\mathrm{CrO_3}$ crystal series [147].

Considering the DMIs between R and M, we notice that in the Γ_2 state we have $H_{DMI}^{RM,\Gamma_2} = -8Nd_x^{RM}\bar{G}_{M,z}C_{R,y} - 8Nd_y^{RM}F_{R,x}\bar{G}_{M,z} - 8Nd_z^{RM}F_{R,x}C_{M,y} - 8Nd_z^{RM}C_{R,y}F_{M,x}$ terms in which d_y^{RM} couples with the main spin directions and also this state has more degrees of freedom compared to the other states making energy of this state lower. As for Γ_4 we have $H_{DMI}^{RM,\Gamma_4} = -8Nd_x^{RM}F_{z,R}A_{M,y} - 8Nd_y^{RM}F_{R,z}\bar{G}_{M,x}$ and for Γ_1 we have $H_{DMI}^{RM,\Gamma_1} = -8Nd_x^{RM}C_{R,z}\bar{G}_{M,y} - 8Nd_y^{RM}C_{R,z}A_{M,x}$ which again due to having the coupling $8Nd_y^{RM}F_{R,z}\bar{G}_{M,x}$ compared to $8Nd_x^{RM}C_{R,z}\bar{G}_{M,y}$ terms the Γ_4 state is lower than that of Γ_1 ($d_y^{RM} \gg d_x^{RM}$). Hence we can write the order of the different energies due to DMI of R and M as:

$$E_{DMI}^{RM,\Gamma_2} < E_{DMI}^{RM,\Gamma_4} < E_{DMI}^{RM,\Gamma_1}.$$

From this analysis, we can see why an SR transition is possible when lowering the temperature.

Indeed, as the temperature is lowered the interactions between R and M cations become stronger due to the magnetization of the R site in the field created by the M spins, and the Γ_2 is more and more favored through the DMIs between R and M sites. Hence, we can explain the Γ_4 to Γ_2 SR due to the DMIs between R and M sites as discussed previously by Yamaguchi [81].

3.3.2 Origin of ordering on R site

The MR observed in RMO_3 is the change of sign in the net magnetization of the material. This property has been related to the polarization of the R site atoms as a result of interaction with transition-metal atoms. In this interaction, R site atoms could polarize in the direction of the weak magnetic moment of the transition-metal or opposite direction, which would result in the presence or the absence of the magnetization reversal respectively [see Fig. 2.7]. The remaining question is why the R paramagnetic atoms magnetize in opposite direction for some R elements (e.g. $NdFeO_3$, $SmFeO_3$, $DyFeO_3$, $ErFeO_3$, $TmFeO_3$, $YbFeO_3$) and why they magnetize in the same direction for others (e.g. $PrFeO_3$, $EuFeO_3$, $GdFeO_3$, $TbFeO_3$, $HoFeO_3$) [100] and what is the microscopic origin of this effect.

With our model, we can have access to the detailed microscopic interaction between R and M cations. Equations 3.13,3.14 and 3.15 show that there are two types of interactions acting on R sites: (i) the superexchange interaction between the weak ferromagnetic (wFM) order of the M and R sublattices ($J_{RM}F_MF_R$) and (ii) the DMI between the G-type orders on the M and R sublattices ($d_y^{RM}F_{R,(z,x)}\bar{G}_{M,(x,z)}$ and $d_x^{RM}C_{R,z}\bar{G}_{M,y}$). These interactions can induce either F- or C-type ordering on the R site. To check the validity of these possibilities, we have used DFT calculations as computer experiments where we have replaced the Gd site by Cr in $GdFeO_3$'s *Pbnm* (i.e., $CrFeO_3$) structure to allow the study of full non-collinear calculations and to have stronger interactions between R-site and Fe-site atoms compared to the Gd case. Our model is valid for two magnetic sublattices in perovskites whatever the magnetic cations, such that replacing Gd by Cr will show the same qualitative trend.

We have done different calculations in which we constrained the magnetic moments on the Fe site and relaxed the magnetic order of the R site within two different settings. In the first setting, we set the spin-orbit coupling (SOC) to zero to suppress the DMI such that the resulting magnetic order on the R site would be due to superexchange interactions only. In the second setting, we considered SOC, hence activating the second term ($d_y^{RM}F_{R,(z,x)}\bar{G}_{M,(x,z)}$) that couples the G type order of the M sublattice to F order on R site. In Fig. 3.3 we show the result of these two types of calculations where we can see that the magnetization line jumps to higher values when the SOC is present. This shows that the DMI can polarize the R site as the superexchange, which is in agreement with the results obtained by Zhao *et al.* [99] using DMI energetic expressions between R and M sites.

We should also mention that in our simulations for R = Cr since the superexchange interaction is AFM, it polarizes the R site in the opposite direction to the wFM direction

of the M, while the DMI polarizes the R site in the same direction as the wFM of the M site [see Fig. 3.3]. Our calculations for $GdFeO_3$ also show that these interactions compete with each other such that the final magnetization direction of the R site will be determined by the balance between them.

Considering $GdCrO_3$ we can see in Table 3.1 that the DMI interactions between the Gd and Cr spins have opposite signs compared to the DMI interaction between Gd and Fe spins. This shows that we can also have a sign change of the DMI depending on the electronic structure of the atoms in the structure. The calculated magnetic ground state of the $GdCrO_3$ shows that the wFM of Cr and magnetic polarization of the Gd are in opposite directions, while for $GdFeO_3$ the wFM of the iron atoms and the magnetic polarization direction of the Gd atoms are in the same direction. Hence, depending on the electronic structure of the atoms we can have the superexchange and DMI that compete or cooperate that will result in the presence or the absence of the MR. This shows that the DMI between the two sublattices is the interaction that is responsible for polarizing the R site. The calculated DMI interaction signs are in agreement with experimental results which shows that for GdFeO3 there is no MR [100] while it is present in GdCrO3 [148].

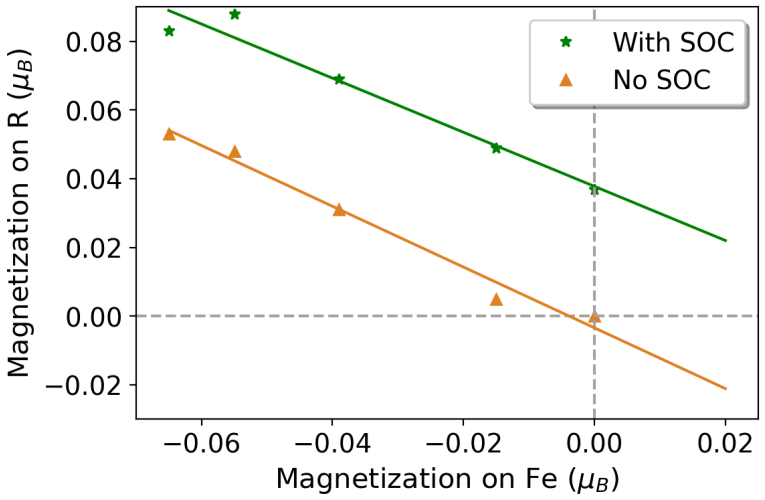

FIGURE 3.3: Calculated magnetization of R as a function of magnetization of Fe in $RFeO_3$ simulated at fixed atomic positions of relaxed *Pbnm* $GdFeO_3$ (R is Cr here i.e., $CrFeO_3$). Orange points are without spin-orbit coupling (with a linear fit orange line) and green points are with spin-orbit coupling (with linear fit green line).

3.4 Spin dynamics

In this section, we present the spin dynamics results obtained with the VAMPIRE code [see Appendix B.1 for details] through the Heisenberg model presented above (with

$R-R$ superexchange and DMI set to zero). First, we worked with the parameters of the magnetic interaction obtained for $GdFeO_3$. Then, we made additional spin dynamics calculations by varying the values of these parameters (related to larger spin-orbit interaction present in other rare-earth elements) to understand how the phase diagram and associated SR transitions are affected by the change of the magnetic interactions.

To verify that our model qualitatively respects the symmetry of the *Pbnm* phase of RMO_3 compounds, we first simulated the ground state (0 K) of these structures by tuning the SIA to obtain the magnetic moment direction along the different x, y, and z crystallographic directions. By doing so, we verified that the obtained cantings correspond to the ones of the Γ_4, Γ_1, and Γ_2 orders when magnetic moments lie along x, y, and z directions, respectively [see Table 2.1].

In the following, we will analyze both Γ_4 to Γ_2 and Γ_4 to Γ_1 SR transitions.

3.4.1 Γ_4 to Γ_2 reorientation

As a first step, we have done temperature-dependent SR. To have temperature-dependent SR, we have tuned the parameters obtained for $GdFeO_3$ to induce such behavior, since this effect is not present in $GdFeO_3$. More precisely, we increase the DMI interaction between R and M by one order of magnitude to have the SR. Figure. 3.4(a) shows the evolution of the magnetic moment directions with respect to the temperature when there is an SR, as obtained from our spin dynamics simulations.

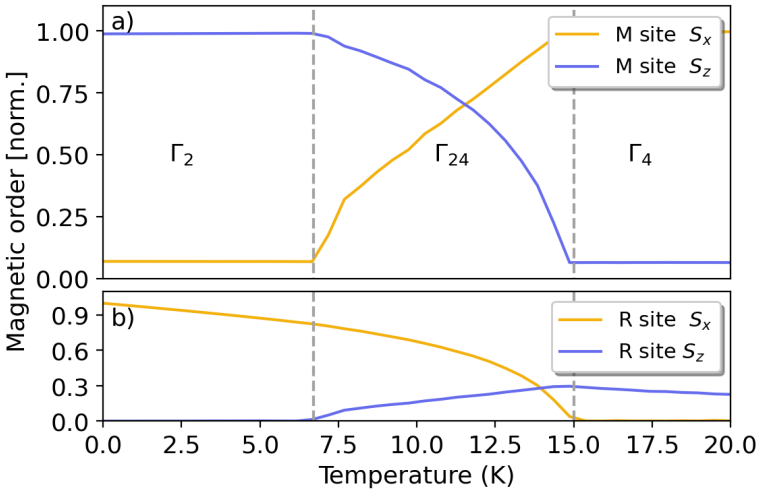

FIGURE 3.4: Temperature-dependent SR as obtained from our spin dynamics calculations. Panel (a) shows the transition-metal M site spin projections along the x and z directions. Panel (b) shows the evolution of the x and z magnetic moment projection of the rare-earth R site in the same temperature range as panel (a). The spin dynamics are done in 0.5 K intervals and we have interpolated the lines. The units on the y axis are spins normalized with their moments($\frac{5}{2}$ and $\frac{7}{2}$ for Fe and Gd, respectively).

We can see a slow rotation of the spins from x to z direction as the temperature decreases and that this reorientation is continuous in a range of temperature where the two orders (associated to the Γ_4 and Γ_2 states) are present together. Figure. 3.4(b) shows the temperature evolution of the magnetic ordering of the R spins due to its interaction with the Fe spins. Here, we can see that the SR happens around 15 K when the normalized magnetic moment of the rare-earth element is about 0.3. Below this critical temperature, the R site magnetization increases in a more pronounced way. Such an increase of the magnetization for the Er has been observed experimentally in $ErFeO_3$ at the vicinity of the SR region [145]. The increased magnetization of the R sites creates a torque that induces the rotation of the Fe magnetic direction. This result shows that we need the ferromagnetic ordering on the R site to have this Γ_4 to Γ_2 SR transition. This is also observed experimentally in, e.g., $TbFeO_3$ where the crystal goes from the Γ_2 state to the Γ_4 state when the Tb atom orders into the A_xG_y magnetic phase (no ferromagnetic order) at very low temperatures [106].

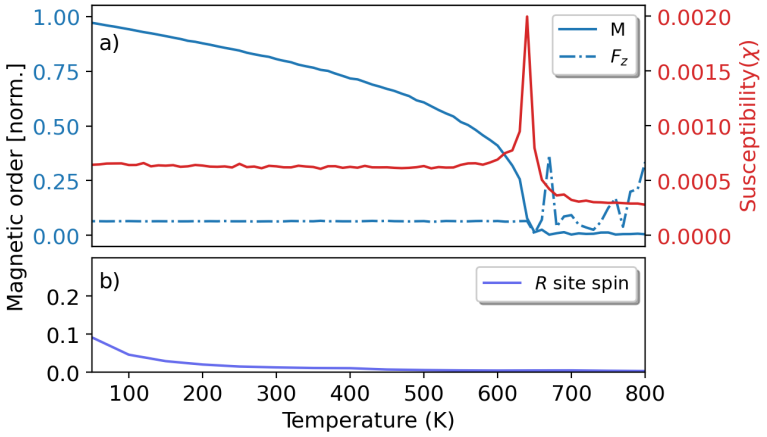

FIGURE 3.5: Temperature-dependent spin dynamics results for $GdFeO_3$: (a) normalized magnetic moment of the Fe site as projected along z and the mean magnetization of Fe sublattice(M). The second axis in panel (a) shows the susceptibility of the Fe sublattice shown in red and (b) normalized magnetic moment of the Gd site (ferromagnetic order along the z direction). The spin dynamics are done in 10 K intervals and the lines are interpolated.

In Figure. 3.5(a), we report the evolution of the magnetic orders at a higher temperature. From the susceptibility shown in red, we can see that the Néel temperature is around 650 K. We also obtain a Néel temperature of 654 K (using the $M-M$ superexchange parameters as obtained for $GdFeO_3$) which is calculated by fitting the curve with $(1-\frac{T}{T_N})^{\beta}$ with β=0.44. The wFM (F_z) appears at temperatures below the Néel temperature and, after a jump at the phase transition, stays constant ($0.10 \times \frac{5}{2}\mu_B$). In Fig. 3.5(b) we show the evolution of the R site magnetic moments where we can see that the induced magnetization of the rare-earth spins is visible at temperatures as high as 400 K.

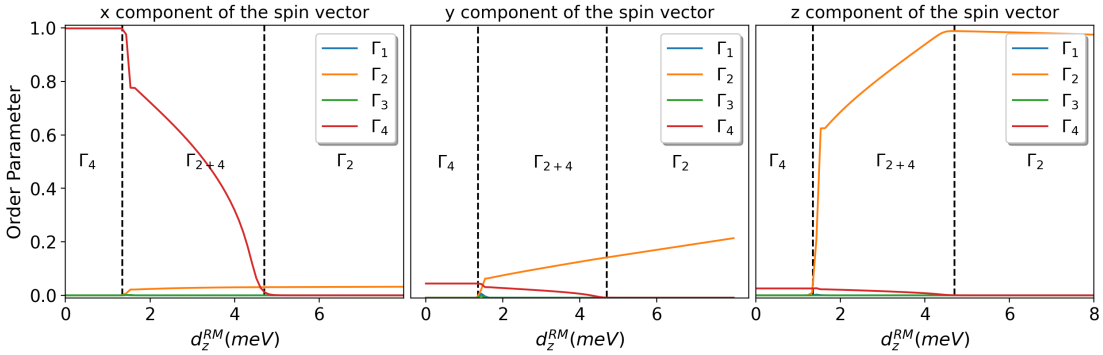

FIGURE 3.6: Decomposition of magnetic ordering on different irreducible representations (Γ_j) for x, y and z directions of the spins in the Γ_4 to Γ_2 SR phase transition case. The calculations are done at 0K (ground state). The horizontal axis shows the magnitude of the z component DMI between R and M sites in the unit of meV and the vertical axis shows the normalised order parameter magnitude. The simulations are done in 0.01 meV grid and the lines are interpolation between the points.

To further understand the SR, we have studied how the stability of the magnetic orders is affected by the value of the DMI coupling between R and M. This allows us to determine how the strength of the interaction between R and M spins influences the SR. Figure. 3.6 shows the equilibrium state of the structure which is projected to the different irreducible magnetic orders along x, y, and z directions versus d_z^{RM}. (The figure presents three components of the spin as projected to different irreducible representations.)

For values of $d_z^{RM} < 1.6$ (meV) we can see that we have the Γ_4 state with the main direction of the spin along x with G-type AFM order (G_x) and small components (canting) of the spins along the y and z directions with A-AFM (A_y) and FM (F_z) ordering respectively. For $4.3(\text{meV}) > d_z^{RM} > 1.6$ (meV) we have a coexisting region that we denote Γ_{24}, where mostly Γ_2 and Γ_4 states are present. The system enters this state through a sudden jump in magnetic order (we also have a discontinuity in the energy of the system). As we move towards higher values of d_z^{RM} the Γ_4 contribution is reduced while Γ_2 contribution increases up to $d_z^{RM} > 4.3$ (meV) where only the Γ_2 is present, the SR being completed. The transition from Γ_2+Γ_4 to Γ_2 at $d_z^{RM} = 4.3$ (meV) is continuous.

To get further insight into this transition, in Fig. 3.7 we show the evolution of the atomic site projection of the spins in x, y, and z components. Since the SR transition is due to the $d_z^{RM} F_{R,x} C_{M,y}$ term in the Hamiltonian, we can observe an increase of the C-type canted order along the y direction as the interaction between R and M becomes stronger. Additionally, since the magnitude of the canted ferromagnetic order on M is constant (FM order along x and z direction before and after SR), this increase in C-type order can only come from a reduction of the G-type order component of the spin.

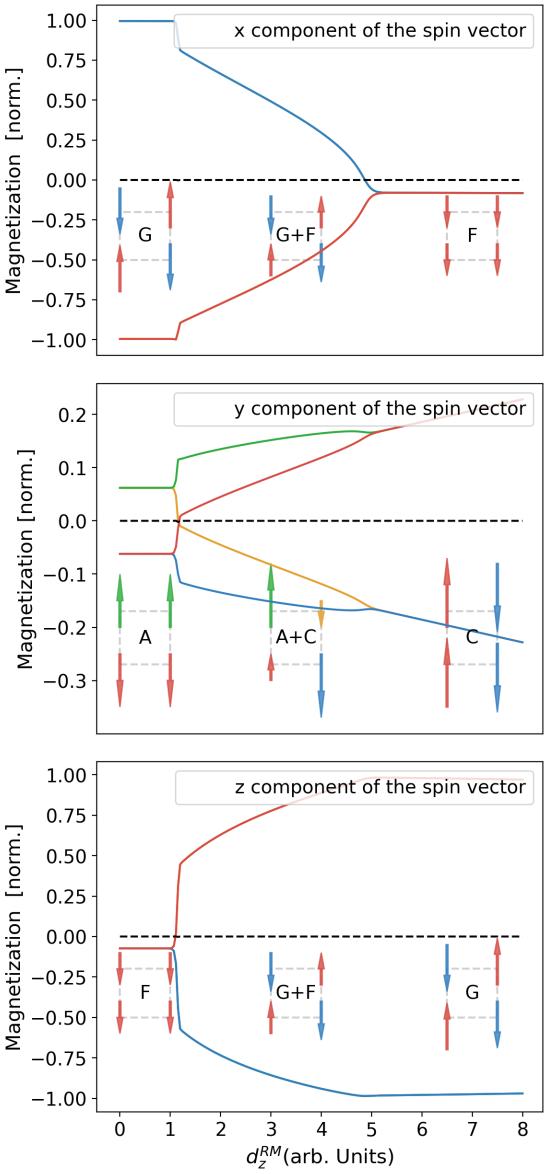

FIGURE 3.7: Plot of the evolution of the x, y, and z projections of the local Fe cation spin components versus the DMI strength between R and Fe cations. A schematic representation of how the Fe spins look like is also given for the three main phases Γ_4, Γ_{24}, and Γ_2. The color of the spins are chosen the same as the magnetization amplitude in the figure. The dashed black line shows the zero of magnetization and is plotted for a guide to the eye. The simulations are done in 0.01 meV grid and the lines are interpolation between the points.

In Fig. 3.8 we show how the different energy contributions of the system (superexchange and DMI) evolve with respect to the d_z^{RM} parameter. We can see that the contributions coming from d_z^M and superexchange interactions between transition-metals are positive and increase as we go from Γ_4 to Γ_2 state, which means that they are against the SR. These interactions are determinants for how fast the SR happens. The superexchange interaction is the main interaction that resists against the SR and this is because the SR involves an increase of the magnitude of C-type order parameter on M sites (via

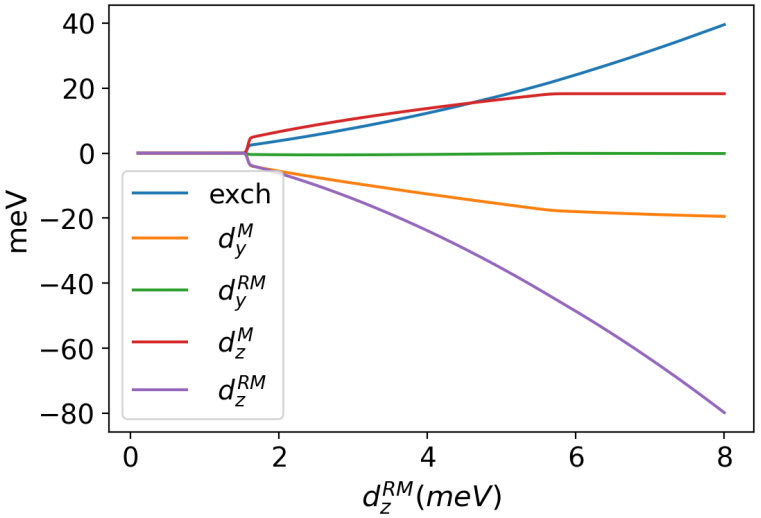

FIGURE 3.8: Decomposition of the total energy from spin dynamics to its components i.e., energy from superexchange interaction (exch), energy from y component of the DMI between M and RM in (d_y^M,d_y^{RM}), and energy from the z component of the DMI between M and RM (d_z^M,d_z^{RM}). The simulations are done in 0.01 meV grid and the lines are interpolation between the points.

$d_z^{RM} F_{R,x} C_{M,y}$, as mentioned above) and the reduction of the magnitude of the G-type order, which costs some energy. Therefore, to overcome this energy penalty we need larger interaction between R and M to complete the SR which is provided by more ordering of the R site atoms.

3.4.1.1 Parameters affecting the Γ_4 to Γ_2 SR

One of the properties that is important to understand is the temperature range in which the spins complete their reorientation. From our model, we found that three parameters affect how fast the SR happens: the DMI d_z^{RM} between R and M cations (related to the ordering amplitude of the R sites), the DMI d_z^M between M cations, and the superexchange interaction J^M between M cations. The ratios between these three parameters drive and determine the energy difference between the Γ_4 and Γ_2 states and hence the temperature range where the SR takes place.

To highlight these parameter effects we report in Figs. 3.9 and 3.10 a two-dimensional (2D) plot showing the presence of the Γ_4, Γ_2 and Γ_{24} regions with respect to d_z^M and d_z^{RM} values at fixed J^M as calculated for $GdFeO_3$. Figure 3.10 shows the same but for a fixed value of J^M corresponding to the one calculated for $GdCrO_3$. As we can see, for too small values of d_z^M the system only experiences an abrupt transition (first-order) between Γ_4 and Γ_2 without any coexisting region and the ratio between d_z^M and d_z^{RM} at which the transition appears is rather constant. However, beyond a critical value of

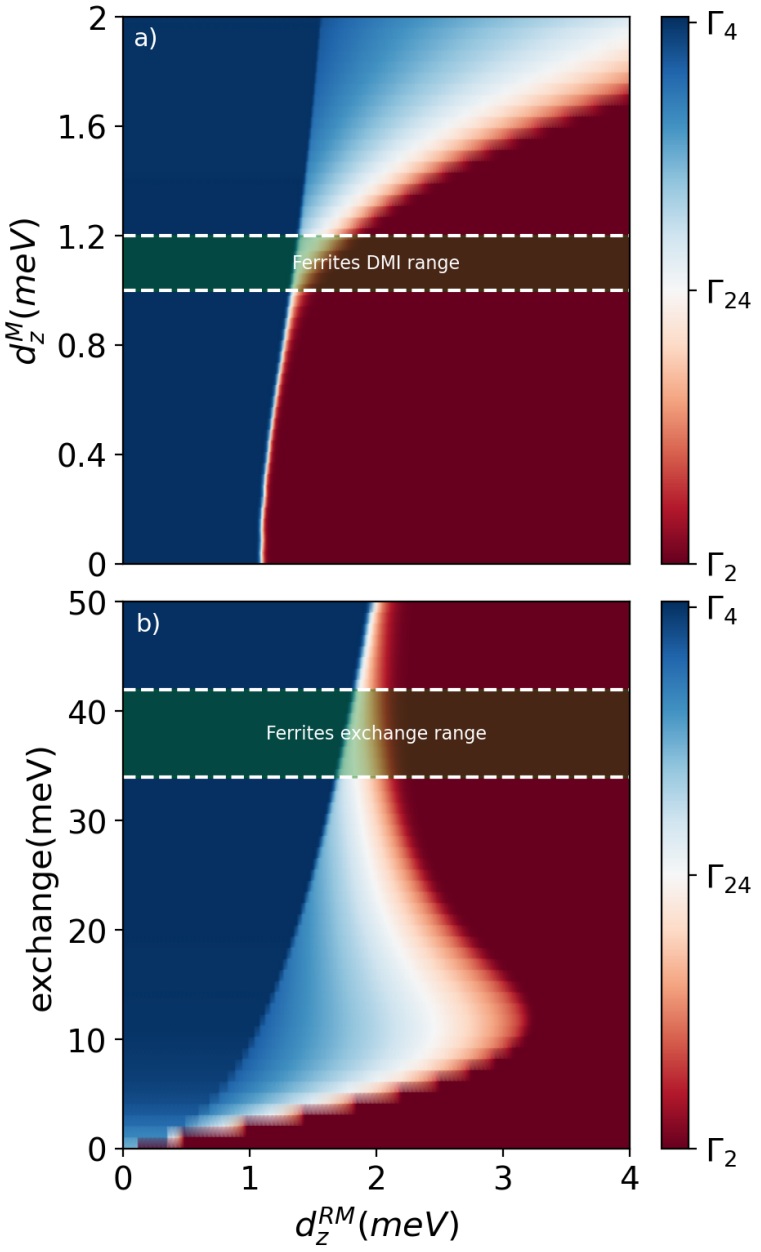

FIGURE 3.9: Phase diagrams for Γ_4 to Γ_2 SR as a function of d_z^{RM} (panel a) and d_z^M with constant superexchange of 38 meV (corresponding to the ferrites) and between d_z^{RM} and superexchange interaction of the transition-metals (panel b) with constant value of 1.1 meV for d_z^{RM} interaction. The dashed lines with green background showing the DMI (panel a) and superexchange (panel b) of iron for the whole range of La family (La to Lu) in $RFeO_3$.

d_z^M a Γ_{24} coexisting region appears and grows with the amplitude of d_z^M. This means that, for a given value of J^M, if d_z^M is not large enough the system will never experience a SR in finite temperature window. Once the coexistence region opens, it grows very fast with d^M such that for large enough d_z^M and d_z^{RM} values a SR in finite temperature window is always guaranteed. On the other side, in Figs. 3.9(b) and 3.10 we can see how the coexisting region area is affected by the value of J^M at a fixed value of d_z^M. Here we

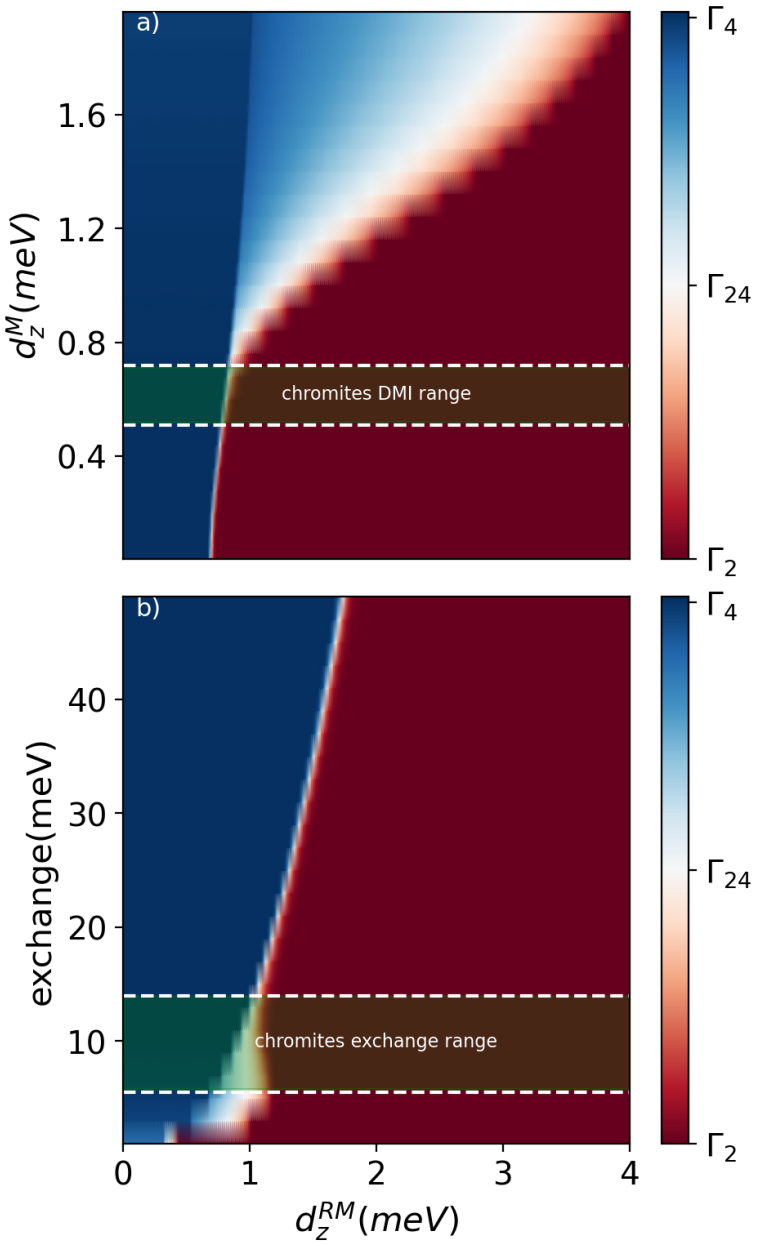

FIGURE 3.10: Phase diagrams for Γ_4 to Γ_2 SR as a function of d_z^{RM} (panel a) and d_z^M with constant superexchange of 9 meV (corresponding to Cr) and between d_z^{RM} and superexchange interaction of the transition-metals (panel b) with constant value of 0.6 meV for d_z^{RM} interaction . The dashed lines with green background showing the DMI (panel a) and superexchange (panel b) of Cr for the whole range of La family (La to Lu) in $RCrO_3$).

can remark that if J^M is too large or too small then the Γ_{24} area is strongly reduced.

In Figs. 3.9 and 3.10 we also draw the maximum and minimum values of d_z^M and J^M as obtained for RFeO$_3$ and RCrO$_3$, respectively, for the whole series of Lanthanides R =La to Lu (horizontal dashed lines). We can see that the range of these parameters is not too large and that they cross small areas of the coexistence region where SR is possible.

We can remark that the SR area for M = Cr is particularly small while it is potentially larger for Fe.

These phase diagrams help if one wants to design engineering of SR speed in these crystals. For example, if a slower SR is desired, the Fe case will be more interesting through doping with atoms that will reduce the superexchange interactions between irons and/or that will increase the DMI between irons (an increase of the wFM).

3.4.1.2 The Γ_4 to Γ_2 rotation in finite temperature window

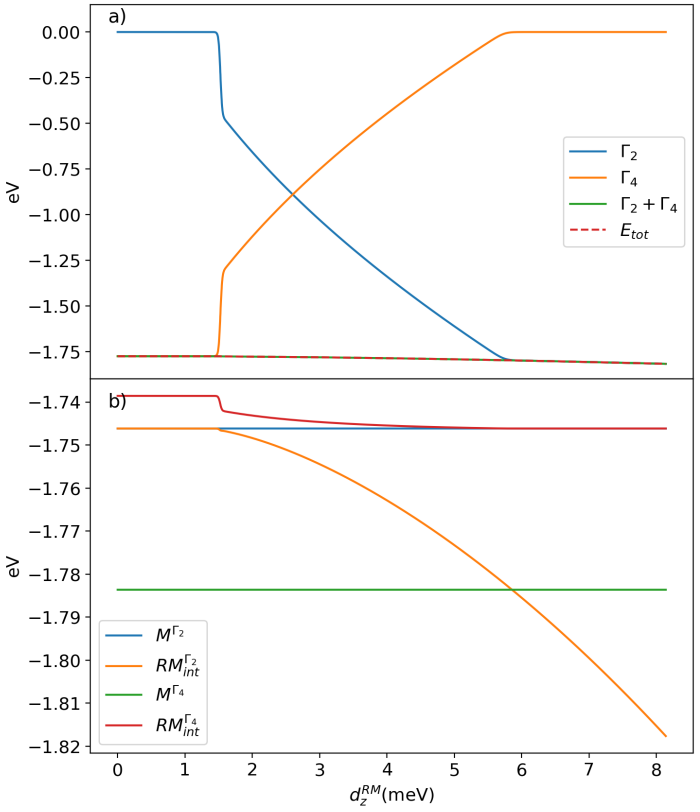

FIGURE 3.11: Decomposition of the energy of the Γ_2 and Γ_4 as a function of d_z^{RM}. (a) Shows the energy of Γ_2 and Γ_4 and $\Gamma_2 + \Gamma_4$ which is the sum of the energies of the two states and E_{tot} which is the total energy from simulations. In b), the energy of each state is decomposed into its pure M sublattice contributions and the interaction contribution between R and M, the pure R-R interactions being neglected. In (b), the zero-energy reference of M and R interactions is taken to be the one of M^{Γ_2}. We can notice that the RM interacting term is the one that lowers the energy of Γ_2 by becoming larger than the energy difference between pure M_4^{Γ} and M^{Γ_2}. The simulations are done in 0.01 meV grid and the lines are interpolation between the points.

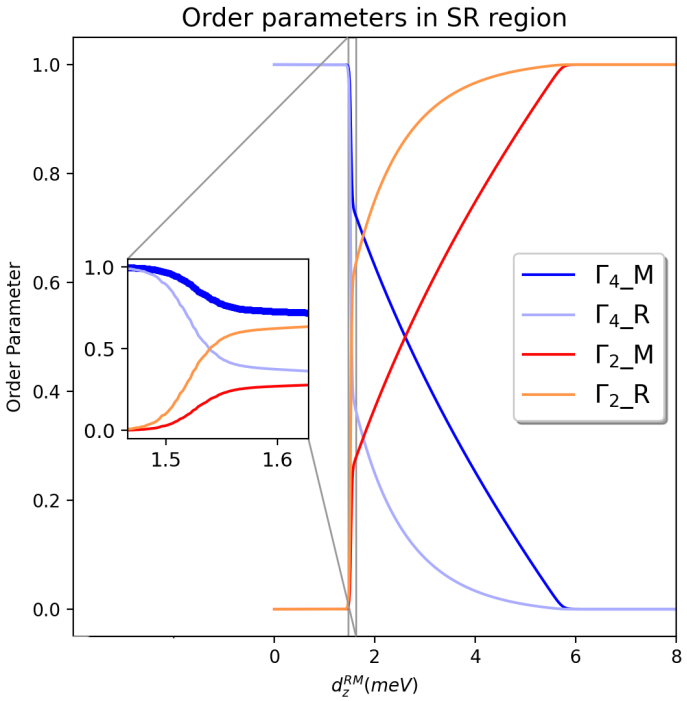

FIGURE 3.12: Order parameter (Γ_2 with orange color and Γ_4 with blue color and gray lines are guide to the eye) decomposition into M and R sublattices when crossing a SR region (here as a function of d_z^{RM}). The inset shows the area where the SR starts and we can notice the change of order of the R site first that drags the M site order afterward. The simulations are done in 0.01 meV grid and the lines are interpolation between the points.

As we show in the analytical part of our model, there is no interaction between Γ_2 and Γ_4, and we have $< \Gamma_2|H|\Gamma_4 >= 0$. This would mean that the transition should be fast from our model since, without interaction between the two states, there is no reason why their coexistence will reduce the energy, and we should have a sharp transition between them. However, our simulations based on this non-interacting Hamiltonian show that a coexisting region exists where both Γ_2 and Γ_4 are present together.

To figure out what is happening, we plot in Fig. 3.11(a) the energy change with respect to the d_z^{RM} as decomposed into a pure Γ_4, pure Γ_2, the sum of the energy of Γ_2 and Γ_4, and total energy from our simulations E_{tot}. To understand if there is hidden coupling between Γ_2 and Γ_4 states, we have plotted the sum of energies of Γ_2 and Γ_4 ($\Gamma_2 + \Gamma_4$) and total energy from our simulations E_{tot} and, as we can see, the two energies match exactly which proves that although there is no coupling between the two states, the SR is slow.

In Fig. 3.11(b) we report the energy decomposition to M sublattice only (M^{Γ_4}, M^{Γ_2}) and interaction between R and M in each state ($RM_{int}^{\Gamma_4}$, $RM_{int}^{\Gamma_2}$,). We can see that the

M sublattice energy of the Γ_2 state (M^{Γ_2}, blue line) is higher than the energy of the M sublattice in the Γ_4 state (M^{Γ_4}, green line), as expected since the Γ_4 phase is the ground state when only the M sublattice is considered. The two $RM_{int}^{\Gamma_4}$ (red line) and $RM_{int}^{\Gamma_2}$ (orange line) interaction terms clearly show that $RM_{int}^{\Gamma_2}$ lowers the energy of the Γ_2 phase with an amplitude that can compensate the energy difference between M^{Γ_4} and M^{Γ_2}, such that the Γ_2 phase can be lower in energy than the Γ_4 phase. This also proves that the M sublattice alone prefers to stay in the Γ_4 state while the R sublattice pushes the M sublattice to be in the Γ_2 state (the $RM_{int}^{\Gamma_2}$ energy is stronger and more negative than the $RM_{int}^{\Gamma_4}$ energy).

In Fig. 3.12 we show the evolution of the order parameters but decomposed into sublattice contributions (Γ_4_M, Γ_4_R , Γ_2_M, and Γ_2_R). We can observe that in the SR region, when going from Γ_4 to Γ_2 the R spins start to rotate first and they drag the M sublattice afterward (highlighted in the inset). Since the M sublattice prefers to stay in the Γ_4 state while the $R-M$ interaction favors the Γ_2 state, the system ends up in a mixed state even if no $\Gamma_2-\Gamma_4$ interaction is present in the Hamiltonian. To understand this better, note that in this problem we do not have two competing orders (Γ_2 and Γ_4), but four (($\Gamma_4(M)$, $\Gamma_4(R)$, $\Gamma_2(M)$ and $\Gamma_2(R)$). As we vary the key Hamiltonian parameter in Fig. 3.12, the $\Gamma_2(R)$ order becomes favorable over $\Gamma_4(R)$; we thus have a $\Gamma_4 \rightarrow \Gamma_2$ rotation of the R sublattice (accompanied by a relatively tiny $\Gamma_2(M)$ component) that yields a reduction of the energy as compared to a pure Γ_4 state. Eventually, the $\Gamma_2(R)$ order grows and drags the M spins to rotate as well, the final result being a pure Γ_2 state.

3.4.1.3 Effect of SIA on Γ_4 to Γ_2 SR

Although the SIA amplitude on the M site is not very large, we can probe it from our model and have an estimate of its effect on SR. To that end, we report in Fig. 3.13(a) the phase diagram of the Γ_4, Γ_2, and Γ_{24} presence with respect to d^{RM} and SIA of M. We can see on this plot that the SIA does not change the Γ_4 to Γ_{24} transition position; in contrast, when the SIA increases, it tends to increase the Γ_{24} SR area at the expense of the Γ_2 state. However, the effect of the SIA is much smaller than the ones of J^M, d^M, or d^{RM} such that it can not affect the temperature window of the SR as other parameters.

3.4.1.4 Summary for the Γ_4 to Γ_2 transition

In summary, in this section, we have shown that our model reproduces well the temperature-dependent SR. This behavior shows that the SR is directly linked to the ordering of the rare-earth in ferromagnetic order and proves that the mechanism behind the SR in

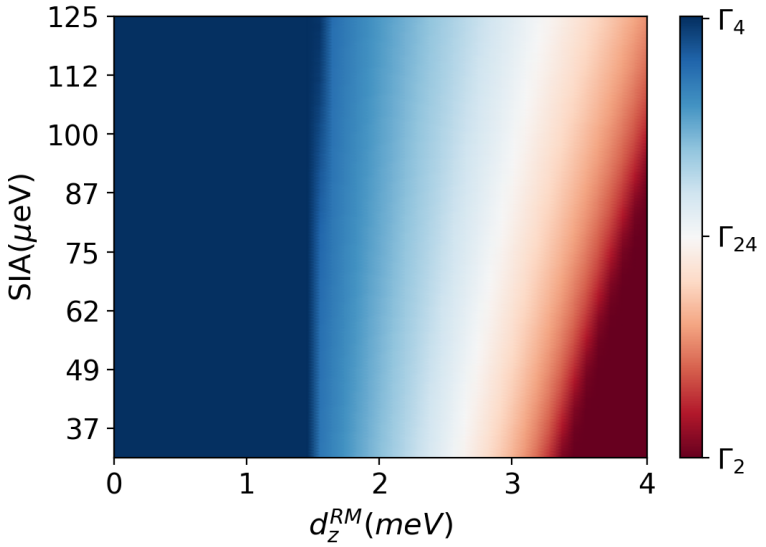

FIGURE 3.13: Effect of SIA on the Γ_4/Γ_2 SR phase diagram. The horizontal axis shows the amplitude of z component of the DMI between R and M sites while the vertical axis shows the amplitude of the SIA of the M site.

RMO_3 compounds is not related to the SIA [92], but it is the DMI between R and M that drives this SR.

A study by Vibhakar *et al.* [149] on triple A-site columnar-ordered quadruple perovskites has shown that the mechanism behind SR in these structures is the competition between DMI and SIA, which is similar to the mechanism that we found to be at play in RMO_3's SR.

In our simulations, we have also studied how different parameters affect the temperature window where the SR happen. We can say that the presence of a smooth transition between Γ_4 and Γ_2 phases through a coexisting region Γ_{24} is very subtle and depends on the ratio between J^M, d_z^M, and d_z^{RM} interactions. If d_z^M is zero, a transition between Γ_4 and Γ_2 can exist but only through a first-order abrupt change; the d_z^M interaction is mandatory to have a smooth SR transition.

3.4.2 Γ_4 to Γ_1 reorientation:

To explain the Γ_4 to Γ_1 SR we need a strong interaction between the R and M sites within the Γ_1 state to allow the M site order to go from its energetically favorable state Γ_4 to the less energetically favorable state Γ_1. If not, we would have each sublattice ordering in different direction like what is observed experimentally in $TbFeO_3$ [106]. However, according to our model, the sole interactions between R and M atoms in the Γ_1 state are $-8Nd_x^{RM}C_{R,z}\bar{G}_{M,y}$ and $-8Nd_y^{RM}C_{R,z}A_{M,x}$. The second term is the coupling between $A_{M,x}$ and $C_{R,z}$, which is small since the $A_{M,x}$ canting is very small

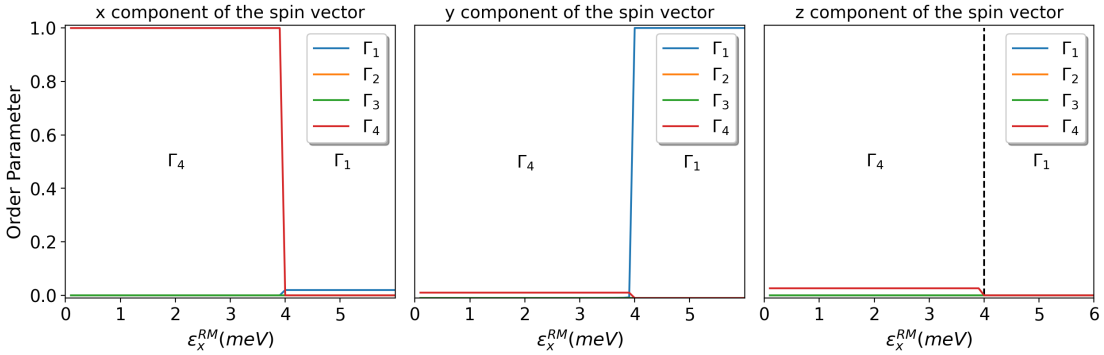

FIGURE 3.14: Magnetic structure for Γ_4 to Γ_1 SR decomposed to different irreducible representations for different components of the spin in x, y, and z directions. The horizontal axis showing the magnitude of ASE in the x direction between R and M and vertical axis showing the order-parameter magnitude normalized. The simulations are done in 0.01 meV grid and the lines are interpolation between the points.

compared to $\bar{G}_{M,y}$. Hence, the only remaining term which can make this SR possible is $-8Nd_x^{RM}C_{R,z}\bar{G}_{M,y}$. From our DFT calculations and from symmetry analysis (since these parameters are originating from $\bar{a}\bar{a}^+c$ oxygen octahedral rotations as discussed in previous section) we know that d_x^{RM} is very small [see Table 3.1] such that it is not possible to explain the Γ_4 to Γ_1 SR using this interaction.

So far we have neglected the anisotropic spin-exchange interactions (ASE) in our model because the effects from these interactions are often negligible with respect to the superexchange or DMI. Now that we have the DMI small too, we will consider the ASE to check whether it can take some importance while the DMI is small. The definitions of DMIs and ASE vector components are as follows:

$$d_x^{ab} = \tfrac{1}{2}(J_{yz}^{ab} - J_{zy}^{zb}) \tag{3.16}$$

$$\varepsilon_x^{ab} = \tfrac{1}{2}(J_{yz}^{ab} + J_{zy}^{ab}), \tag{3.17}$$

where ε_x^{ab} (d_x^{ab}) represents the ASE (DMI) vector component in the x direction between atom a and atom b and J_{yz} is the superexchange interaction between spins directing in the y direction on atom a and in z direction on atom b (another component, i.e., in y and z directions, can be obtained by cyclic permutation of the xyz directions). We can see (from their definitions) that when a component of the DMI vector is small it is possible to have the ASE vector with that component to be big.

In Table 3.2 we show the calculated ASE between Fe and Cr sites. The calculated results show that the x component of the ASE vector is the largest with respect to the y and z components for Fe-Fe and Cr-Cr atom pairs. In Table 3.2 we also report the calculated ASE vector for Fe-Gd and Cr-Gd pairs. The biggest component of the ASE vector is in the y direction for Gd-Fe while it is along the x direction for the Gd-Cr case. We note

TABLE 3.2: Calculated ASE components from DFT of $GdFeO_3$ and $GdCrO_3$ (units are in μeV). ε_i are the ASE vector components along $i = x$, y, and z.

	ε_x	ε_y	ε_z
Fe-Fe	-15	0	0
Cr-Cr	51	0	7
Gd-Fe	6	-16	7
Gd-Cr	-30	10	-9

that the ASE interaction in the Hamiltonian takes the same place as the DMI does, i.e., for the Γ_1 state we have:

$$-8N\varepsilon_x^{RM} C_{R,z} \bar{G}_{M,y} \tag{3.18}$$

$$8N\varepsilon_y^{RM} C_{R,z} A_{M,x} \tag{3.19}$$

Considering these ASE interactions, we can say that the Γ_4 to Γ_1 SR can happen through the x component of the ASE (through $-8N\varepsilon_x^{RM} C_{R,z} \bar{G}_{M,y}$ interaction), which will take the place of the DMI when the latter is small. This conclusion is in agreement with Zvezdin [150] who explained the origin of the Γ_4 to Γ_1 SR to originate from ASE.

We will now study this SR by tuning the ε_x^{RM} ASE coupling in our model. In Figs. 3.14 and 3.15 we report how the relative Γ_4 and Γ_1 stability evolves with respect to the ε_x^{RM} parameter at 0 K (ground state). In contrast to the Γ_4 to Γ_2 transition, we can see that there is no coexisting region between Γ_4 and Γ_1 states, the transition is always first order with respect to the ε_x^{RM} amplitude. To confirm this, we also explore in Fig. 3.14 how the superexchange parameter J^M affects the Γ_4 to Γ_1 SR transition. We can clearly see that whatever value of J^M we considered, the Γ_4 to Γ_1 SR is always abrupt without any coexisting region. We can also remark that J^M favors the Γ_1 state with respect to the Γ_4 state, which can be logically understood by the fact that in the Γ_1 phase all the directions are AFM and, since the torque creating this SR is acting on $G_{M,y}$ (in contrast to Γ_4 to Γ_2 SR where the torque is acting on $C_{M,y}$), the cantings are smaller than in the Γ_4 state. Hence, unlike the Γ_4 to Γ_2 case, the SR involving Γ_1 happens as soon as the system overcomes the energy difference due to ASE and SIA between the two states, making this transition first order.

We also need to mention that this mechanism explains the Ising-type nature (strong anisotropic) of the Γ_1 state [150]. Since the force creating this SR is acting between G-type order of M site and C-type order of R site (i.e., $-8N\varepsilon_x^{RM} C_{R,z} \bar{G}_{M,y}$), the M atoms in Γ_1 state will have a very small canting compared to other states and the spins will mainly order in the G_y type, hence closer to an Ising-type nature.

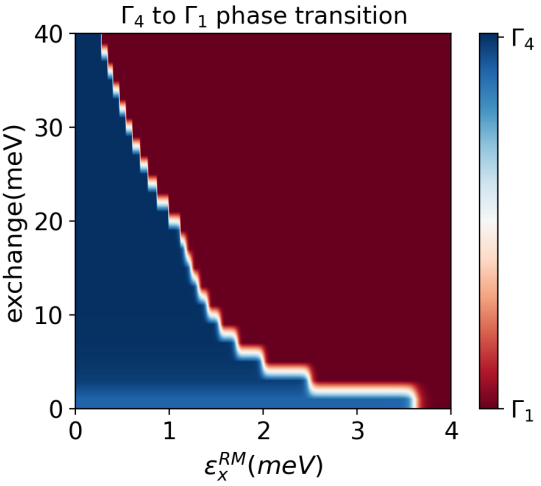

FIGURE 3.15: Phase diagrams of Γ_4 to Γ_1 transition by plotting superexchange on transition-metal sites (J^M) vs the anisotropic exchange ε_x^{RM}. We can see that the SR transition is abrupt for the whole range of superexchange.

3.5 Conclusion

We have studied in this chapter the microscopic mechanism behind the SR and MR magnetic behaviors of the RMO_3's through a Heisenberg model where we considered the superexchange interactions and DMI between the transition-metal sites, as well as between the rare-earth (R) and transition-metal sites (M), and we neglected the superexchange and the DMI between the R spins as they are much smaller than the other interaction parameters.

We conclude that there are two interactions polarizing the R atom site, i.e., (i) the superexchange between M sites (through its wFM) and R sites and (ii) the DMI between R and M, which can result into two effects. Indeed, we can have that both interactions polarize the R element parallel to the M wFM canting direction such that there will be no MR but an amplification of the total magnetization of the crystal [see Fig. 2.7]. We can also have that both interactions polarize the R element in the opposite direction to the wFM of the M cation such that the total magnetization amplitude can be reduced up to a critical temperature below which its sign changes [see Fig. 2.7]. The change of sign appears when the negative R cation magnetization compensates the positive one of the M site (wFM).

Our analysis of the SR transitions has shown that the Γ_4 to Γ_2 transition similarly comes mainly from the DMI interactions between the M and R site but it can be weighted by the superexchange between the M sites. We found that within a relatively wide range of these three interactions this SR transition is smooth and happens through a mixed state where the Γ_4 and the Γ_2 phases coexist. How broad is the temperature range in which

the SR takes place through the Γ_{24} mixed state depends on a subtle ratio between DMI and superexchange interactions between M sites, which can vary depending on the rare-earth and transition-metal cations that are present in the $Pbnm$ perovskite structure. We also found that the Γ_4 to Γ_1 SR transition depends on even more subtle interactions (anisotropic superexchange that acts as the DMI) but, contrary to the Γ_4 to Γ_2 SR, it never presents a coexisting region, i.e., it always proceeds through an abrupt change.

The model we have presented can help in designing the strength and amplitude of SR and MR in RMO_3 through, e.g., doping, strain, or pressure that would tune the ratio between the key interactions as desired. Our model can also be easily extended by including the interactions between the rare-earth spins to study the complex magnetic phase diagrams below the Néel temperature of the rare-earth sublattice. It can be enlarged too with the anisotropic exchanges (important for the Γ_4 to Γ_1 SR) [150] or with a four-spin interaction term, which is important in rare-earth manganites [151]. Because it contains all the key interactions that allow describing most of the important magnetic properties of RMO_3 compounds, the model can be used to study dynamically magnetic domain walls. Going beyond, the model can be coupled with a lattice model (second principles [152, 153]) to have access to a full atom plus spin dynamics for the simulations of, e.g., recent ultrafast laser excitation experiments made on these crystals [154–156].

Chapter 4

Origin of nonlinear magnetoelectric response in GdFeO3

4.1 Introduction

In this chapter, we report a simulation study of the microscopic origin of the large non-linear ME response of $GdFeO_3$. Experimentally it has been observed that the polarization can go from 0.12 $\mu C/cm^2$ to 0 $\mu C/cm^2$ under an applied magnetic field of 3.7 T [see Fig. 2.15 and 2.16] [80]. If we extrapolate an effective linear response in the unit of ps/m by calculating $\frac{\Delta P}{\Delta B}$ between 0 and 3.7 T, we obtain an effective amplitude of about 406 ps/m, i.e the same order as in the linear ME crystal $TbPO_4$ (730 ps/m among the largest linear ME responses)[157]. Although this response is not the strongest non-linear ME response reported in materials [158, 159], understanding its microscopic mechanism will help in designing and engineering other ME materials. To tackle this problem from a simulation viewpoint, we first derive an analytical form of the ME response of this material using both Heisenberg Hamiltonian and DFT calculations to fit the parameters [For the technical detail see Appendix B.2]. Then, we report the results obtained through classical spin dynamics to calculate the ME response and the polarization of these materials under an applied magnetic field. Our results reproduce the response observed experimentally on $GdFeO_3$, i.e., the fully non-linear response and the appearance of two regimes, associated with a magnetic phase transition under the applied magnetic field.

4.2 Theoretical derivation

In this section, we derive an analytical expression of the ME response of the $GdFeO_3$. This ME response is originating from the exchange striction. To derive the ME response, we use the fact that interaction between the G-type (or A-type) magnetic order of the rare-earth site and G type order on Fe sublattice is the driving force that breaks the inversion symmetry and causes the polarization in rare-earth orthoferrites [47, 80, 139]. Hence, we will consider the polarization to be a function of the rare-earth site G-type order such that we can expand the polarization in terms of the corresponding order parameter (Fe G type is considered as constant). From this assumption, we can write the ME response in these structures using the following relations (Einstein summation rule applies):

$$\frac{\partial P_i}{\partial B_l^{app}} = \frac{\partial P_i}{\partial G_j^R}\frac{\partial G_j^R}{\partial B_l^{app}}, \tag{4.1}$$

where B_l^{app} is the applied magnetic field in the l direction, P_i is the polarization in the i direction and G_j^R is the magnitude of the G-type order on rare-earth site in the j direction.

To probe the variation of G-type order with respect to the magnetic field, $\frac{\partial G_j^R}{\partial B_l^{app}}$, we use the general Heisenberg model developed by us for RMO_3 crystals (R = Rare-earth, M = Fe or Cr) [160] but using the data fitted from DFT calculations done on $GdFeO_3$.

In deriving the ME response from theory, we have neglected the changes in Fe sublattice. The effect of magnetic field on Fe sublattice is to change the AFM order to FM order on Fe atoms and it competes with exchange interactions between Fe atoms. Fe sublattice has a Néel temperature of more than 600K. This corresponds to an effective magnetic field from exchange interactions on the order of 10^2 T. The estimated effective field is much larger than the fields relevant in this work. So, we can neglect the Fe sublattice changes in our theoretical model and consider its magnetic order as G type in the x-direction from now on. According to our spin dynamics simulations also, the magnetic order on the Fe sublattice is not affected by the range of magnetic fields that we are interested in (see Fig. 4.3).

The energy of rare-earth spins per formula unit can be derived from the Heisenberg Hamiltonian to obtain:

$$H_{Heis}^R = -3J^R(G_i^R)^2 + 3J^R(F_j^R)^2 - K^R(G_i^R)^2 - B_l^{app}F_j^R\delta_{jl} - B_n^{RM}F_j^R\delta_{mj}, \tag{4.2}$$

where J^R is the exchange interaction between rare-earth sites and G_i^R and F_j^R are the G-type AFM and FM orders on rare-earth in the i and j directions respectively, K is the single-ion anisotropy in the i direction. The interaction of Gd and Fe spins can be reduced to an effective magnetic field B_n^{RM}, which can be written as follows (see chapter 3) [99, 160]:

$$B_n^{RM} = 8J^{RM}F_n^M + 8(d_y^{RM}G_{n'}^M), \tag{4.3}$$

This formula represents the effective field in n direction on Gd sublattice from Fe. J^{RM} is the exchange interaction between Gd and Fe and the d_y^{RM} is the y component of Dzyaloshinskii-Moriya interaction (DMI) between rare-earth and transition metal cations (DMI has the largest component in y direction see chapter 3 [160]). $G_{n'}^M$ represents G-type order in direction n' that is prependicular to n and y. We consider the effective magnetic field B_n^{RM} to be in the same direction as the applied magnetic field, or small compared to it such that it can be neglected. In the case where the applied field is in the z direction and the rare-earth orders in the G type in x direction, the B_n^{RM} and the applied magnetic field are in the same direction [99, 160]. When the applied field is in the x direction, B_n^{RM} and the applied field are perpendicular to each other before the phase transition (in which we can consider B_n^{RM} to be negligible compared to the applied magnetic field), while after the phase transition they will be in the same direction.

We can minimize the energy with the following constraint using Lagrange multipliers (the constraint is coming from considering the magnitude of the spin as normalized with spin magnetic moments of each atom, i.e., $\frac{5}{2}\mu_B$ for Fe and $\frac{7}{2}\mu_B$ for Gd):

$$(G_i^R)^2 + (F_j^R)^2 = 1, \tag{4.4}$$

which gives us the G_i and F_j orders as a function of the applied magnetic field:

$$G_i^R = \pm\sqrt{1 - \left(\frac{B_l^{app}+B_l^{RM}}{12J^R+2K^R}\right)^2} \tag{4.5}$$

$$F_l^R = \frac{B_l^{app}+B_l^{RM}}{12J^R+2K^R}. \tag{4.6}$$

From these expressions we can obtain the following term:

$$\frac{\partial G_j^R}{\partial B_l^{app}} = \mp\frac{\frac{B_l^{app}+B_l^{RM}}{(12J^R+2K^R)^2}}{\sqrt{1-\left(\frac{B_l^{app}+B_l^{RM}}{12J^R+2K^R}\right)^2}}. \tag{4.7}$$

Now, we are left with the determination of the variation of P with respect to G_j^R: $\frac{\partial P_i}{\partial G_j^R}$.

Because the exchange striction between the rare-earth site and the transition metal site is the interaction responsible for polarizing the material [80, 139] we are going to use the energy expression for this interaction to derive the $\frac{\partial P_i}{\partial G_j^R}$. To derive this expression we are going to use the energy expression which is written as a function of change in exchange interaction due to atomic displacement and elastic potential that resist against this deformation as:

$$E_{int} = -4G_i^R G_j^M \epsilon_l^{ij} \Delta r_l^{ij} + \tfrac{1}{2} k (\Delta r_l^{ij})^2 \tag{4.8}$$

where the change in exchange interaction (J_{ij}^{RM}) between R and M atoms is written as $\epsilon_l^{ij} \Delta r_l^{ij}$ (changes of J_{ij}^{RM} expanded to linear order). In this relation the ϵ_l^{ij} is the constant of proportionality and Δr_l^{ij} is the magnitude of change of l component of the position vector between atoms. k in this equation shows the elastic constant. By minimizing the Eq. 4.8 we can have the equilibrium displacement as:

$$\Delta r_l^{ij} = \epsilon_l^{ij} \tfrac{4G_i^R G_j^M}{k} \tag{4.9}$$

If we expand the l component of the polarization to linear order on atomic displacement from center of symmetry, we can write it as:

$$P_l = \zeta_l^{ij} \Delta r_l^{ij} \tag{4.10}$$

From Eq. 4.10 and Eq. 4.9 we can write the polarization in l direction as:

$$P_l = 4\delta_l^{ij} G_i^R G_j^M \tag{4.11}$$

Where we have used the $\delta_l^{ij} = \frac{\zeta_l^{ij} \epsilon_l^{ij}}{k}$. In this equation we can neglect the anisotropic symmetric exchange, i.e., $i \neq j$. These interactions are negligible compared to the other interactions in $GdFeO_3$ [160]. Hence, we can write the polarization for isotropic exchanges as:

$$P_i = 4\delta_i^{jj} G_j^R G_j^M \tag{4.12}$$

In this case we have:

$$\frac{\partial P_i}{\partial G_j^R} = 4\delta_i^{jj} G_j^M, \tag{4.13}$$

To determine the strength of the change of polarization as a function of the magnitude of the G-type AFM ordering of rare-earth (as Eq. 4.13), we performed DFT calculations. We have calculated the polarization for different magnetic ordering of Gd atoms by changing their spin order from G-type order in x direction to FM order in z direction by

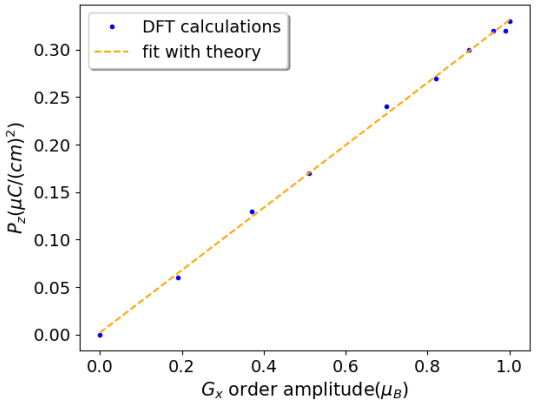

FIGURE 4.1: Polarization of the $GdFeO_3$ as a function of magnitude of G-type order in the material. The x-axis represents the magnitude of G-type order normalized to 1 (Fully G-type=1) as we rotate it to F-type order (G=0 for fully ferromagnetic Gd atoms) using constraint DFT calculations. We also have shown the fitted line with the theory.

rotating it slowly [see Appendix B.2 for the detail of calculations]. In Fig. 4.1 we report the results, i.e., the change of polarization as a function of the G-type order magnitude of Gd atoms as we go from G-type to the FM order. We can notice the linear relation between G-type order magnitude and the polarization, which proves that the Eq. 4.12 is a good estimation of the polarization of the materials as a function of G-type order magnitude.

By fitting the Eq. 4.13 with the results of Fig. 4.1, we can extract the coefficients of this equation. We obtain a slope of 0.328 $\mu C cm^{-2} \mu_B^{-1}$ with the polarization in the z direction which is perpendicular to G_x type magnetic ordering (from now on we will consider the polarization in the z direction). Hence we have:

$$\frac{\partial P_z}{\partial G_x^R} = 4\delta_z^{xx} G_x^M = 0.328\ \mu C cm^{-2} \mu_B^{-1} \tag{4.14}$$

for $GdFeO_3$. With this coupling term at hand, we can explore how the crystal responds to an applied magnetic field with the Heisenberg model and deduce how the polarization changes, i.e. the ME response. We use the same applied field conditions as reported experimentally for $GdFeO_3$ by Tokunaga *et. al.* [80].

We can now have following analytical expression for the ME response (in the following equations we are considering $B_l^{eff} = B_l^{app} + B_l^{RM}$):

$$\frac{\partial P_z}{\partial B_l^{app}} = \mp \frac{4\delta_z^{jj} G_j^M \frac{B_l^{eff}}{(J_P)^2}}{\sqrt{1 - \left(\frac{B_l^{eff}}{J_P}\right)^2}} \tag{4.15}$$

In this equation we consider $B_l^{eff} < J_p$ with $J_p = 12J^R + 2K^R$. This means the system is not completely ferromagnetically ordered. This assumption is a good assumption since we are studying the response of the system in this regime. We can expand the ME response in Eq. 4.15 around zero applied magnetic field as follows:

$$\frac{\partial P_z}{\partial B_l^{app}} = \mp \frac{4\delta_z^{jj} G_j^M \frac{B_l^{eff}}{(J_p)^2}}{\sqrt{1-\left(\frac{B_l^{eff}}{J_p}\right)^2}} = \mp 4\delta_z^{jj} G_j^M \frac{B_l^{eff}}{(J_p)^2}\left(1 + \frac{1}{2}\left(\frac{B_l^{eff}}{J_p}\right)^2 + \frac{3}{8}\left(\frac{B_l^{eff}}{J_p}\right)^4 + ...\right), \tag{4.16}$$

where the negative and positive signs are for the positive and negative direction of the applied magnetic field respectively.

Our derivation gives us the ability to understand the origin of non-linear behavior. Since ME calculated from two terms, (i.e., $\frac{\partial P_i}{\partial G_j^R}$ and $\frac{\partial G_j^R}{\partial B_l^{app}}$) we can see that the ME response is non-linear because the AFM order changes non-linearly under an applied magnetic field (i.e., $\frac{\partial G_j^R}{\partial B_l^{app}}$ term) and we can expect this non-linear behavior for all the cases where the AFM order breaks the inversion symmetry (this should be the case for A-type AFM order and E-type AFM order). While the AFM order creates a non-linear ME response, the FM order that drives ferroelectricity will have a linear ME response before magnetization saturation (since the FM order changes linearly with respect to the applied magnetic field, see Eq. 4.6). Another point to mention is the fact that the A-type AFM ordering of the rare-earth site can also break the inversion center in these structures and can induce nonlinear polarization. If we consider the ME response from this ordering we should change the denominator $12J^R$ by $4J^R$ in the ME response.

If we integrate Eq. 4.15 with respect to the magnetic field, we can calculate the polarization as a function of the magnetic field for these materials using the initial values obtained from DFT. This integration gives the following final analytical expression:

$$\begin{aligned} P_z(B_l^{app}) &= 4\delta_z^{jj} G_j^M \left(\sqrt{1-\left(\frac{B_l^{eff}}{J_P}\right)^2}\right) \\ &= 4\delta_z^{jj} G_j^M G_j^R \end{aligned} \tag{4.17}$$

In the second equation, we are using Eq. 4.5. Now that we have analyzed analytically the ME response of rare-earth perovskites in the magnetic phases as present in ferrites and chromites, in the next section we present our numerical results coming from the simulations for $GdFeO_3$.

4.3 Simulations

In this section, we present the results of the spin dynamics simulations to study numerically the effect of the applied magnetic field on magnetism and the resulting ME response. For $GdFeO_3$, the magnetic ground state is Γ_4 as shown in Fig. 4.2(b) in which the main spin component is in AFM order in the x direction (i.e., $G_xA_yF_z$ for Fe and G_xF_z for Gd) and it has a small FM canting in the z direction (i.e., F_z). When the magnetic field is applied in the z direction, the magnetic ordering of the Gd sublattice changes slowly from G_x type to F_z while the magnetic symmetry does not change. When the applied magnetic field is in x direction, the magnetic field induces an FM order in the x direction which is not allowed by symmetry in Γ_4 magnetic state. So, by increasing the magnitude of the applied magnetic field, the energy from $F_x.B_x^{app}$ interaction increases, and once this energy is large enough to compensate the energy difference between two magnetic states (i.e., Γ_2 and Γ_4) a phase transition takes place for Gd sublattice from Γ_4 to Γ_2 ((Fig. 4.2(a)). In this phase transition the order for Fe sublattice stays in $G_xA_yF_z$ and for Gd sublattice changes to F_xG_z). This spin-flip phase transition can be seen as a change in magnetic anisotropy for the Gd sublattice from the x to the z direction. We will present the results for two different regimes (B_z^{app} and B_x^{app}) in the two following sections.

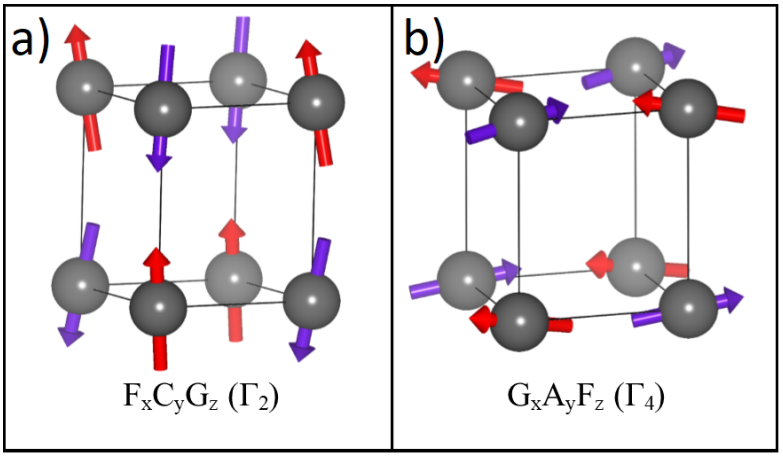

FIGURE 4.2: Schematic presentation of the two magnetic phase a) Γ_2 and b) Γ_4. In his figure the G type shows the main spin component with its direction presented as subscript and other letters in the presentation showing the canting due to DMI

.

4.3.1 Magnetic fields perpendicular to the Gd G-type order direction

In this part we discuss the ME response of $GdFeO_3$ as a function of the magnetic field applied perpendicular to the direction of the Gd spins with G-type order.

In Fig. 4.3(a) and Fig. 4.3(b) we show the spin dynamics results of the effect of an external magnetic field on Fe sublattice. We notice that the Fe sublattice does not change much as the magnetic field is applied to the structure, we can only observe a small change in its weak FM canting (see Fig. 4.3(b)). This result shows that we can neglect the Fe magnetic order changes effects on the ME response since the effects for Gd sublattice are much larger.

In Fig. 4.3(c) and Fig. 4.3(d) we report the effect of the applied magnetic field in the z direction on the Gd sublattice. We can see a continuous decrease of the G type ordering along the x direction and an increase of the F type along the z direction. Hence, the applied magnetic field can fully magnetize the Gd parallel to the field direction. Beyond a critical field of 4 T, we can see that the ground state G type AFM order has disappeared, the magnetic field having fully magnetized all the Gd moments in the same direction. This transition is fully consistent with the experimental results of Ref. [80].

To check the consistency of the spin dynamics results with the analytical solution that we have obtained in the previous section, we fitted the results of the FM order (z component of the Gd spin) with Eq. 4.6 to obtain the J^R, K^R and B_l^{RM} parameters. The orange dashed line in Fig. 4.3(d) shows the resulting fit that is in good agreement with the spin dynamics results (blue dots). We then used these parameters and put them in Eq. 4.5 and plotted the results in Fig. 4.3(c) for the x component of the Gd spin. The values for the parameters obtain from the fit with spin dynamics are close to the values calculated from DFT. As we can see these results agree well with the spin dynamics simulations.

Having calculated the required coefficients for the magnetic response, we can calculate the ME response. In Fig. 4.4 we report the evolution of the change of polarization versus the applied magnetic field. We can see that the change of polarization response is negative (i.e. the magnetic field reduces the polarization), symmetric for each magnetic field direction, and diverges when approaching the critical field where the Gd order goes from G_x to F_z. This critical field is directly related to the amplitude of the Gd exchange interaction (J^R), which governs the energy change associated with the change of the Gd magnetic order (here from G to F type). This corresponds to the phase transition from the polar $m'm2'$ ($Pna2_1$) phase to the para-electric $m'm'm$ ($Pbnm$) phase

In Fig. 4.5 we report the ME response decomposed into its different expansion orders as made in Eq. 4.16. We can see that close to zero magnetic fields the response is mainly driven by its linear term (second-order ME response) but as we are going with higher magnetic field amplitudes the higher-order non-linear responses become more and more important.

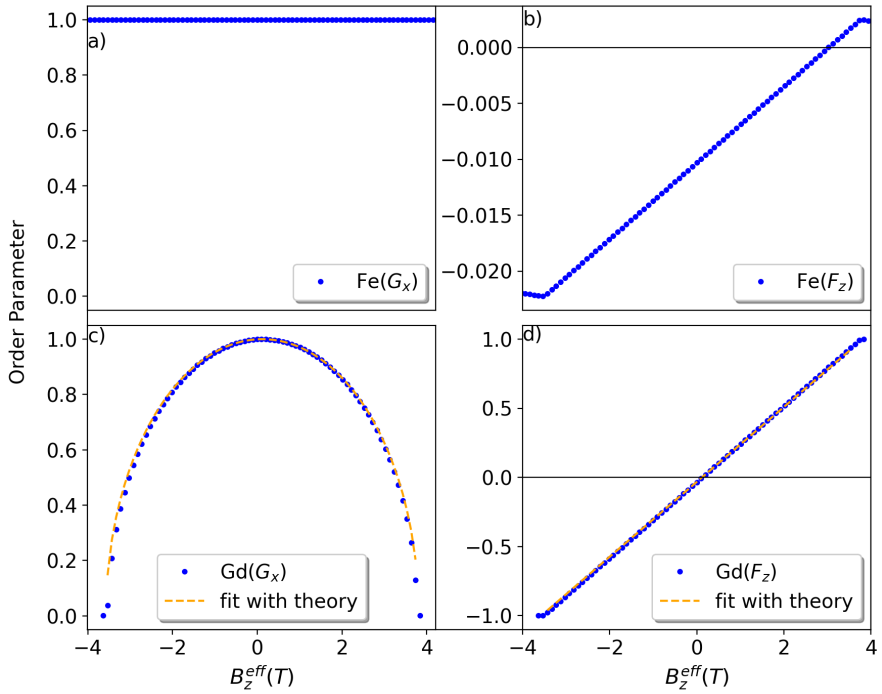

FIGURE 4.3: Fe and Gd site magnetic ordering for spins in x and z direction as a function of applied magnetic field in z direction. Panel (a) presents the Fe sublattice magnetic order in x direction which G-type here, and panel (b) presents z component of the spins in Fe sublattice which is FM order. Figure (c) and (d) represents the x component (G-type) and z component (FM order) for Gd sublattice.

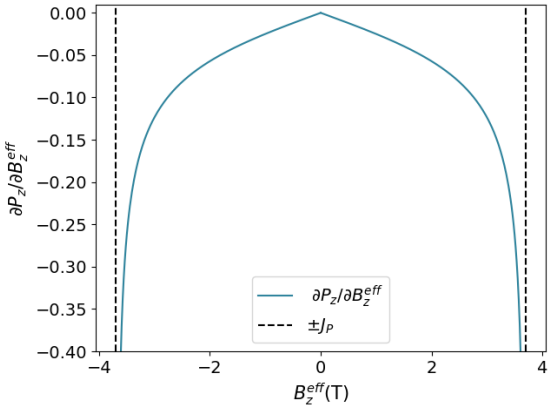

FIGURE 4.4: Non-linear Magneto electric response of $GdFeO_3$ orthofrrites plotted according to Eq. 4.15 where we can see a divergence in the response as applied magnetic field strength get closer to J_p

In Fig. 4.6 we show the polarization versus the magnetic field of $GdFeO_3$ as obtained from Eq. 4.17. We obtain that the polarization decreases non-linearly for both directions of the field and reaches zero at the critical magnetic field where the crystal goes to the *Pbnm* paraelectric phase. In this figure, we have also included the magnetization of the crystal coming from the Gd where we can see that when the Gd sublattice is ferromagnetically ordered, the polarization vanishes. This result is in very good agreement with the

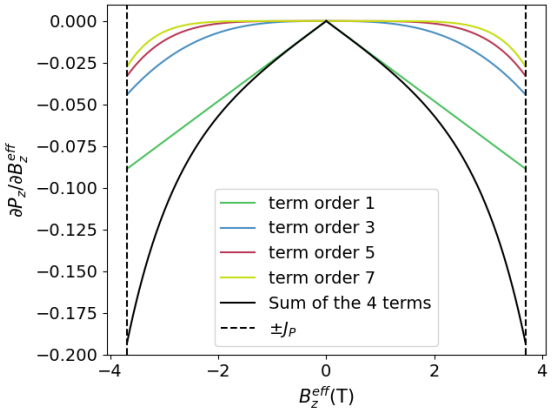

FIGURE 4.5: Non-linear Magneto electric response of Gd orthoferrites plotted according to Eq. 4.16 for different orders of the equation where we can see that the divergence is mainly coming from higher order terms in response of the material

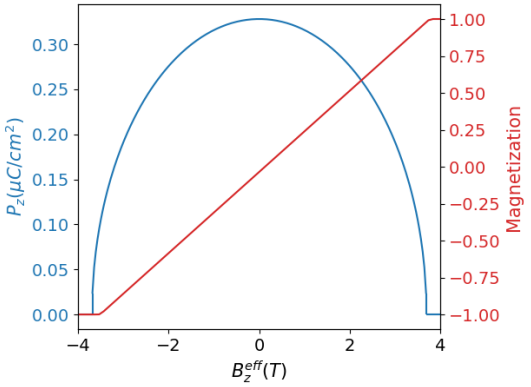

FIGURE 4.6: Polarization as a function of the magnetic field for $GdFeO_3$ where it reaches to zero as the applying magnetic field strength reaches that of exchange interaction between Gd (J^R), and magnetization of the Gd (red line)

experimental results of Tokunaga et al. [80], which also proves that our model describes correctly the ME response of this material.

4.3.2 ME response for magnetic field parallel to the Gd G-type order

In this section we discuss the ME response of $GdFeO_3$ for an applied magnetic field parallel to the direction of the Gd G-type magnetic order. Similar to the applied field along the z direction, our simulations give that the magnetic ordering of the Fe site is not strongly affected by the applied magnetic field along the x direction such that we can neglect it. In Fig. 4.7 we report the evolution of the Gd sublattice spin from spin dynamics when we apply a magnetic field in x direction. We can see that for a critical magnetic field of about 0.7 T, the Gd goes thorough a spin-flip phase transition from the Γ_4 state with G-type order in x direction (orange line) to the Γ_2 state with the G-type order along the z direction (blue line). In this structure, the Gd atoms prefer to

be in Γ_4 state due to single-ion anisotropy and the effective field of Fe. By applying a magnetic field in the x direction, we lower the energy of the Γ_2 state by $B_x.F_x$ (where F_x is a weak canted moment characteristic of the Γ_2 state) and once this energy is larger than the energy difference between Γ_4 and Γ_2 we will have a phase transition. Beyond this phase transition, the Gd spins start to be more and more FM and it becomes fully magnetized for the amplitude of the 4 T magnetic field.

As done previously for the applied field along the z direction, we can also calculate how the polarization is affected by the applied field along the x direction and so the ME response. In Fig. 4.8 we report the evolution of the polarization versus the applied magnetic field along x. We encounter a non-linear ME response again where the polarization is decreased for both directions of the field. We, however, observe two regimes, one between 0 and ±0.7T where the polarization is approximately constant and not affected by the field. Exactly at ±0.7 T, we observe a sharp polarization drop (from 0.36 $\mu C/cm^2$ to 0.05 $\mu C/cm^2$, a reduction by a factor of 5 (calculated from DFT) due to the transition of Gd sublattice from the Γ_4 to the Γ_2 phase.

Then, beyond ±0.7T we have a non-linear further reduction of the polarization down to zero when the Gd is fully magnetized by the field along the x direction. The polarization will change like Eq. 4.17 for the range of fields between 0.7 T and 4 T with a different exchange coupling: in the first case (where we apply the magnetic field in z direction) we had both Gd and Fe atoms main spin component in the x direction and we were considering $\delta_z^{xx} = \frac{\zeta_z^{xx}\epsilon_z^{xx}}{k}$; instead, now we will have $\delta_z^{zx} = \frac{\zeta_z^{zx}\epsilon_z^{zx}}{k}$ (Fe in G-type ordering in the x direction and Gd in G-type ordering in z direction) which is much smaller than the first δ_z^{xx} hence resulting in a smaller polarization for this part. The ME response will also be similar to Eq. 4.15 for magnetic fields higher than 0.7 T.

Again, our results reproduce well the experiments of Tokunaga et al.[80] where two regimes of non-linear ME response were also observed with a polarization drop around the critical field of 0.7 T and a disappearance of the polarization beyond a critical field of about 4 T.

4.4 Conclusion

In this chapter, we have analyzed the magnetoelectric response of the rare-earth orthoferrite perovskite oxides through theoretical methods based on DFT calculations, Heisenberg, and analytical models taking into account the exchange striction that induces the polarization. With this analysis, we have shown that the non-linear character

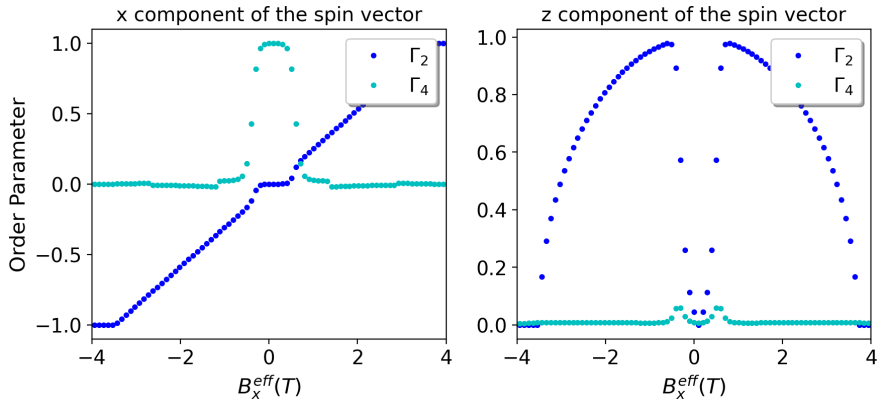

FIGURE 4.7: Re site magnetic ordering as a function of applied magnetic field in x direction. For the magnetic field of less than 0.7 T we can see the sudden drop of G-type order in x direction (the orange line in x component of spin) which is accompanied by a increase in G-type order in z direction (blue line in z component of spin)

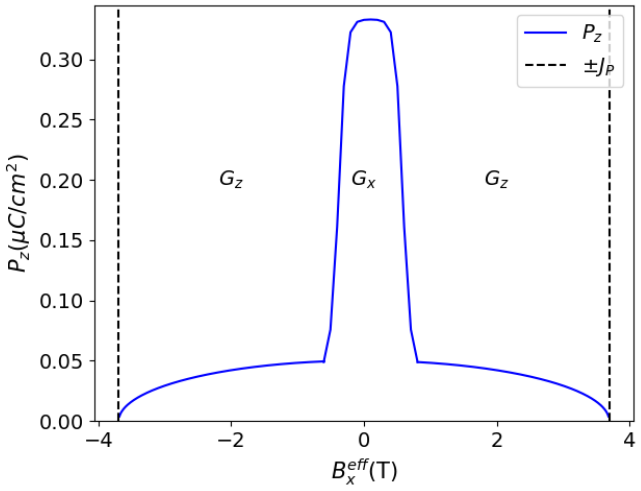

FIGURE 4.8: Change of polarization as a function of applied magnetic field in x direction where we can see the ordering of R site in G_x before phase transition and in G_z with lower polarization.

of the magnetoelectric response of $GdFeO_3$ is coming from the fact that the G-type ordering that breaks the inversion center changes non-linearly with respect to an externally applied magnetic field. When the applied magnetic field is along the z direction, the polarization reduces down to zero at a field of 4 T, i.e., when the Gd spins are all aligned with the magnetic field in an FM state where the exchange striction is absent. When the applied magnetic field is along the x direction, the field is parallel to the main Gd G-type spin direction such that we observe two regimes: (i) from 0 to 1 T, the polarization is not affected by the field, and (ii) at 1 T the Gd spin directions change from x to z direction (but keeping its G-type AFM ordering), which induces a strong reduction of the polarization. From 1 to 4 T the polarization is reduced non-linearly down to 0 when the Gd becomes ferromagnetically aligned with the field along x. These two regimes and the non-linear evolution of the polarization observed for the two directions of the

applied magnetic field in $GdFeO_3$ is in good agreement with the experiments such that we are confident about the validity of the developed model.

Our analysis can be generalized to other rare-earth perovskites in which the polarization arises from the AFM ordering and the exchange striction effect. Our conclusions are also general for all materials where the AFM order breaks the inversion symmetry in the presence of two different magnetic sublattices. For example, Wang *et. al* [159] have reported the ME response of $Fe_2Mo_3O_8$ where the AFM order breaks the inversion symmetry through the exchange striction effect. The ME behavior is similar to what we have for $GdFeO_3$, i.e. giant and non-linear with similar shapes of the polarization versus magnetic field curves. Additionally, for the systems in which it is the FM order that breaks the inversion symmetry, the same analysis can be done but instead of having a non-linear response, we will have a linear response that will be observed.

Chapter 5

Light-driven ultrafast phonomagnetism in $DyFeO_3$

5.1 Introduction

Today's technology largely relies on changing and controlling the properties of materials. Switching ferromagnetic and ferroelectric order in materials, metal to insulator phase transitions, colossal magnetoresistance, just to name a few, are among the properties that are desirable to have control over. One of the focuses of the scientific community is to enhance and improve the control over phases and properties of the materials that will result in technological devices with improved performances. One path in this direction is to achieve shorter time scales in the processes of controlling and changing the phases of the materials to have devices with higher performance speeds [161].

Using laser and matter interaction is one of the approaches employed to achieve a higher speed in dynamics in controlling phases of the materials [161]. Until recently, two mechanisms have been used to experimentally excite the crystal lattice using laser. The first one is the direct coupling of the laser field to the infra-red (IR) active phonons (phonons that possess electric dipole). In the second method, the coupling is indirect and the phonons are excited due to coupling with electrons, like stimulated Raman scattering [162–164]. A third path named ionic Raman scattering (IRS) was proposed 50 years ago but was not possible to prove it experimentally [165–167]. In IRS, an IR active mode excites a Raman active mode and it relies on lattice anharmonicities rather than electron-phonon couplings [168].

Recently, Forst *et. al* [168] showed experimentally that it is possible to excite Raman active phonon modes by exciting IR-active mode with large amplitudes (IRS scattering).

The possibility to induce ultrafast dynamics in a material using nonlinear phononics was observed by Forst [168] but it was not possible to validate this mechanism using an all-optical experiment. Later, the nonlinear modulation of the structure using ultrafast X-ray diffraction is observed directly by Mankowsky in 2016 [169] proving the possibility of exciting Raman modes using excitation of the IR modes. This mechanism needs laser pulses with energies in the mid-IR region while previously used laser pulses to induce dynamics in Raman modes were using laser pulses with energies in the visible or near-IR region.

The IRS can be seen as a new tool for materials discovery, with optical lattice control providing a perturbation analogous to strain, fields, or pressure that can induce exotic collective electronic behavior [170]. Exciting an IR active mode in manganites has shown to melt the spin order [171] or to enhance the coherent transport in cuprite's [172]. In another work, using IRS, it has also been possible to make a transition from stripe-ordered (spin ordered and charge-ordered) non-superconducting phase to superconductive state in cuprite's [173]. Rectification of two IR modes with large amplitudes has shown to excite magnons in $ErFeO_3$ [174]. In 2015, Subdi proposed switching ferroelectric order using IR modes excitation from density functional theory calculations [175] which has been followed by a demonstration of ultra-fast optical reversal of the ferroelectric polarization in $LiNbO_3$ [176]. IRS mechanism is also used to induce transient ferroelectric polarization in $SrTiO_3$ (where the structures is in transition from one stable state to another stable state) [177]. Recently, ultrafast laser has been also successfully used to induce anomalous Hall effect in graphene [178]. Although pioneering experiments demonstrated that driving optical phonons can also affect magnetism [174, 179–181], however, no coherent switching of the spin orientation or coherent light-induced magnetic symmetry breaking has been shown so far.

In this chapter, we present the results of a collaboration with experimentalists doing ultrafast laser excitation of crystals. Our collaborators investigated phonon-induced magnetism (phono-magnetism) in dysprosium orthoferrite ($DyFeO_3$) using IRS. $DyFeO_3$ is a material in which a strong exchange interaction between the transition metal ion and the rare-earth ion leads to a distinctive first-order spin-reorientation phase transition accompanied by a change of the magnetic symmetry from the antiferromagnetic (AFM i.e., Γ_1) to the weakly ferromagnetic order (WFM i.e., Γ_4) [150]. Our collaborators show that a subpicosecond pulse of an intense multiterahertz electric field, tuned in resonance with an IR active phonon mode, drives a coherent spin reorientation, which develops a long-living WFM order within a half-cycle of the spin precession. Phonon-induced magnetism emerges via a non-equilibrium metastable state, inaccessible not only via a thermodynamic transformation but also via optical pumping of the high-energy electronic transitions. We have demonstrated experimentally and theoretically

that phono-magnetism originates from phonon-induced lattice distortions and it leads to ultrafast modification of the Dy-Fe exchange interaction. To study and investigate the processes involved in the excitation of $DyFeO_3$ we used DFT calculations (for the technical detail see Appendix B.3).

5.2 Ground state calculation

One of the drawbacks of the DFT is its self-interaction error (see Sec. 1.2.4). To solve this problem an energy penalty is added to reinforce localization. A Hubbard-like interaction "U" is added in the interaction between localized orbitals of the same kind and this makes the electron occupying these orbitals to be more localized [35]. Adding this into DFT forces the electrons from the partial occupation of the orbitals to go toward integer occupations. However, this method enable multiple minima of energy associated to different orbital occupations such that the electronic states obtained at the end of the SCF cycle might be in one of these local minima that is not the ground state of the system [182]. Different methods have been implemented to tackle this problem, including occupation matrix control [183, 184], quasi adiabatic [185], U ramping [182], meta-heuristic approaches [186].

Since we are studying $DyFeO_3$, where Dy atoms have f electrons, for which we need to add Hubbard interaction, we might end up in an electronic state other than the real ground state. In this work, we have used the occupation matrix control to achieve the true GS of the system [184]. In this method, different possible occupations of the density of localized orbitals are tested to find the GS of the system (for details of the calculation see Appendix C) where we have relaxed the structure by using different occupation matrices. For Fe, Since we have half filled orbitals (all orbitals for one spin channel are filled) and since the exchange splitting is large, we are sure that we will reach to ground electronic state even if we use U in the calculations.

We found that the ground state of the Dy-f orbitals occupation is also the one that gives the best agreement with the experimental cell parameters, which confirms our choice of the U parameter (see Tab. 5.1). All the results given below are those obtained for this GS occupation of the f orbitals in $DyFeO_3$, which we verified to be the case for all the further different calculations (relaxation, frozen phonon, and condensed phonons).

In Tab. 5.1 we present the calculated lattice parameters and band gaps from our simulations. The calculated results for the case where f electrons are in the valence are in good agreement with the results from the experiments. If we do a calculation where the f electrons are frozen in the core, the lattice parameters deviate from the experimental

TABLE 5.1: Lattice parameters and band gaps from our calculations compared to values from experimental values.

	a	b	c	Band-gap(eV)
Exp [187]	5.302	5.598	7.623	2.1 [188]
DFT($f_{valence}$)	5.292	5.594	7.615	2.30
DFT(f_{core})	5.247	5.588	7.588	2.28

values. So, in the calculations where we put the f electrons in the core, we have fixed the lattice parameters coming from the case where the f electrons are put in the valence.

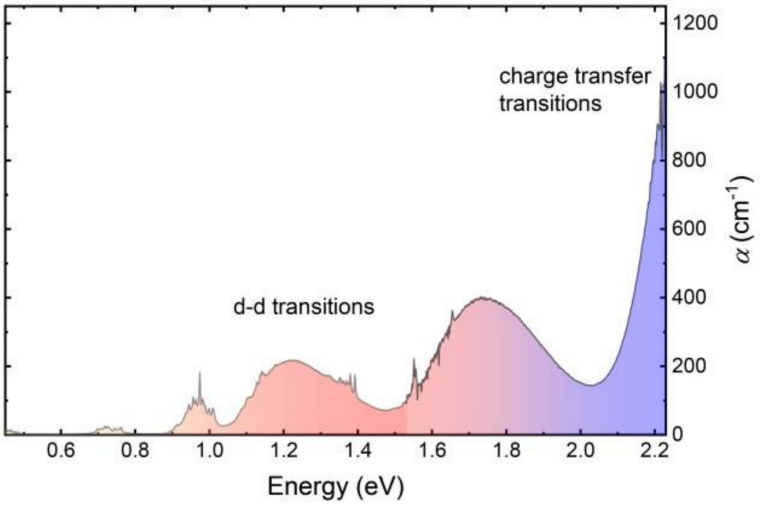

FIGURE 5.1: Optical absorption of the sample from the experiment. The absorption in higher energies than 2.1 eV are due to O^{2p} to Fe^{3d} electronic transition. While lower than 2.1 eV absorption are coming from d-d spin-forbidden transitions.

The optical absorption of the sample from experiments is shown in Fig. 5.1. In energies higher than 2.1 eV, the absorption is coming from a charge transfer from O^{2p} to Fe^{3d} in agreement with the calculated band gaps from DFT [188]. Lower energy transitions are due to spin forbidden $d-d$ transition in Fe^{3+} multiplets.

In the experiment, ultrafast laser pulse is tuned to be in the frequency range of the phonon modes, which accordingly will excite the phonon modes of the structure. In the following part, we calculate the phonon modes of the structure to study which one of the modes will be affected by the range of the laser pulse frequencies that hit the sample during the experimental ultrafast laser excitation.

5.3 Phonons

In Tab. 5.2 we report our calculated Raman and IR active mode frequencies for both Dy-f electrons treated as valence states ($f_{valence}$) and as core states (f_{core}) (only B_{2u},

B_{3u} and A_g modes are shown for a complete list of phonons see Appenedix D). The main difference between these two calculations is that with $f_{valence}$ Dy is magnetic while with f_{core} Dy atoms do not possess magnetic moment. The Raman active modes are in good agreement with respect to the experiments and previous DFT calculations (done with f_{core}) [187]. The few deviations between our results and the previous calculations can be due to the fact that they have used different lattice parameters compared to us (experimental cell in previous calculations vs relaxed PBEsol+U cell parameters in our case) and also different PAW atomic potentials.

We note that in the f_{core} case, the space group of the crystal is $Pbnm$. In the $f_{valence}$ case, we obtain that the G-type AFM magnetic ordering of Dy has the lowest energy (with respect to the A- and C-type AFM or the ferromagnetic state), in agreement with the experimental reports. This G-type AFM of Dy atoms combined with the G-type AFM ordering of the Fe breaks the inversion center such that the space group of the crystal becomes $Pna2_1$ (see Tab .2.2).

The main idea behind doing calculations with f electrons in the core and in the valence is to estimate the effects of f electrons and magnetism on phonons frequencies. The difference between the f_{core} and $f_{valence}$ could thus be accounted to the effect of the magnetic order of the Dy, though the differences are rather small for most of the modes (the largest difference is about 12cm^{-1}). We will use f_{core} calculations to estimate the couplings of phonons and we then use $f_{valence}$ when we want to calculate the change in magnetic interactions as a funciton of phonons.

TABLE 5.2: Calculated $DyFeO_3$ Raman active and IR active mode frequency (cm^{-1}). In the first column, we show the mode label within the $Pbnm$ structure and in the second column, we report the frequency of the mode with f electron in the core. The third column presents the mode labels in the $Pna2_1$ space group and the last column is the frequency of the mode in $Pna2_1$ structure by considering the f electrons in the valence with the G-type AFM ordering of the Dy. The last column gives the change in frequency between the two cases. In the fifth column we also report the calculated frequencies and in the sixth column the experimental measurements reported by Weber *et al.* in Ref. [187].

label($Pbnm$)	$f_{\text{in-core}}$	label($Pna2_1$)	f_{valence}	ref	exp	$\Delta(f_{\text{core}} - f_{\text{valence}})$
$A_g(1)$	109	$A_1(1)$	107	112	113	2
$A_g(2)$	129	$A_1(2)$	133	135	140	-4
$A_g(3)$	255	$A_1(3)$	249	262	261	6
$A_g(4)$	330	$A_1(4)$	328	332	341	2
$A_g(5)$	401	$A_1(5)$	408	422	422	-6
$A_g(6)$	415	$A_1(6)$	408	415	417	7
$A_g(7)$	401	$A_1(7)$	413	422	422	-11
$A_g(8)$	479	$A_1(8)$	480	490	496	-1
$B_{1u}(1)$	109	$B_2(6)$	106	–	–	2
$B_{1u}(2)$	168	$B_2(7)$	175	–	–	-7
$B_{1u}(3)$	244	$B_2(8)$	250	–	–	-6
$B_{1u}(4)$	274	$B_2(9)$	278	–	–	-3
$B_{1u}(5)$	324	$B_2(10)$	322	–	–	2
$B_{1u}(6)$	346	$B_2(11)$	347	–	–	-1
$B_{1u}(7)$	399	$B_2(12)$	393	–	–	6
$B_{1u}(8)$	501	$B_2(13)$	497	–	–	4
$B_{1u}(9)$	541	$B_2(14)$	543	–	–	-2
$B_{3u}(1)$	97	$B_1(6)$	100	–	–	-2
$B_{3u}(2)$	189	$B_1(7)$	187	–	–	2
$B_{3u}(3)$	228	$B_1(8)$	234	–	–	-6
$B_{3u}(4)$	289	$B_1(9)$	290	–	–	-0
$B_{3u}(5)$	307	$B_1(10)$	309	–	–	-1
$B_{3u}(6)$	333	$B_1(11)$	332	–	–	1
$B_{3u}(7)$	425	$B_1(12)$	424	–	–	1
$B_{3u}(8)$	510	$B_1(13)$	514	–	–	-4
$B_{3u}(9)$	523	$B_1(14)$	525	–	–	-2

5.4 Laser phonon interaction

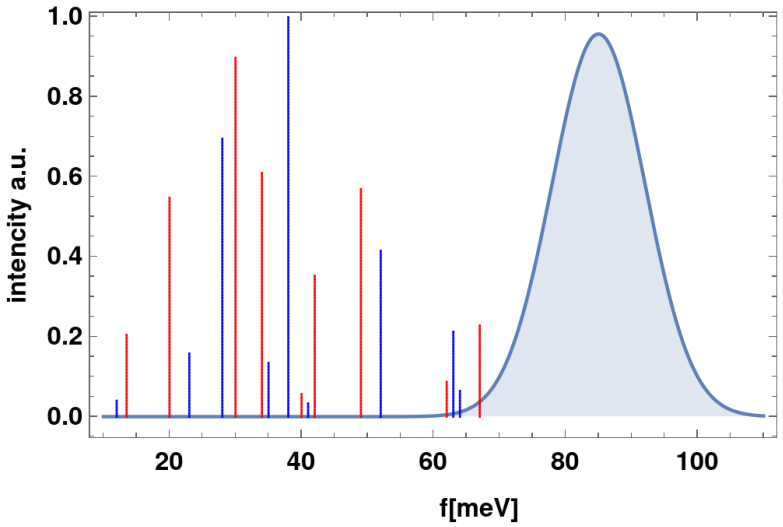

FIGURE 5.2: Schematic presentation of the laser pulse and B_{1u} (red lines) and B_{3u} (Blue lines) modes frequency positions. The length of the lines modes is representing mode effective charge normalized with effective charge of the mode with highest effective charge.

To understand to which phonon modes the laser pulse couples, we plotted the laser pulse and polar modes in Fig. 5.2. Here, we are considering the laser field to be a Gaussian function with formula Eq. 5.1. In this function σ_ω gives the spread in frequency and E_0 gives the peak of the laser pulse.

$$E(\omega) = \frac{E_0}{2\pi\sigma_\omega} e^{\frac{-(\omega-\omega_0)^2}{2\sigma_\omega}} \tag{5.1}$$

The modes presented in Fig .5.2 are B_{1u} and B_{3u}. These two modes are those that are polar in the a and b directions respectively, the direction in which the laser is polarized in the experiments. The laser in this case couples to B_{1u} and B_{3u} with the highest frequencies. The schematic representation of polar distortion of the $B_{1u}(9)$ and $B_{3u}(9)$ are shown in Fig 5.3. The $B_{1u}(9)$ mode is polar in b direction and $B_{3u}(9)$ is polar in a direction of the *Pbnm* structure. This polarization is mainly coming from oxygen displacements and other atoms are not moving in these modes.

In the experiment, the optical absorption of the sample below 150 meV was measured and the result is shown in Fig. 5.4. From this figure the absorption close to highest frequency phonon modes (i.e., B_{1u} and B_{3u} modes) is the highest and the result is in agreement with the DFT calculations.

The highest frequency $B_{1u}(9)$ (Fig. 5.3-A) mode is the closest to the laser pulse peak frequency and it also has a large effective charge compared to other modes in this region.

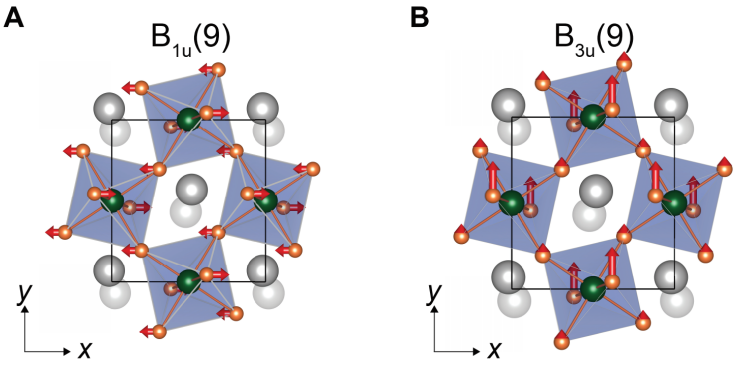

FIGURE 5.3: Schematic picture of a) $B_1u(9)$ and $B_3u(9)$ modes

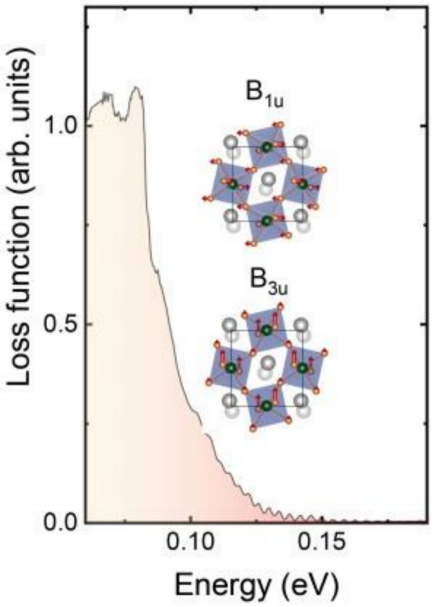

FIGURE 5.4: Optical absorption of the sample below 150 meV energy of the laser from the experiment. The absorption is maximum close to 0.6 eV (i.e., ∼500 cm^{-1}) coming mainly from B_{1u} and B_{3u} modes.

This mode's eigenvector corresponds to oxygen bond stretching as shown in figure 5.3-A. Considering all these facts, we can conclude that the laser will excite the $B_{1u}(9)$ more strongly. The point to notice here is the fact that deriving this IR mode does not create a magnetic phase transition, since this vibration does not change the potential energy surface and magnetic interactions in macroscopic time scales.

5.5 Phonon-phonon interaction

To understand what is causing the spin reorientation in the sample exposed to the laser pulse, we studied the coupling of IR mode to other modes that could consequently change the magnetic interactions of Dy and Fe and result in spin reorientation [168] as

TABLE 5.3: Coupling coefficients for B_{1u} and $A_g(1)$ and $A_g(2)$ modes. The units are $(meV/(\sqrt{amu}\mathring{A})^n)$ with square root of atomic mass unit (amu) times angstrom $(\sqrt{amu}\mathring{A})$

	C_R	d_{IR}	d_R	γ_1
$A_g(1)$	-0.004	0.0072	0.000	0.0681
$A_g(2)$	0.003	0.0072	0.000	0.1246

suggested by IRS mechanism. To determine the phonon-phonon couplings, we used the potential energy as expanded according to Eq 5.2. We fitted this equation against DFT calculations to get the coupling constants in the spirit of Juraschek et.al [156]. We did the fitting with $f_{valence}$ and f_{core} and since the differences were negligible, all the fitting is done with f_{core} PAWs for Dy.

$$\begin{aligned} V(Q) = \omega_{IR}^2 Q_{IR}^2 + \omega_R^2 Q_R^2 + C_R Q_R^3 + \gamma_1 Q_R Q_{IR}^2 \\ + \frac{1}{4} d_{IR} Q_{IR}^4 + \frac{1}{4} d_R Q_R^4 \end{aligned} \tag{5.2}$$

In this equation, Q_X are mode amplitudes of phonon mode X (X = IR or R) with eigenfrequencies ω_X. The coefficients C_R, γ_1, d_{IR} and d_R are the ones fitted on DFT data. In this case, we have considered the highest IR frequency $B_{1u}(9)$ mode (noted IR in Eq 5.2) excited by the laser and its couplings to any A_g modes (noted R in Eq 5.2) that are the first order couplings coming into play in the 20 atoms perovskite *Pbnm* phase (the A_g mode label being invariant under all the symmetry operation of the crystal, any coupling order with this mode is allowed). We found that the strongest coupling is obtained by the second-lowest frequency $A_g(2)$ (Fig. 5.5 (c)) mode, followed by the first one $A_g(1)$ (Fig. 5.5 (b)), such that we consider these two modes in our model. This also shows that considering the lowest A_g mode frequency by default is not necessarily physically relevant. The calculated model parameters for these $A_g(1)$ and $A_g(2)$ modes are presented in Tab. 5.3.

As one can see, the γ_1 parameter drives the strongest coupling with the B_{1u} mode. This coefficient couples A_g modes with the square of the B_u modes. This means that the B_u mode forces the A_g mode in the same direction irrespective of the direction of the B_u mode distortion. This interaction then shifts the Ag mode to one direction. The effect of this interaction is shown in Fig. 5.6. Fig. 5.6 shows that the minimum of the energy surface for A_g mode shifts to a different position for higher amplitude oscillations of the B_u mode which means the A_g mode will be quasi statically condensed in the structure.

In the experiments, a SHG signal around 100 cm^{-1} (3 THz) is observed after the laser excitation. This symmetry breaking could be due to the excitation of a low-frequency

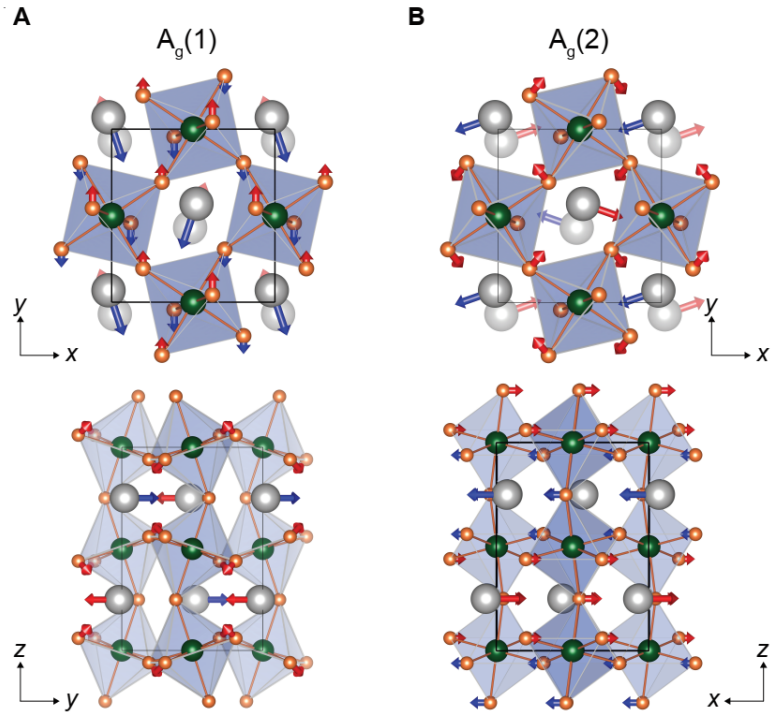

FIGURE 5.5: Schematic picture of $A_g(1)$ mode, c) $A_g(2)$ mode

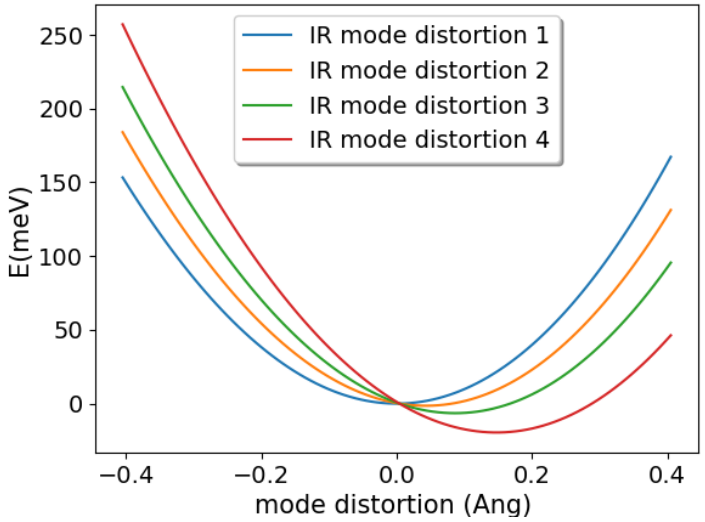

FIGURE 5.6: Schematic representation of the potential energy change for A_g mode as a function of different amplitudes of IR mode as we go from lower amplitudes (IR mode distortion 1) to higher amplitude (IR mode distortion 4) of distortions of the B_{1u} mode mode

polar mode. We then also considered the coupling of the highest B_{1u} mode with the lowest B_{1u} mode as a possible phenomenon to explain the observed SHG signal at 100 cm^{-1}. To consider this possibility, we fitted Eq. 5.3 against DFT calculations:

TABLE 5.4: Coupling coefficients for $B_1u(9)$ and $B_1u(1)$ modes. The units are $(meV/(\sqrt{amu}\mathring{A})^n)$ with square root of atomic mass unit (amu) times angstrom $(\sqrt{amu}\mathring{A})$

	d_IR1	d_IR2	γ_1	γ_2	γ_3	γ_3
$B_1u(9)$-$B_1u(1)$	0.0072	0.0000	-0.0046	0.0010	0.0002	0.0045

$$\begin{aligned} V(Q) =& \omega_1^2 Q_{IR1}^2 + \omega_2^2 Q_{IR2}^2 + \frac{1}{4} d_{IR1} Q_{IR1}^4 \\ &+ \frac{1}{4} d_{IR2} Q_{IR2}^4 + \gamma_1 Q_{IR1} Q_{IR2} + \gamma_2 Q_{IR1}^2 Q_{IR2}^2 \\ &+ \gamma_3 Q_{IR1} Q_{IR2}^3 + \gamma_4 Q_{IR1}^3 Q_{IR2} \end{aligned} \tag{5.3}$$

The calculated coefficients are presented in Tab. 5.4. For this mode, the coupling coefficients are one to two orders of magnitude smaller than the A_g mode coupling to B_{1u}.

In this section, we have shown which modes are coupled to the laser pulses. In the following section, we will consider the dynamics of the modes due to laser excitation.

5.6 Phonon dynamics

Since the amplitude of the coupled phonon condensation is related to the inverse of its squared frequency, from the coupling coefficient it is not possible to say which coupling is important [156]. To clarify this point, we simulated phonon dynamics to understand how large the distortion for each of the A_g modes could be through their coupling with the B_{1u} mode. The phonon dynamics associated with our phonon potential is studied through the following equation of motion (Eq. 5.4):

$$\ddot{Q} + \gamma \dot{Q} + \bigtriangledown_Q [V(Q) - F(t,Q) Q_{IR}] = 0 \tag{5.4}$$

Where Q=$Q_{B_{1u}}$, Q_{A_g} are the line width of each mode and F(t,Q) is the laser force induced on the $B_1u(9)$ mode. The results of the phonon dynamic are shown in Fig. 5.7 (for modes $A_g(1)$ and $A_g(2)$) and Fig. 5.8 (for mode $B_{1u}(1)$) where we plot the amplitude evolution of each mode eigendisplacement with respect to time.

As confirmed from the fitted parameter coupling strength, we observe that the $A_g(1)$ and $A_g(2)$ have similar excitation amplitudes while it is much smaller for the $B_{1u}(1)$ mode (note the range change). According to these calculations, the dynamics are strongly

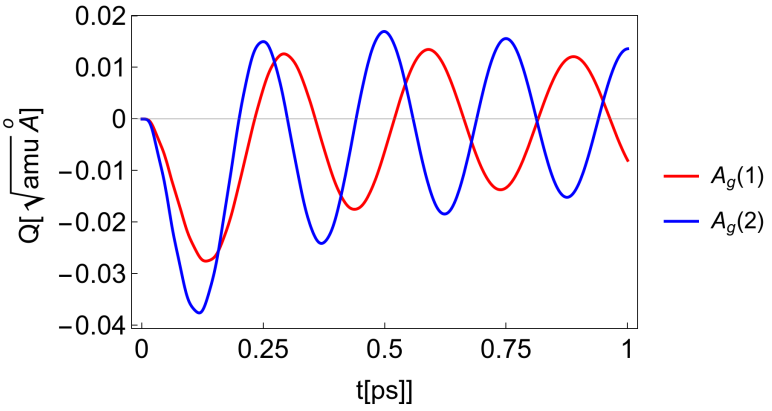

FIGURE 5.7: Dynamics of amplitude of $A_g(1)$ and $A_g(2)$ phonons as driven by $B_{1u}(9)$ mode. The x-axis represent time in pico-seconds and y-axis shows the mode amplitude in units of square root of atomic mass unit (amu) times angstrom ($\sqrt{amu}\mathring{A}$).

dominated by the A_g modes excitations, the B_{1u}-B_{1u} mode coupling cannot be the source of the SHG signal.

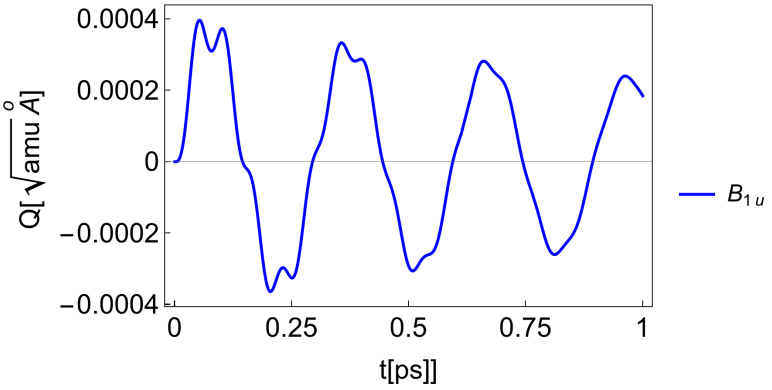

FIGURE 5.8: Dynamics of amplitude of $B_{1u}(1)$ phonons as driven by $B_{1u}(9)$ mode. The x-axis represent time in pico-seconds and y-axis shows the mode amplitude in units of square root of atomic mass unit (amu) times angstrom ($\sqrt{amu}\mathring{A}$).

From Fig. 5.7 we can see that the Ag modes are oscillating around different minima than their ground state. This shift in minimum has a longer lifetime than the laser pulse duration and also a lifetime of the B_{1u} mode. This quasi-static shift in minima could change the interactions and material properties in picosecond time scales.

To understand the change in magnetic interaction resulting from the dynamics of the $A_g(1)$ and $A_g(2)$ modes, we will study in the following how the magnetic interactions are modified as a result of these modes rectification.

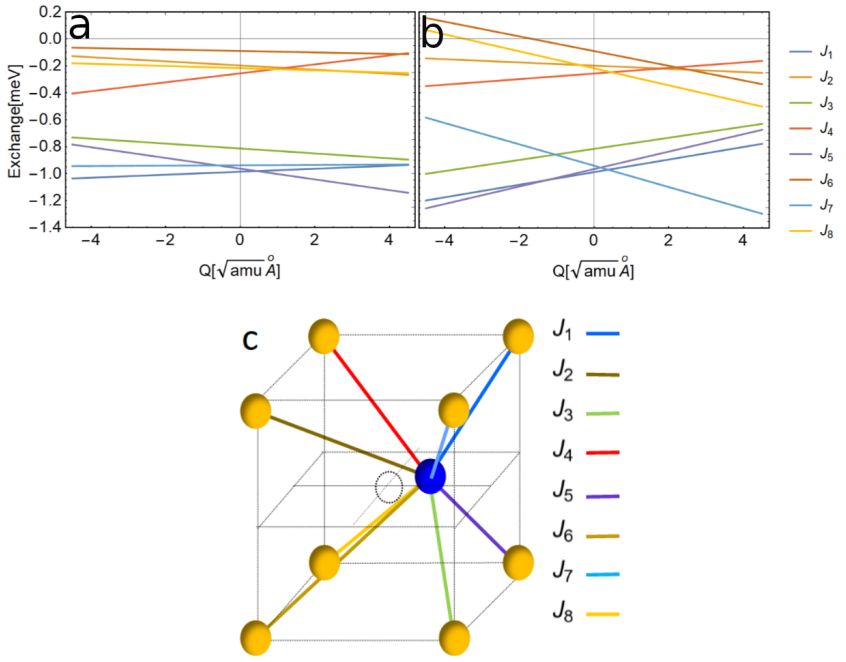

FIGURE 5.9: Superexchange interactions between Dy and Fe as a function of a) $A_g(1)$ mode amplitude and b) $A_g(2)$ mode (color scheme corresponds to the Dy-Fe bond color of panel c). The x-axis represents the mode amplitude in square root of atomic mass unit times angstrom ($\sqrt{amu}\mathring{A}$) and y axis shows exchange interaction in meV. The panel c) shows to which Dy-Fe neighbor each J corresponds to. Blue ball corresponds to Dy and yellow balls correspond to Fe; The empty black circle corresponds to the Dy atom as if not displaced from the high-symmetry cubic position.

5.7 Phonon-magnetism interaction

To study how the indirectly driven A_g modes can change the magnetic interaction between Dy and Fe, we used the Greens function method to calculate the superexchange interaction as a function of A_g modes amplitude following the scheme of Korotin *et al.* [50] as implemented in the TB2J code [51].

We report in Fig 5.9 the evolution of the Dy-Fe superexchanges with respect to both $A_g(1)$ and $A_g(2)$ mode amplitudes. As we can see the two modes can drive different modifications of superexchanges, which can be decomposed into eight contributions related to the eight Fe ions surrounding one Dy ion as shown in Fig. 5.9(c). For example, J3 and J7 have opposite trends with respect to both $A_g(1)$ and $A_g(2)$ mode condensation, while all the other J have the same trend. We also note that the $A_g(2)$ mode has a larger effect on the J than the $A_g(1)$ mode.

To have a more qualitative understanding of the way the A_g modes modify the exchange interactions, we have shown in tables the change in the exchange interactions between iron and iron (see Tab. 5.6) and between Iron and Dysprosium (see Tab. 5.5). As can be seen from the tables, the iron Dysprosium interaction has changed with a higher slope,

TABLE 5.5: The table represents the slope of a line fitted to the exchange interactions change between Fe and Dy as a function of A_g modes distortions according to the Fig. 5.9 a and b. The units are $meV/\sqrt{amu}\mathring{A}$

Exchange	dj/(jdQ) [$A_g(1)$]	dj/(jdQ) [$A_g(2)$]
J1	-0.011	-0.047
J2	0.077	0.060
J3	0.022	-0.050
J4	-0.129	-0.081
J5	0.041	-0.067
J6	0.059	0.607
J7	-0.001	0.084
J8	0.037	0.289

TABLE 5.6: The table presents the slope of a line fitted to the exchange interactions change between Fe atoms as a function of A_g modes distortions amplitude. The units are $meV/\sqrt{amu}\mathring{A}$

Exchange	dj/(jdQ) [$A_g(1)$]	dj/(jdQ)[$A_g(2)$]
Fe-Fe	0.001	0.001

and changes in exchange interactions for iron and iron are negligible and could not be responsible for spin reorientation.

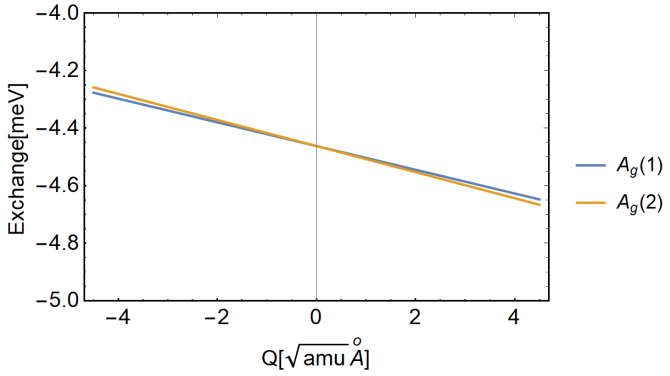

FIGURE 5.10: Average exchange interactions change for two A_g modes as a function of A_g modes distortion amplitudes. The x-axis shows the A_g modes amplitudes in units of $\sqrt{amu}\mathring{A}$ and The y-axis represents the sum of the exchange interactions between Fe and Dy in meV.

To have a more clear picture of the way the Ag mode modifies the exchange interactions, in figure 5.10 we present the average exchange interaction change between each Dy and its 8 Fe neighbors. The figure shows that both $A_g(1)$ and $A_g(2)$ change the exchange interaction with the same sign and they both will change the interactions between Fe and Dy so that the magnetic phase transition happens.

To conclude the theoretical part of the work, we have shown that laser pulse couples to highest frequency IR active phonon modes and excite these modes with large amplitudes. The excited high frequency IR active modes will couple to two lowest frequency Ag

Raman active modes and shift their minimum to a new position and freezing these modes quasi statically in the structure. This rectification of the Raman active modes will change the exchange interactions between Dy and Fe and causes a phase transition. In the following section we will present experimental results concerning the laser excitation of the $DyFeO_3$. From these results we will see that other possible mechanism (e.g., thermal dissipation) will be ruled out and the one suggested by the theory is the mechanism that is responsible in the phase transition.

5.8 Nature of spin reorientation

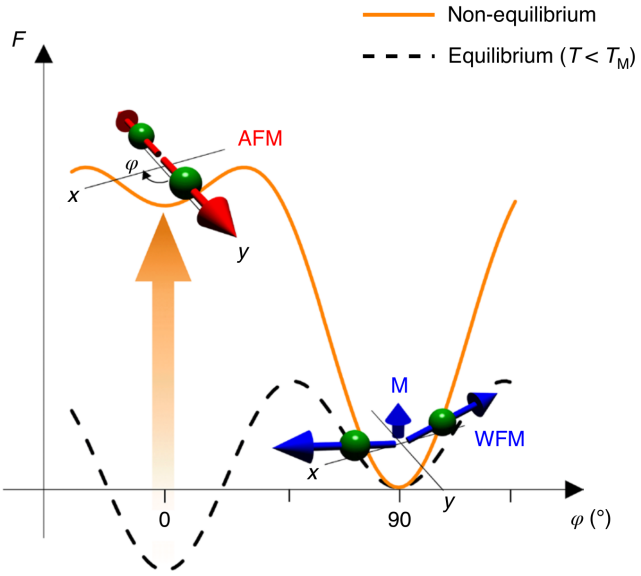

FIGURE 5.11: The magnetic potential F as a function of the angle φ that the spins form with the y axis before (dashed black line) and after (orange line) phonon excitation. The potential is shown only for T < T_M . The red and blue arrows depict the spin configurations that correspond to the antiferromagnetic (AFM) and weakly ferromagnetic(WFM) phases. The orange arrow highlights the destabilization of the AFM ground state together with the reduction of the potential barrier that separates the phases

The spin reorientation in $DyFeO_3$ can be described by the magnetic potential F, which depends on the temperature and the angle φ the spins form with the y-axis (see Sec. 2.3.3 and Eq. 2.6). In a broad temperature range, this potential function features two characteristic minima at 0 and 90 degrees (Fig. 5.11), which signals two ordered states. The height of the potential barrier that separates the two competing states, as well as their relative energy, is controlled by the strength of the Fe–Dy interactions. This interaction is not only sensitive to the temperature but also changes in the crystal environment, both via direct modulation of the Fe–Dy electronic overlap and via structurally driven

changes in the orbital state of the Dy $4f$ multiplet [189]. In according to DFT calculations, we considered light-induced oscillations of atoms driven far from their equilibrium positions to control the strength of the Fe–Dy exchange [190, 191] and to realize lattice control of the spin arrangement on an ultrafast timescale.

A comparison of the Fourier spectra [see Fig. 5.12-(a) and (b)] reveals that the frequency of the spin precession excited by pulses in resonance with the lattice mode is shifted as compared to the equilibrium value. The sign of the shift Δf depends on the initial magnetic configuration, being red in the AFM phase and blue in the WFM phase. To underline the resonant character of the frequency shift, we tuned the photon energy of the pump pulse across the phonon resonance and extracted the central frequency of the spin oscillations [see Fig. 5.12-(c)]. The data acquired in both magnetic phases show that the onset of the frequency shift follows closely the spectrum of the linear absorption of the B_u phonon mode and therefore reveals a correlation between the light-driven phonon and spin dynamics. These observations contain important information on the effects of phonon pumping on magnetic potential. The redshift indicates a flattening of the potential energy in the vicinity of the AFM minimum ($\varphi = 0$), which may lead to phase instability. The blue shift observed in the WFM phase points at an increased curvature of the potential and enhanced phase stability in the vicinity of the WFM minimum ($\varphi = 90$).

In Fig. 5.13, we have shown the dynamics of the magnetism as driven by a laser pulse with 85 meV pulse in blue. The magnetism with this energy arises immediately in less than 5 ps. It is important to compare the observed kinetics of the ultrafast Morin phase transition launched via the phonon-pumping with those driven via a dissipative mechanism. Therefore, we performed an auxiliary experiment in which the sample was excited with visible light having photon energy of 2.3 eV and 3.1 eV, above the change-transfer electronic gap, the onset of this absorption band is visible in the right part of figure 5.1. Here the optical absorption is large ($\alpha \gg$1000 cm^{-1}), and the transition is expected to be driven by the heat deposited in the medium. As was shown in Fig. 5.13 (green line), the experiment shows that although the spin oscillations are launched nearly instantaneously for high photon energy excitation with pump fluences similar to those for the phonon-pumping, it takes more than 30 ps before a photo-induced magnetization ΔM starts to appear and about 100 ps to complete the growth. This indicates that the heat-driven evolution of the potential is significantly slower than the one guided by coherent pumping of the lattice. Note that the optical absorption at the above-bandgap energy of 2.3 eV and especially 3.1 eV is significantly larger than the optical absorption due to phonons at 85 meV. The slow dynamics can be explained by the slow heat transfer from the excited electrons to the $4f$ electrons of Dy^{3+}, which determines the dynamics of the magnetic potential. This kinetics stands in sharp contrast with the one studied

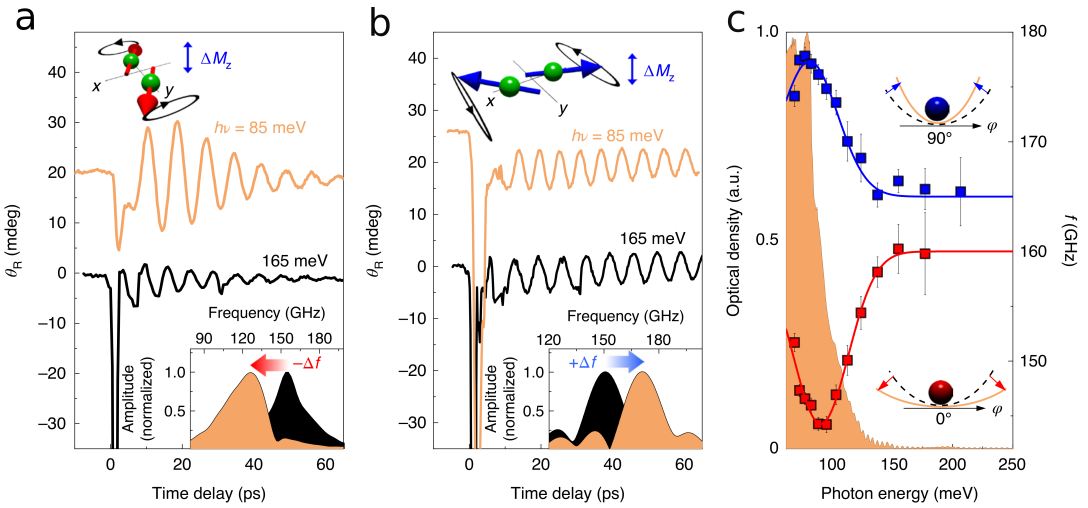

FIGURE 5.12: (Results from experiment) a, b, time-resolved transient rotation of the probe polarization plane θ_R after light excitation with photon energies of 85 meV (orange traces) and 165 meV (black traces) performed in the AFM (a) and WFM (b) phases. Bottom insets: normalized amplitude spectra of the soft mode oscillations. Top insets: schematics of the corresponding spin precessions, with the resulting oscillating magnetic component ΔM_z. c, Central frequency of the exciting soft mode as a function of the photon energy of the pump pulse in the two magnetic phases. The solid lines serve as a guide to the eye. The shaded curve shows the sample's optical density. Insets: schematics that indicate changes in the local curvature of the magnetic potential. a.u., arbitrary units. The error bars represent the standard error of the extracted frequency f.

here by the phonon pumping where the potential is altered on a timescale shorter than a single cycle of the coherent spin precession. All this leads us to conclude that a very different mechanism from regular heating is at play in the case of phonon pumping. We also note that the frequency difference between the excited phonon (17 THz) and the magnon (0.2 THz) rules out direct phonon–magnon coupling.

As shown in Fig. 5.14, measurements of the frequency of the magnetic mode at equilibrium as a function of temperature revealed a cusp-like evolution in proximity to T_M, in excellent agreement with Balbashov et al. [192]. In contrast, the frequency of the magnons launched via resonant phonon excitation was characterized by a split-up of the magnon branches at T_M, which led to a pronounced discontinuity of more than 50 GHz (Fig. 5.14). The discontinuity leads to the emergence of magnetic responses at frequencies well below the minimum value attainable at equilibrium (140 GHz). Although the heat capacity of $DyFeO_3$ changes by a factor of 20 between 10 and 60 K (ref. [193]), the magnitude of the observed frequency change is nearly temperature independent in the range 10–100 K, which provides another indication that a non-thermal process is at play.

Importantly, phonon pumping substantially increases the energy of the AFM state, which simultaneously lowers the potential barrier, such that close to T_M the AFM phase may

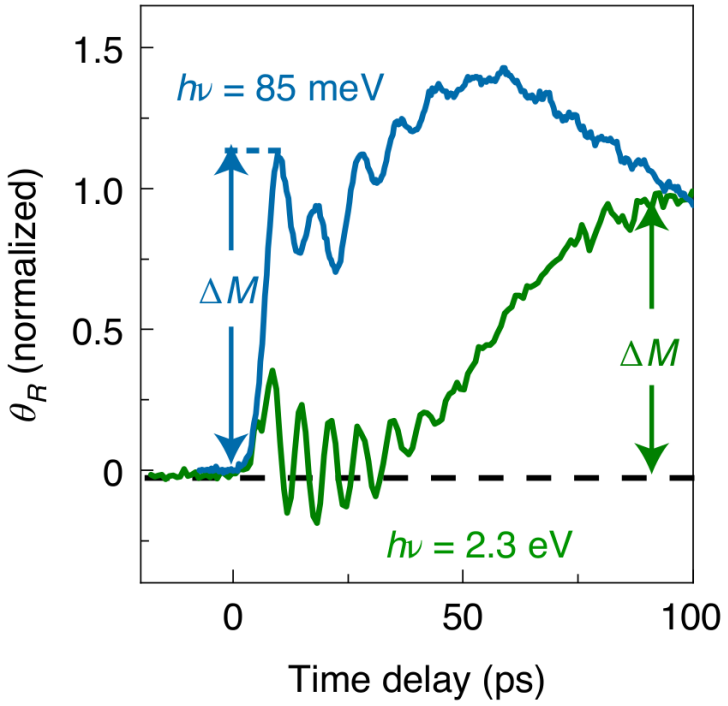

FIGURE 5.13: (Results from experiment) a direct comparison of the dynamics of the magnetization initiated by a pump pulse with above-bandgap photon energy (2.3 eV) and in resonance with the phonon mode (85 meV)

lose its thermodynamic stability.

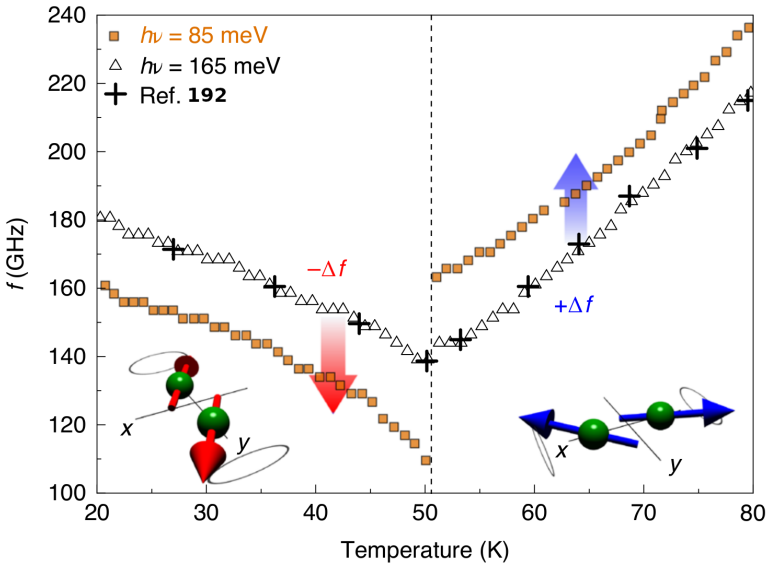

FIGURE 5.14: (Results from experiment) Frequency of the spin precession as a function of the temperature across the Morin phase transition for different photon energies of the pump excitation

From these considerations, we can see that other possible mechanisms, for the phase transition studied here, can not explain the observed magnetic dynamics. Hence, in

accordance with the results of DFT, we can consider the IRS as the mechanism inducing the phase transition.

The results of this section are adapted from ref [154], For a complete discussion see the corresponding reference.

5.9 Conclusion

In this chapter, we have shown a mechanism to manipulate magnetic phase using nonlinear phononics in $DyFeO_3$. The experimental results show that excitation of the $DyFeO_3$ using a laser tuned to IR mode frequency induces dynamics that are faster than the ones resulting from heat dissipation phase transition. Our results (in accordance with experiment) prove that the excitation of the $DyFeO_3$ using a laser tuned to IR active phonon modes, can cause a rectification of the low-frequency Rama active modes. This quasi-statically frozen Raman mode in the structure can change the exchange interactions between Dy and Fe, which induces a magnetic phase transition. The same mechanism can be present in other magnetic materials of rare-earth based compounds with anisotropic magnetic interactions (i.e., manganites, nickelates and orthochromites). The discussed mechanism is an effective approach to manipulating magnetic interactions and magnetic phases in the materials. This mechanism is much faster than the other mechanism (i.e., heat dissipation phase transition) and can offer devices that have much faster operation times.

The results presented in this chapter show the power of nonlinear phononics as an efficient method to manipulate and control properties of materials in fashion that is not achievable through other physical mechanisms. Advances in this filed, and achieving more powerful laser sources, may allow controlling and achieving new classes of materials. Nonlinear phononics has recently shown to propagate in macroscopic length scales thanks to phonon-polariton which makes this scheme more important.

Chapter 6

Concluding remarks

In this thesis, we have studied the magnetic and magnetoelectric properties of rare-earth orthoferrites (RFeO$_3$). Since the thesis is mainly concerned with magnetic properties, in Chapter 1, we have discussed the origin of magnetism and the theories to explain it. We have discussed the different mechanisms of interactions between magnetic moments in materials and finally we have derived an extended Heisenberg model Hamiltonian that we used to study RFeO$_3$. To make our model we have used DFT calculations such that in the second part of Chapter 1, we have discussed the DFT, its theory, and the approximations used to practically solve the equations. We have finished this first chapter by describing the methods to fit and extract parameters that we used in our Heisenberg models.

In Chapter 2, we have discussed the material properties of RFeO$_3$ crystals. We have introduced their magnetic structures and their different magnetic phases. We have also discussed some of the magnetic properties arising due to the inclusion of two magnetic sublattices in the structure. In particular, we discuss the main open questions about the magnetic properties of these materials, i.e. magnetization reversal and spin reorientation.

The Chapter 3 was devoted to study and understand the magnetic properties and behaviors present in RFeO$_3$. We have derived the Heisenberg Hamiltonian for RFeO$_3$ analytically and we fitted it against DFT calculations. Using our model, we have explained the origin of the different magnetic behaviors in these materials. In particular, we have shown that the DMI interaction between rare-earth and transition-metal cations can create the spin rotation transition in these materials. We have also shown that the origin of magnetization reversal in RFeO$_3$ is DMI interaction between rare-earth and iron. Besides, we have presented how DMI can polarize the rare-earth element in different directions depending on the atoms in A site or B site.

In chapter 4 we have used our model developed in Chapter 3 to study the magnetoelectric (ME) responses of $R\mathrm{FeO_3}$. The main focus of this chapter is the nonlinear ME responses observed experimentally in $\mathrm{GdFeO_3}$. Our model correctly reproduces the results of the experimental observations and it allows us to study the origin of the nonlinear and large ME responses observed in $\mathrm{GdFeO_3}$. We have shown that the origin of the nonlinear ME response is related to the fact that the G-type order, that breaks inversion symmetry, changes nonlinearly with respect to an applied magnetic field, hence creating a nonlinear ME response.

In chapter 5 we have presented the results of our collaboration with the experimental group of A. Caviglia regarding the manipulation of the magnetic phase of $\mathrm{DyFeO_3}$ under an ultrafast laser excitation. In this work, we presented a mechanism that can be utilized to induce magnetic phase transitions in very short time scales. We have proved that nonlinear phononics is the mechanism that drives the magnetic phase transition. We have also shown that the dynamics of the magnetic phase transition arising from nonlinear phononics are much faster than the dynamics originating from heat dissipation.

Rare-earth perovskite oxides, a big family with different properties and functionalities can play an important role in technology. Current researches on this family show that they are multiferroic materials where we can achieve large magneto-electric responses. This property paves the way for utilizing electric field to control magnetism (a crucial part in efficient spintronics). Our work sheds light on the magnetic interactions and magnetic properties of these materials, their understanding being very important in advancing the technology that might emerge from these materials either as a magnetic material or as a type-II magneto-electric.

Although we have addressed some of the questions regarding the magnetic properties of these materials, there are still some other aspects that can be studied. Our findings regarding the magnetic interactions present in these materials shows that B site atoms polarize the A site atoms at higher temperatures than their Néel temperature. On the other hand, the direction of these interactions depends on the A site atom and its orbital magnetic moments. Hence, if we have a checker board ordering of two different atoms on A site, it is possible to induce G-type magnetic order on A site atoms at higher temperature than their Néel temperature. In this case we will have two different mechanism that makes these materials polar (checker board ordering of A site atoms and G-type ordering of A site atoms), switch-ability of which needs to be investigated.

Besides, our primary studies on Hysteresis behavior of these materials shows that we can reproduce well the *s* like shape of hysteresis loops close to the spin-reorientation and the rectangular shape far from this point. Hence this model can used to study hysteresis

loops and the exchange bias effects in these materials to study origin of the sign change in exchange bias effect with these materials.

We have further extended our magnetic model and used it to study the magnetoelectric response of these materials. The findings of our studies on ME response of $GdFeO_3$ can be generalized to other similar structures where we can estimate the magnitude of the magnetoelectric response based on the parameters fitted from DFT calculations. Our results also show the limitation of these materials as magneto electrics. For example if we want to have a A site magnetic ordering at high temperature (e.g., like Fe with 600 K Néel temperature), then changing its magnetic order would require a large magnetic field which hinders their use as ME devices. On the other hand if we use materials with large enough exchange interaction so that the operating temperature is close to the phase transition we can expect large ME responses.

According to our model, exchange interaction in RFeO$_3$ will create a nonlinear ME response. The ME response measured in $DyFeO_3$, and claimed to be originating from exchange interaction, is a linear response which is in conflict with our findings. The origin of this behavior is not explained well and needs further studies.

Publications list

- A. Sasani, J. Íñiguez, and E. Bousquet, Origin of nonlinear magnetoelectric response in rare-earth orthoferrite perovskite oxides, (arXiv:2107.03228).
- A. Sasani, J. Íñiguez, and E. Bousquet, Magnetic phase diagram of rare-earth orthorhombic perovskite oxides, Phys. Rev. B 104, 064431 (2021).
- Hortensius, J.R., Afanasiev, D., Sasani, A. et al. Ultrafast strain engineering and coherent structural dynamics from resonantly driven optical phonons in LaAlO3. npj Quantum Mater. 5, 95 (2020).
- D. Afanasiev, J. R. Hortensius, B. A. Ivanov, A. Sasani, E. Bousquet, Y. M. Blanter, R. V. Mikhaylovskiy, A. V. Kimel, and A. D. Caviglia, Ultrafast control of magnetic interactions via light-driven phonons, Nature Materials 20, 607–611 (2021).

Appendix A

Derivation of Heisenberg model

To model the magnetic properties of RMO_3 perovskite structures, we have used the following Hamiltonian which includes magnetic interactions for transition metal atoms, H^{MM}, and magnetic interaction between rare earth atoms H^{RR}, and the interaction between the two sublattices H^{RM} (Eq.A.1).

$$H = H^{MM} + H^{RM} + H^{RR} \tag{A.1}$$

The Hamiltonian for each of the sublattices can be written as following.
For the transition metal atoms we would have:

$$H^{MM} = H^{MM}_{ex} + H^{MM}_{DMI} + H^{MM}_{SIA}, \tag{A.2}$$

For the R atoms the DMI and exchange interactions are very small and can be neglected such that:

$$H^{RR} \approx H^{RR}_{SIA}, \tag{A.3}$$

and for the interaction between two sublattices we have:

$$H^{RM} = H^{RM}_{ex} + H^{RM}_{DMI}, \tag{A.4}$$

where the exchange and DMI interactions are considered to have the following forms respectively:

$$H_{Ex}^{ab} = \frac{1}{2}\sum_{ij}^{N}\left(J_{ab,ij}S_{i,a}.S_{j,b}\right) \tag{A.5}$$

$$H_{dmi}^{ab} = \frac{1}{2}\sum_{i,j}\left(D_{ab,ij}\times S_{j,a}\right).S_{i,b} \tag{A.6}$$

and the SIA is considered to have the following form on both magnetic sublattices:

$$H_{SIA}^{aa} = \sum_{i} K_a\left(S_{i,a}.\hat{e}_i\right)^2, \tag{A.7}$$

where i and j are magnetic lattice sites and the some is over magnetic sites with spin S and the $\hat{e}_i$ shows the SIA direction.

For these structures we have four different symmetry adapted spin states that can be written as shown in Eq. A.8 to Eq. A.11.

$$S_{i,a}^{\Gamma_1} = A_{a,x}(-1)^{(n_z^i)} + \bar{G}_{a,y}(-1)^{(n_x^i+n_y^i+n_z^i)} + C_{a,z}(-1)^{(n_x^i+n_y^i)} \tag{A.8}$$

$$S_{i,a}^{\Gamma_2} = F_{a,x} + C_{a,y}(-1)^{(n_x^i+n_z^i)} + \bar{G}_{a,z}(-1)^{(n_x^i+n_y^i+n_z^i)} \tag{A.9}$$

$$S_{i,a}^{\Gamma_3} = C_{a,x}(-1)^{(n_y^i+n_z^i)} + F_{a,y} + A_{a,z}(-1)^{(n_z^i)} \tag{A.10}$$

$$S_{i,a}^{\Gamma_4} = \bar{G}_{a,x}(-1)^{(n_x^i+n_y^i+n_z^i)} + A_{a,y}(-1)^{(n_z^i)} + F_{a,z} \tag{A.11}$$

Where the $\bar{G}$ shows the main spin direction while the other letters showing small cantings.

from now on we will only consider the state with G type order which is the dominant order in RMO_3s (i.e Γ_1, Γ_2 and Γ_4). The general spin state of the atoms in these representations could be written as Follows (Eq.A.12):

$$S_{i,a} = C_{\alpha,a}^{1}S_{i,a}^{\Gamma_1} + C_{\alpha,a}^{2}S_{i,a}^{\Gamma_2} + C_{\alpha,a}^{4}S_{i,a}^{\Gamma_4}, \tag{A.12}$$

where $C_{\alpha,a}^{g}$ is the ratio of the spins in g state.

Using these definitions we can write the exchange interactions for atom a as (Eq. A.13)

$$\begin{aligned}
H_{Ex}^{aa} &= \frac{1}{2}\sum_{i,j} J_{ij} S_{i,a}.S_{j,a} \\
&= \frac{1}{2}\sum_{i,j}\sum_{\alpha} J_{ij}(C_{\alpha,a}^{1}S_{i,\alpha}^{\Gamma_1} + C_{\alpha,a}^{2}S_{i,\alpha}^{\Gamma_2} + C_{\alpha,a}^{4}S_{i,\alpha}^{\Gamma_4}).(C_{\alpha,a}^{1}S_{i,\alpha}^{\Gamma_1} + C_{\alpha,a}^{2}S_{j,\alpha}^{\Gamma_2} + C_{\alpha,a}^{4}S_{j,\alpha}^{\Gamma_4}) \\
&= \frac{1}{2}\sum_{i,j}\sum_{\alpha} J_{ij}(C_{\alpha,a}^{1}C_{\alpha,a}^{1}S_{i,\alpha}^{\Gamma_1}S_{j,\alpha}^{\Gamma_1} + C_{\alpha,a}^{2}C_{\alpha,a}^{2}S_{i,\alpha}^{\Gamma_2}S_{j,\alpha}^{\Gamma_2} + C_{\alpha,a}^{4}C_{\alpha,a}^{4}S_{i,\alpha}^{\Gamma_4}S_{j,\alpha}^{\Gamma_4} \\
&+ 2C_{\alpha,a}^{1}C_{\alpha,a}^{2}S_{i,\alpha}^{\Gamma_1}S_{j,\alpha}^{\Gamma_2} + 2C_{\alpha,a}^{1}C_{\alpha,a}^{4}S_{i,\alpha}^{\Gamma_1}S_{j,\alpha}^{\Gamma_4} + 2C_{\alpha,a}^{2}C_{\alpha,a}^{4}S_{i,\alpha}^{\Gamma_2}S_{j,\alpha}^{\Gamma_4}) \\
&= H_{Ex}^{aa,\Gamma_1} + H_{Ex}^{aa,\Gamma_2} + H_{Ex}^{aa,\Gamma_4} + H_{Ex}^{aa,\Gamma_{12}} + H_{Ex}^{aa,\Gamma_{14}} + H_{Ex}^{aa,\Gamma_{24}}
\end{aligned} \tag{A.13}$$

This equation shows the exchange interaction between spins in each state (H_{Ex}^{aa,Γ_1}, H_{Ex}^{aa,Γ_2}, H_{Ex}^{aa,Γ_4}) and the exchange interaction beween two states $H_{Ex}^{aa,\Gamma_{14}}$, $H_{Ex}^{aa,\Gamma_{12}}$, $H_{Ex}^{aa,\Gamma_{24}}$.

Exchange interaction between two states can be written as Eq. A.14 which can be proven to be zero since the final result is the dot product of the spins between different modulations:

$$\begin{aligned}
H_{Ex}^{aa,\Gamma_{24}} &= \sum_{i,j}\sum_{\alpha} J_{ij}(C_{\alpha,a}^{2}C_{\alpha,a}^{4}S_{i,\alpha}^{\Gamma_2}S_{j,\alpha}^{\Gamma_4}) \\
&= \sum_{i,j} J_{ij}(F_{a,x}\bar{G}_{a,x}s_{i,x}^{\Gamma_2}s_{j,x}^{\Gamma_4} + C_{a,y}A_{a,y}s_{i,y}^{\Gamma_2}s_{j,y}^{\Gamma_4} + \bar{G}_{a,z}F_{a,z}s_{i,z}^{\Gamma_2}s_{j,z}^{\Gamma_4}) \\
&= \sum_{i,j} J_{ij}(F_{a,x}\bar{G}_{a,x}(-1)^{(n_x^i+n_y^i+n_z^i)} + C_{a,y}A_{a,y}(-1)^{(n_z^i)}(-1)^{(n_x^i+n_z^i)} \\
&+ \bar{G}_{a,z}(-1)^{(n_x^i+n_y^i+n_z^i)}F_{a,z}) = 0
\end{aligned} \tag{A.14}$$

such that we will have :

$$H_{Ex}^{aa,\Gamma_{12}} + H_{Ex}^{aa,\Gamma_{14}} + H_{Ex}^{aa,\Gamma_{24}} = 0, \tag{A.15}$$

and the Exchange interactions in this system can be written as follows which is the sum of the exchange interactions in each state:

$$H_{Ex}^{aa} = H_{Ex}^{aa,\Gamma_1} + H_{Ex}^{aa,\Gamma_2} + H_{Ex}^{aa,\Gamma_4} \tag{A.16}$$

To calculate the DMI in this system we can write:

$$\begin{aligned} H_{dmi}^{aa} &= \sum_{i,j} \left(D_{a,ij} \times S_{j,a}\right).S_{i,a} \\ &= \sum_{i,j} \left\{D_{a,ij} \times \left(C_{\alpha,a}^{1} S_{i,a}^{\Gamma_1} + C_{\alpha,a}^{2} S_{i,a}^{\Gamma_2} + C_{\alpha,a}^{4} S_{i,a}^{\Gamma_4}\right)\right\} . \left(C_{\alpha,a}^{1} S_{i,a}^{\Gamma_1} + C_{\alpha,a}^{2} S_{i,a}^{\Gamma_2} + C_{\alpha,a}^{4} S_{i,a}^{\Gamma_4}\right) \\ &= H_{dmi}^{aa,\Gamma_1} + H_{dmi}^{aa,\Gamma_2} + H_{dmi}^{aa,\Gamma_4} + H_{dmi}^{aa,\Gamma_{12}} + H_{dmi}^{aa,\Gamma_{14}} + H_{dmi}^{aa,\Gamma_{24}} \end{aligned} \tag{A.17}$$

It is shown that the DMI vector in these systems can be written as Eq .A.18. We are going to use this vector to describe the properties of these materials regarding DMI [81].

$$D_{aa,ij} = d_x^a (-1)^{n_{ij}^z} \hat{i} + d_y^a (-1)^{n_{ij}^x + n_{ij}^y + n_{ij}^z} \hat{j} + d_z^a (-1)^{n_{ij}^x + n_{ij}^y} \hat{k} \tag{A.18}$$

The DMI between two state can be proven to be zero since for this interaction also we will have product of the spins with two different modulations.(see Eq. A.19)

$$H_{dmi}^{aa,\Gamma_{24}} = \sum_{i,j} \left(D_{a,ij} \times S_{j,a}^{\Gamma_2}\right).S_{i,a}^{\Gamma_4} + \left(D_{a,ij} \times S_{j,a}^{\Gamma_4}\right).S_{i,a}^{\Gamma_2} = 0. \tag{A.19}$$

So, the DMI between two states would be as follows:

$$H_{dmi}^{aa} = H_{dmi}^{aa,\Gamma_1} + H_{dmi}^{aa,\Gamma_2} + H_{dmi}^{aa,\Gamma_4}. \tag{A.20}$$

Hence, the total Hamiltonian of the system can be written as follows:

$$H = H^{\Gamma_1} + H^{\Gamma_2} + H^{\Gamma_4}. \tag{A.21}$$

The exchange interaction in Γ_4 state can be written as in Eq. A.22. The n' is the nearest neighbours at the position i as shown in Fig A.1 and it can be $(\pm 1, 0, 0)$,$(0, \pm 1, 0)$,$(0, 0, \pm 1)$.

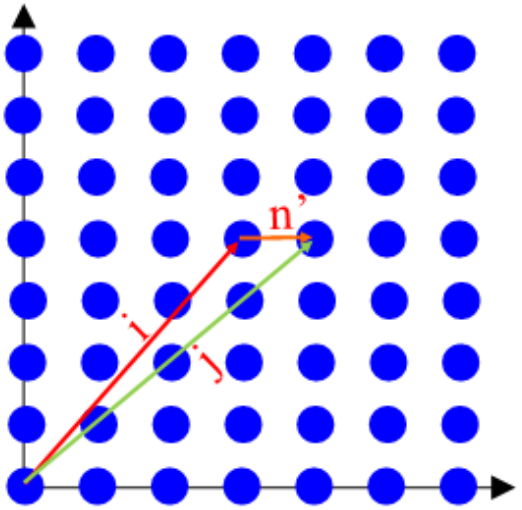

FIGURE A.1: Figure showing how we have considered nearest neigbours of position i.

$$
\begin{aligned}
H_{Ex}^{MM,\Gamma_4} &= \frac{1}{2}J_M \sum_i^N \sum_j^{NN} \bar{G}_{M,x}\bar{G}_{M,x}(-1)^{(n_x^i+n_y^i+n_z^i)}(-1)^{(n_x^j+n_y^j+n_z^j)} \\
&+ \frac{1}{2}J_M \sum_i^N \sum_j^{NN} A_{M,y}A_{M,y}(-1)^{(n_z^i)}(-1)^{(n_z^j)} + F_{M,z}F_{M,z}(1)^{n_x^i}(1)^{n_x^j} \\
&= \frac{1}{2}J_M \sum_i^N \sum_{n'}^{NN} (\bar{G}_{M,x}^2(-1)^{(n_x^i+n_y^i+n_z^i)}(-1)^{(n_x^i+n_y^i+n_z^i)}(-1)^{(n'_x+n'_y+n'_z)} \\
&+ (A_{M,y})^2(-1)^{(n_z^i)}(-1)^{(n_z^i)}(-1)^{(n'_z)} + (F_{M,z})^2(1)^{n_x^i}(1)^{n_x^i}(1)^{n'_x}) \\
&= -3J_M(\bar{G}_{M,x})^2 \sum_i^N (-1)^{2(n_x^i+n_y^i+n_z^i)} + J_M(A_{M,y})^2 \sum_i^N (-1)^{2(n_z^i)} \\
&+ 3J_M(F_{M,z})^2 \sum_i^N ((1)^{2(n_x^i)}) \\
&= -3NJ_M(\bar{G}_{M,x})^2 + NJ_M(A_{M,y})^2 + 3NJ_M(F_{M,z})^2
\end{aligned}
\tag{A.22}
$$

Similarly for H_{Ex}^{a,Γ_1} and H_{Ex}^{a,Γ_2} we can derive the following:

$$H_{Ex}^{MM,\Gamma_1} = NJ_M(A_{M,x})^2 - 3NJ_M(\bar{G}_{M,y})^2 - NJ_M(C_{M,z})^2, \tag{A.23}$$

$$H_{Ex}^{MM,\Gamma_2} = 3NJ_M(F_{M,x})^2 - NJ_M(C_{M,y})^2 - 3NJ_M(\bar{G}_{M,z})^2, \tag{A.24}$$

as well as for the exchange interactions between R and M sites we can write:

$$H_{Ex}^{RM,\Gamma_2} \simeq 8NJ_{RM}F_{M,x}F_{R,x}, \tag{A.25}$$

$$H_{Ex}^{RM,\Gamma_4} \simeq 8NJ_{RM}F_{M,z}F_{R,z}. \tag{A.26}$$

The DMI between M atoms in H_{dmi}^{M,Γ_4} can be written as follows:

$$\begin{aligned}
H_{dmi}^{MM,\Gamma_4} = \frac{1}{2}\sum_{i}^{N}\sum_{n'}^{NN} & \\
& \left(d_x^M(-1)^{(n_i^z)}(-1)^{(n'^z)}\hat{i} \times A_{M,y}(-1)^{(n_i^z)}(-1)^{(n'^z)}\hat{j}\right).S_{i,M}^{(\Gamma_4)} + \\
& \left(d_x^M(-1)^{(n_i^z)}(-1)^{(n'^z)}\hat{i} \times F_{M,z}\hat{k}\right).S_{i,M}^{(\Gamma_4)} + \\
& \left(d_y^M(-1)^{(n_i^x+n_i^y+n_i^z)}(-1)^{(n'^x+n'^y+n'^z)}\hat{j} \times \bar{G}_{M,x}(-1)^{(n_i^x+n_i^y+n_i^z)}(-1)^{(n'^x+n'^y+n'^z)}\hat{i}\right).S_{i,M}^{(\Gamma_4)} + \\
& \left(d_y^M(-1)^{(n_i^x+n_i^y+n_i^z)}(-1)^{(n'^x+n'^y+n'^z)}\hat{j} \times F_{M,z}\hat{k}\right).S_{i,M}^{(\Gamma_4)} + \\
& \left(d_z^M(-1)^{(n_i^x+n_i^y)}(-1)^{(n'^x+n'^y)}\hat{k} \times \bar{G}_{M,x}(-1)^{(n_i^x+n_i^y+n_i^z)}(-1)^{(n'^x+n'^y+n'^z)}\hat{i}\right).S_{i,M}^{(\Gamma_4)} + \\
& \left(d_z^M(-1)^{(n_i^x+n_i^y)}(-1)^{(n'^x+n'^y)}\hat{k} \times A_{M,y}(-1)^{(n_i^z)}(-1)^{(n'^z)}\hat{j}\right).S_{i,M}^{(\Gamma_4)},
\end{aligned} \tag{A.27}$$

and from this we can write:

$$\begin{aligned}
H_{dmi}^{MM,\Gamma_4} = \frac{1}{2}\sum_{i}^{N} & \\
& - 12d_x^M(-1)^{2(n_i^z)}A_{M,y}F_{M,z} - 12d_y^M(-1)^{2(n_i^x+n_i^y+n_i^z)}\bar{G}_{M,z} \\
& - 12d_z^M(-1)^{2n_i^z}\bar{G}_{M,x}A_{M,y} \\
& = -6Nd_x^M A_{M,y}F_{M,z} - 6Nd_y^M\bar{G}_{M,x}F_{M,z} - 6Nd_z^M\bar{G}_{M,x}A_{M,y}.
\end{aligned} \tag{A.28}$$

Similarly for H_{dmi}^{MM,Γ_1} and H_{dmi}^{MM,Γ_2} we can write:

$$H_{dmi}^{MM,\Gamma_1} = -6Nd_x^M\bar{G}_{M,y}C_{M,z} - 6Nd_y^M C_{M,z}A_{M,x} - 6Nd_z^M A_{M,x}\bar{G}_{M,y}, \tag{A.29}$$

$$H_{dmi}^{MM,\Gamma_2} = -6Nd_x^M C_{M,y}\bar{G}_{M,z} - 6Nd_y^M\bar{G}_{M,x} - 6Nd_z^M F_{M,x}C_{M,y}, \tag{A.30}$$

and for DMI between R and M we can write:

$$\begin{aligned}
H_{dmi}^{RM,\Gamma_4} = & \frac{1}{2}\sum_{i}^{N}\sum_{j}^{NN}((D_{ij} \times S_{j,M}^{\Gamma_4}).S_{i,R}^{\Gamma_4} \\
& + \frac{1}{2}\sum_{i}^{N}\sum_{j}^{NN}(D_{ij} \times S_{j,R}^{\Gamma_4}).S_{i,M}^{\Gamma_4}.
\end{aligned} \tag{A.31}$$

The first part of this equation is the DMI from 8 M neighbours of R and R which can be written as (Eq. A.21):

$$\begin{aligned}
&\frac{1}{2}\sum_{i}^{N}\sum_{j}^{NN}(D_{ij}\times S_{j,M}^{\Gamma_4}).S_{i,R}^{\Gamma_4}= \\
&\frac{1}{2}\sum_{i}^{N}\sum_{n'}^{8}\left(d_y^{RM}(-1)^{(n_i^x+n_i^y+n_i^z)}(-1)^{(n'^x+n'^y+n'^z)}\hat{j}\times\bar{G}_{M,x}(-1)^{(n_i^x+n_i^y+n_i^z)}(-1)^{(n'^x+n'^y+n'^z)}\hat{i}\right).S_{i,R}^{\Gamma_4}+ \\
&\frac{1}{2}\sum_{i}^{N}\sum_{n'}^{8}\left(d_x^{RM}(-1)^{(n_i^z)}(-1)^{(n'^z)}\hat{i}\times A_{M,y}(-1)^{(n_i^z)}(-1)^{(n'^z)}\hat{j}\right).S_{i,R}^{\Gamma_4} \\
&=\frac{1}{2}\sum_{i}^{N}-8d_y^{RM}(-1)^{2(n_i^x+n_i^y+n_i^z)}\bar{G}_{M,x}F_{z,R}-8d_x^{RM}(-1)^{2(n_i^z)}A_{M,y}F_{z,R} \\
&=-4Nd_y^{RM}\bar{G}_{M,x}F_{z,R}-4Nd_x^{RM}A_{M,y}F_{z,R}
\end{aligned} \tag{A.32}$$

The interaction of Fe with its 8 R neighbours is as follows:

$$\begin{aligned}
&\frac{1}{2}\sum_{i}^{N}\sum_{j}^{NN}(D_{ij}\times S_{j,R}^{\Gamma_4}).S_{i,Fe}^{\Gamma_4}= \\
&\frac{1}{2}\sum_{i}^{N}\sum_{n'}^{8}(d_y^{RM}(-1)^{n_i^x+n_i^y+n_i^z}\hat{j}\times F_{z,R}\hat{k}).S_{i,Fe}^{\Gamma_4}+ \\
&\frac{1}{2}\sum_{i}^{N}\sum_{n'}^{8}(d_x^{RM}(-1)^{n_i^z}(-1)^{(n'^z)}\hat{i}\times A_{M,y}(-1)^{(n_i^z)}(-1)^{(n'^z)}\hat{j}).S_{i,Fe}^{\Gamma_4} \\
&=-\frac{1}{2}\sum_{i}^{N}(8d_y^{RM}(-1)^{2(n_i^x+n_i^y+n_i^z)}F_{z,R}\bar{G}_{M,x}+8Nd_x^{RM}(-1)^{(2n_i^z)}A_{M,y}F_{z,R}) \\
&=-4Nd_y^{RM}F_{z,R}\bar{G}_{M,x}-4Nd_x^{RM}A_{M,y}F_{z,R}
\end{aligned} \tag{A.33}$$

Finally for the DMI between R and M we can write:

$$H_{dmi}^{RM,\Gamma_4}=-8Nd_x^{RM}F_{z,R}A_{M,y}-8Nd_y^{RM}F_{R,z}\bar{G}_{M,x}, \tag{A.34}$$

and similarly for the other states we can write:

$$H_{dmi}^{RM,\Gamma_1}=-8Nd_x^{RM}C_{R,z}\bar{G}_{M,y}-8Nd_y^{RM}C_{R,z}A_{M,x}, \tag{A.35}$$

$$\begin{aligned}
H_{dmi}^{RM,\Gamma_2}=&-8Nd_x^{RM}\bar{G}_{M,z}C_{R,y}-8Nd_y^{RM}F_{R,x}\bar{G}_{M,z} \\
&-8Nd_z^{RM}F_{R,x}C_{M,y}-8Nd_z^{RM}C_{R,y}F_{M,x}.
\end{aligned} \tag{A.36}$$

By summing all the energy components and by including SIA energy we can reach the final energy of each states as follows:

$$\begin{aligned} H^{\Gamma_1} =& H^M_{ex} + H^M_{DMI} + H^{RM}_{ex} + H^{RM}_{DMI} \\ =& NJ^M(A_{M,x})^2 - 3NJ^M(\bar{G}_{M,y})^2 - NJ^M(C_{M,z})^2 \\ & - 6Nd^M_x \bar{G}_{M,y} C_{M,z} - 6Nd^M_y C_{M,z} A_{M,x} - 6Nd^M_z A_{M,x} \bar{G}_{M,y} \\ & - 8Nd^{RM}_x C_{R,z} \bar{G}_{M,y} - 8Nd^{RM}_y C_{R,z} A_{M,x} \end{aligned} \tag{A.37}$$

$$\begin{aligned} H^{\Gamma_2} =& H^M_{ex} + H^M_{DMI} + H^{RM}_{ex} + H^{RM}_{DMI} \\ =& 3NJ^M(F_{M,x})^2 - NJ^M(C_{M,y})^2 - 3NJ^M(\bar{G}_{M,z})^2 \\ & - 6Nd^M_x C_{M,y} \bar{G}_{M,z} - 6Nd^M_y \bar{G}_{M,z} F_{M,x} - 6Nd^M_z F_{M,x} C_{M,y} \\ & - 8NJ^{RM} F_{M,x} F_{R,x} - 8Nd^{RM}_x \bar{G}_{M,z} C_{R,y} - 8Nd^{RM}_y F_{R,x} \bar{G}_{M,z} \\ & - 8Nd^{RM}_z F_{R,x} C_{M,y} - 8Nd^{RM}_z C_{R,y} F_{M,x} \end{aligned} \tag{A.38}$$

$$\begin{aligned} H^{\Gamma_4} =& H^M_{ex} + H^M_{DMI} + H^{RM}_{ex} + H^{RM}_{DMI} + H^R_{SIA} + H^M_{SIA} \\ =& -3NJ^M(\bar{G}_{M,x})^2 + NJ^M(A_{M,y})^2 + 3NJ^M(F_{M,z})^2 \\ & - 6Nd^M_x A_{M,y} F_{M,z} - 6Nd^M_y \bar{G}_{M,x} F_{M,z} - 6Nd^M_z \bar{G}_{M,x} A_{M,y} \\ & - 8NJ^{RM} F_{M,z} F_{R,z} - 8Nd^{RM}_x F_{z,R} A_{M,y} - 8Nd^{RM}_y F_{R,z} \bar{G}_{M,x} \\ & - NK^M(\bar{G}_{M,x})^2 - NK^R(\bar{G}_{R,x})^2 \end{aligned} \tag{A.39}$$

Appendix B

Technical details

B.1 Chapter 3

The main goal of this chapter is to give a qualitative picture of the magnetic properties of RMO_3's. We choose to work with Gd because the DFT calculation results are more robust and reliable for fully filed f-electron channel (Gd-f^7) that does not have many multiplets. However, the Gd ion is a special case with a very small angular momentum compared to the other rare-earth elements but, once the model is built for Gd, we can tune the model parameter values, i.e., the single-ion anisotropy and DMI, to reproduce the physics of the other rare-earth atoms.

To understand these magnetic behaviors we have used DFT calculations on $GdFeO_3$ and $GdCrO_3$, as reference materials, to have an estimation of the the magnetic interactions in these crystals. We then tuned these parameters to study how they affect the overall magnetic behavior of the system. We build a Heisenberg model containing M-M and M-R superexchange and DMI interactions. Because we will focus on the temperature range where the R sublattice is paramagnetic, we will neglect the R-R interactions (these interactions are nevertheless small as compared to the M-M and M-R couplings). We fit this model against DFT calculations [25, 26] done for the orthorhombic $Pnma$ phase of $GdFeO_3$ and $GdCrO_3$. We used the VASP package [194, 195] and its projected augmented wave implementation of DFT [196]. We used the so-called PBEsol-GGA [197] functional for the exchange correlation part of the density functional; a Hubbard U correction [198] on Fe, Cr, and Gd of, respectively, 4, 2, and 5 eV has been used with J parameter of 1 and 0.5 eV on Fe and Cr. All the calculations were done with a 6×6×4 mesh of k points for sampling the reciprocal space and a cut-off energy on the plane-wave expansion of 700 eV to have a good convergence on single-ion anisotropic and DMIs (less than 5 μeV convergence).

The calculations of the superexchange interactions were done using Green's function method as implemented in the TB2J [51] code. In this method the maximally localized Wannier function [52] as implemented in WANNIER90 [53] are calculated using DFT (VASP interface to maximally localized Wannier functions) and using these Wannier functions and the Green's function method, the superexchange parameters are calculated. Some of these superexchange interactions were compared to the ones calculated using total energy to ensure the consistency of the method. To calculate the DMI couplings, we calculated the energy of different spin configurations and used the method given by Xiang *et al.* [46]. We have checked that the results are qualitatively the same by using different Hubbard U and J corrections while we have used the ones giving the best Néel temperature for both sublattices. All of the fitted magnetic interaction parameters were used to do spin dynamics with the VAMPIRE code [199]. In this code the Landau-Lifshitz-Gilbert (LLG) equation for the spin dynamics [Eq. (B.1)] is solved numerically.

$$\frac{\partial S_i}{\partial t} = \frac{\gamma}{1+\lambda^2}\left[S_i \times B^i_{eff} + \lambda S_i \times \left(S_i \times B^i_{eff}\right)\right] \tag{B.1}$$

In the temperature-dependent spin dynamics simulations we have used a simulation cell of 20 nanometers in each direction. The thermalization step was done in 50000 time steps of 1.5 fs and the measurement is done in 90000 time steps of 1.5 fs.

B.2 Chapter 4

In this work we have used the Heisenberg model that has been derived previously by us in Ref. [160], which includes both rare earth and transition metal site interactions (superexchange and Dzyaloshinskii-Moriya interactions). This model is fitted against density functional theory (DFT) calculations [25, 26] of the $Pna2_1$ phase of $GdFeO_3$. We used the VASP DFT package [194, 195] and its projected augmented wave implementation [196]. We used the so-called generalized gradient approximation (GGA) of the PBEsol flavor [197] for the exchange correlation functional and added a Hubbard U correction [198] on Fe and Gd of respectively 4 eV and 5 eV as well as a J parameter of 1 eV on Fe. Since the behavior that we are interested in is arising from exchange interactions, we have chosen Hubbard interaction parameters (U) so that we get the closest Néel temperature compared to experiments. All the calculations were done considering non-collinear magnetism and including the spin orbit interaction. The calculations were converged with a 6×6×4 mesh of k-points for sampling the reciprocal space and a cut-off

energy on the plane wave expansion of 700 eV (giving a precision of less than 5 μeV on the single-ion anisotropy and the DMIs).

The calculations of the superexchange interactions were done using Green's function method as implemented in the TB2J [51] code. In this method the maximally localized Wannier function [52] as implemented in WANNIER90 [53] are calculated using DFT (VASP interface to Maximally localized Wannier functions) and, using these Wannier functions and the Green's function method, the superexchange parameters are calculated. Some of these superexchange interactions were compared to the ones calculated using total energy to ensure the consistency of the method. To determine the DMI amplitudes, we have calculated the energy of different spin configurations as described by Xiang *et al.* [46]. All of the fitted magnetic interaction parameters were used to do spin dynamics with the VAMPIRE code [199]. In this code the Landau-Lifshitz-Gilbert (LLG) equation for the spin dynamics

$$\frac{\partial S_i}{\partial t} = \frac{\gamma}{1+\lambda^2}\left[S_i \times B^i_{eff} + \lambda S_i \times \left(S_i \times B^i_{eff}\right)\right] \tag{B.2}$$

is solved numerically. The ground state (lowest energy solution at T=0 K) for each of the calculations (with applied magnetic field) is found by minimizing the energy with respect to the magnetic order .

The calculation of the polarization is done using the Berry phase approach as implemented in VASP [200, 201]. In order to calculate the ferroelectric response as a function of magnetic order in the structure, we have constrained magnetic order and rotated the spins on rare earth site from antiferroamgnetic order to feromagnetic order and relaxed the atomic structure at each step. To make a model to simulate the ME response of the materials we have fitted the spin dynamics results with the models that we have developed in the following.

B.3 Chapter 5

In the experiment, laser driven spin dynamics of a [001] cut single crystal of $DyFeO_3$ is studied. The laser provide an intense (with electric field of more than 10 MV cm^{-1} with polarization direction in ab plane of the crystal) phase locked mid-infrared impulsive source (250 fs, 1 kHz); which is tunable in a broad photon energy range from 65 to 250 meV (16-60 THz). The energy range provided by the laser can be in the range of the highest frequency IR active transversal optical phonon mode centered at 70 meV of the $DyFeO_3$ crystal. The spin dynamics were measured using a pomp-probe scheme, by

tracking the polarization rotation, imprinted by the magneto-optical Faraday effect, on co-propagating near-infrared probe pulses at the photon energy of 1.55 eV.

To address the origin of the behaviors observed in the experiments, we simulated the *Pnma* phase of $DyFeO_3$ through density functional theory (DFT) [25, 26] and its projected augmented wave (PAW) [196] flavor as implemented in the ABINIT package [202, 203]. The PAW atomic potentials used for Fe and O were from the GBRV pseudopotential library [204] with $3s$, $3p$, $3d$, $4s$ and $2s$, $2p$ considered as valence states for Fe and O respectively. For Dy we used the PAW atomic potential from M. Topsakal *et. al.* [205]. For Dy potential we considered two different cases: one where the valance states are $4f$, $5s$, $5p$ and $6s$ (with f electrons in the valence) and one where we have put the f states in the core such that the valence electrons are $5s$, $5p$ and $6s$. We used the PBEsol [197] GGA functional for the exchange correlation interaction and a Hubbard correction [198] on both Fe and Dy of respectively 4 and 7 eV have been used to have the closest possible properties with respect to experiments (band gaps, lattice constants and Neel temperature). All the calculation was done with $6\times6\times4$ mesh of k-points for the reciprocal space and a cut-off energy on the plane wave expansion of 36 Hartree and 72 Hartree for the second finer grid inside the PAW spheres. To calculate the phonons, the frozen phonon scheme has been used through the Phonopy software [206].

The calculations of the exchange interactions were done using Green's function method as implemented in the TB2J [51] code. In this method the maximally localized Wannier function [52] as implemented in WANNIER90 [53] are calculated using DFT (VASP interface to Maximally localized Wannier functions) and using these Wannier functions and the Green's function method, the superexchange parameters are calculated. Some of these superexchange interactions were compared to the ones calculated using total energy to ensure the consistency of the method.

Appendix C

f electrons ground state

We have considered the occupations of the f orbitals with respect to the symmetry given by the crystal field splitting of Dy environment in $DyFeO_3$. The crystal field splits the 7 degenerate f orbitals of the Dy to 7 different energy levels and these state are mixed as follows:

$$\Psi_{\mathrm{i}} = \sum_{m} c_{\mathrm{m}} |\mathrm{l,m}>$$

where $m = -3, -1, 1, 3$ and

$$\Psi_{\mathrm{j}} = \sum_{\mathrm{m}'} c_{\mathrm{m}'} |\mathrm{l,m}'>$$

where $m' = -2, 0, 2$.

f electrons calculations

We have started from different occupation matrices and forced (constrained) these initialized occupation matrices for the first 30 self-consistent field cycles (SCF) of each ionic relaxation step, the constraint being fully released beyond 30 SCF. We summarize in Tab. C.1 the resulting occupation state for each starting occupation case, their relative energy with respect to the lowest energy case and the relaxed cell parameters. The states shown in Tab. C.1 are the states that have converged, other state either did not converged or relaxed to the same states as shown in table.

Among the converged states shown in Tab. C.1, states 1 and 7 are degenerate and states 5,6,8 are also degenerate.

TABLE C.1: Energies and relaxed cell parameters of the different Dy-f orbitals occupation matrices. The second column represents the starting occupation state and the third column shows the resulting occupation state obtained after full relaxation and release of the constraint. The fourth column shows the relative energy with respect to the lowest energy state and the last three columns shows the associated relaxed cell parameters (Angstrom).

#	starting state	final state	ΔE	a	b	c
1	(1 -1 3)(3 -1 1)	(-3 -1 1)(-1 -3 3)	0.3	5.291	5.595	7.616
2	(0 -3)(2)	(-3 0)(2 -1)	18.2	5.284	5.601	7.615
3	(-1 -3) (2)	(-3 0) (2 -1)	18.7	5.282	5.603	7.615
4	(1 3) (2)	(1 3) (2)	52.3	5.279	5.601	7.620
5	(1 0 2 3) (3 1 0 1)	(3 0)(2 0 -1 -2)	7.7	5.275	5.609	7.616
6	(0 3 2) (2 -3 -2 -1 0)	(3 0)(2 0 -1 -2)	7.5	5.274	5.610	7.616
7	(-3 1 -1) (-1 3 1)	(-3 -1 1)(-1 -3 3)	0.0	5.292	5.594	7.615
8	(-1 0 2)(3 -1)	(2 0 -1 -2) (3 0)	7.4	5.274	5.611	7.616

Appendix D

Phonons

D.1 Phonons of $GdFeO_3$ for different magnetic ordering of Fe

TABLE D.1: A2 mode phonons for $GdFeO_3$

label	G-type	label	F-type	label	C-type	label	A-type
A2	81.6	A2	83.0	A2	81.3	A	84.2
A2	106.8	B2	107.4	B2	106.6	A	106.9
A2	155.9	B1	155.1	B2	156.4	A	154.9
A2	159.6	A2	159.8	A2	159.8	A	159.0
A2	195.4	A2	189.7	A2	192.4	A	192.3
A2	238.3	A1	238.3	B1	239.1	B	233.6
A2	284.7	B2	286.8	B2	286.9	A	283.5
A2	298.6	A2	302.7	A2	299.2	A	301.8
A2	342.7	A2	348.6	B1	346.0	A	347.0
A2	346.5	A1	350.2	A2	346.9	B	349.2
A2	463.1	B2	461.0	B2	461.3	A	460.5
A2	489.9	A1	491.0	B1	485.3	A	488.8
A2	512.9	B2	507.0	A2	512.3	A	508.0
A2	516.0	A2	507.5	B2	512.5	A	515.8
A2	606.3	B2	631.5	B2	606.7	A	628.6

Tab. D.1 and Tab D.2 represents the phonon modes frequencies in cm^{-1} for G-type, F-type, C-type, and A-type ordering of Fe sublattice in $GdFeO_3$. In these calculations the Gd sublattice had G-type order. In the Tab D.2 the first column represents the mode effective charges (Z^*) in electronic unit charge (e).

D.2 Phonons of $DyFeO_3$

TABLE D.2: IR-active phonons for $GdFeO_3$

Z*	label	G-type	label	F-type	label	C-type	label	A-type
z-direction								
-0.1	A1	108.2	A1	108.9	A1	108.3	A	109.3
-0.1	A1	134.1	A1	136.6	A1	134.6	A	135.4
4.3	A1	159.2	B2	158.3	B1	159.6	A	156.9
-4.2	A1	163.2	B1	164.0	B1	165.1	A	161.2
-0.1	A1	246.4	B2	241.5	A1	247.5	B	236.6
-7.3	A1	261.7	B1	255.0	B1	256.0	A	261.3
-2.9	A1	297.5	B1	302.5	B1	298.0	B	301.6
0.0	A1	321.3	A1	322.5	B2	320.9	A	322.7
6.9	A1	342.3	B1	345.6	B2	343.1	B	342.5
-0.1	A1	393.0	A1	405.3	A1	394.1	A	396.2
0.1	A1	405.5	A1	410.1	A1	407.5	A	405.6
0.0	A1	467.3	A1	473.8	A1	468.0	A	469.3
0.6	A1	487.6	A2	478.4	B2	485.1	B	482.6
4.0	A1	525.6	B2	521.8	B1	521.0	A	523.9
y-direction								
-0.8	B1	99.9	B2	104.7	A1	100.5	B	103.7
0.0	B1	143.6	A2	140.4	B1	142.8	B	141.6
2.4	B1	187.9	B2	187.2	A1	188.8	B	186.5
6.6	B1	236.4	A2	229.8	A1	238.5	A	229.3
0.0	B1	239.1	A2	240.0	A2	239.2	B	235.4
2.9	B1	287.1	B2	291.2	A1	288.0	B	287.1
10.2	B1	303.2	B1	306.0	A1	307.9	A	302.9
0.9	B1	327.8	B2	331.2	A1	328.3	B	329.1
0.0	B1	347.0	A2	352.4	B2	349.2	A	351.3
1.7	B1	414.1	A2	417.4	A2	412.5	B	413.5
3.2	B1	414.8	B1	418.5	A1	418.5	B	420.7
3.4	B1	508.4	B2	495.2	A1	509.2	B	504.9
-0.7	B1	517.7	B1	518.2	A1	516.3	B	517.7
0.0	B1	588.6	A2	609.9	B1	603.7	B	587.7
x-direction								
1.0	B2	109.7	A1	115.3	B2	109.7	B	113.9
0.1	B2	126.3	B1	127.8	A2	127.3	B	125.6
5.4	B2	171.7	A1	173.8	B2	174.5	B	170.4
8.7	B2	246.7	A1	251.1	B2	250.4	A	246.4
-4.4	B2	277.0	A1	283.8	B2	281.5	B	278.3
0.0	B2	309.0	B2	309.5	A2	309.4	B	304.9
1.0	B2	316.0	A1	319.2	A1	319.8	B	313.9
4.4	B2	342.0	B2	343.6	B1	340.2	A	339.8
6.0	B2	381.7	A1	386.1	B2	382.1	B	384.3
0.1	B2	414.3	B2	418.0	B1	415.5	B	415.4
0.0	B2	446.3	B1	446.5	A2	446.3	B	445.1
1.1	B2	480.8	B1	478.0	A2	479.3	A	480.0
-2.5	B2	536.8	A1	533.8	B2	535.7	B	535.2
0.0	B2	636.8	B1	661.3	A2	641.3	B	650.3

TABLE D.3: Calculated $DyFeO_3$ Raman active mode frequency (cm^{-1}). In the first column we show the mode label within the *Pnma* structure and in the second column we report the frequency of the mode with f electron in the core. The third column presents the mode labels in the $Pna2_1$ space group and the last column is the frequency of the mode in $Pna2_1$ structure by considering the f electrons in the valence with the G-type AFM ordering of the Dy. The last column give the frequency difference between the two cases. In the fifth and sixth column we also report, respectively, the calculated frequencies and the experimental measurements reported by Weber *et al.* in Ref. [187].

label(*Pnma*)	$f_{\text{in-core}}$	label($Pna2_1$)	f_{valence}	ref	exp	Δ
$A_g(1)$	109	$A_1(1)$	107	112	113	2
$A_g(2)$	129	$A_1(2)$	133	135	140	-4
$A_g(3)$	255	$A_1(3)$	249	262	261	6
$A_g(4)$	330	$A_1(4)$	328	332	341	2
$A_g(5)$	401	$A_1(5)$	408	422	422	-6
$A_g(6)$	415	$A_1(6)$	408	415	417	7
$A_g(7)$	401	$A_1(7)$	413	422	422	-11
$A_g(8)$	479	$A_1(8)$	480	490	496	-1
$B_{1g}(1)$	129	$B_1(1)$	136	135	–	-7
$B_{1g}(2)$	241	$B_1(2)$	245	250	–	-4
$B_{1g}(3)$	351	$B_1(3)$	353	359	361	-2
$B_{1g}(4)$	412	$B_1(4)$	419	427	427	-7
$B_{1g}(5)$	585	$B_1(5)$	591	593	–	-6
$B_{2g}(1)$	105	$A_2(1)$	107	109	111	-3
$B_{2g}(2)$	157	$A_2(2)$	155	161	163	2
$B_{2g}(3)$	307	$A_2(3)$	298	311	325	9
$B_{2g}(4)$	346	$A_2(4)$	348	351	–	-2
$B_{2g}(5)$	479	$A_2(5)$	474	482	494	4
$B_{2g}(6)$	527	$A_2(6)$	527	534	–	0
$B_{2g}(7)$	607	$A_2(7)$	610	612	624	-3
$B_{3g}(1)$	117	$B_2(1)$	120	123	–	-3
$B_{3g}(2)$	304	$B_2(2)$	307	311	–	-4
$B_{3g}(3)$	408	$B_2(3)$	417	424	433	-9
$B_{3g}(4)$	453	$B_2(4)$	455	460	474	-1
$B_{3g}(5)$	629	$B_2(5)$	637	637	639	-8

TABLE D.4: Calculated $DyFeO_3$ phonon IR active mode frequency (cm^{-1}). The first column gives the mode label of the *Pnma* structure with *f* electrons in the core and the second column the calculated frequency. The third column presents the mode label in the $Pna2_1$ space group and the fourth column the corresponding calculated frequencies with *f* electrons in the valence. The last column (Δ) gives the difference in frequency between $f_{\text{in-core}}$ and f_{valence}.

label(*Pnma*)	$f_{\text{in-core}}$	label($Pna2_1$)	f_{valence}	Δ
$B_{1u}(1)$	109	$B_2(6)$	106	2
$B_{1u}(2)$	168	$B_2(7)$	175	-7
$B_{1u}(3)$	244	$B_2(8)$	250	-6
$B_{1u}(4)$	274	$B_2(9)$	278	-3
$B_{1u}(5)$	324	$B_2(10)$	322	2
$B_{1u}(6)$	346	$B_2(11)$	347	-1
$B_{1u}(7)$	399	$B_2(12)$	393	6
$B_{1u}(8)$	501	$B_2(13)$	497	4
$B_{1u}(9)$	541	$B_2(14)$	543	-2
$B_{2u}(1)$	148	$A_1(9)$	152	-4
$B_{2u}(2)$	159	$A_1(10)$	162	-2
$B_{2u}(3)$	253	$A_1(11)$	260	-6
$B_{2u}(4)$	299	$A_1(12)$	300	-1
$B_{2u}(5)$	348	$A_1(13)$	351	-2
$B_{2u}(6)$	480	$A_1(14)$	490	-9
$B_{2u}(7)$	515	$A_1(15)$	527	-12
$B_{3u}(1)$	97	$B_1(6)$	100	-2
$B_{3u}(2)$	189	$B_1(7)$	187	2
$B_{3u}(3)$	228	$B_1(8)$	234	-6
$B_{3u}(4)$	289	$B_1(9)$	290	-0
$B_{3u}(5)$	307	$B_1(10)$	309	-1
$B_{3u}(6)$	333	$B_1(11)$	332	1
$B_{3u}(7)$	425	$B_1(12)$	424	1
$B_{3u}(8)$	510	$B_1(13)$	514	-4
$B_{3u}(9)$	523	$B_1(14)$	525	-2

Bibliography

[1] Jiles David. *Introduction to Magnetism and Magnetic Materials*. CRC Press, Boca Raton, 2015. doi:10.1201/b18948.

[2] Hans Christian Ørsted, P. O. Pedersen, and Burndy Library. Experimenta circa effectum conflictus electrici in acum magneticam. *Typis Schultzianis*, 1820.

[3] James Clerk Maxwell. Dynamical theory of the electromagnetic field. *Trans. Roy. Soc.*, CLV, 1865.

[4] chemistry, 2021. URL https://chemistry.stackexchange.com/questions/49248/what-is-the-difference-between-a-positive-and-negative-electron-orbital.

[5] Ralph Skomski. *Simple Models of Magnetism*. Oxford University Press, UK, Oxford, 2008. doi:10.1093/acprof:oso/9780198570752.001.0001.

[6] H.A Kramers. L'interaction entre les atomes magnétogènes dans un cristal paramagnétique. *Physica*, 1(1):182–192, 1934. ISSN 0031-8914. doi:10.1016/S0031-8914(34)90023-9.

[7] P. W. Anderson. New approach to the theory of superexchange interactions. *Phys. Rev.*, 115:2–13, Jul 1959. doi:10.1103/PhysRev.115.2.

[8] Clarence Zener. Interaction between the d-shells in the transition metals. ii. ferromagnetic compounds of manganese with perovskite structure. *Phys. Rev.*, 82: 403–405, May 1951. doi:10.1103/PhysRev.82.403.

[9] M. A. Ruderman and C. Kittel. Indirect Exchange Coupling of Nuclear Magnetic Moments by Conduction Electrons. *Physical Review*, 96(1):99–102, October 1954. doi:10.1103/PhysRev.96.99.

[10] T. Kasuya. A Theory of Metallic Ferro- and Antiferromagnetism on Zener's Model. *Progress of Theoretical Physics*, 16(1):45–57, July 1956. doi:10.1143/PTP.16.45.

[11] Kei Yosida. Magnetic Properties of Cu-Mn Alloys. *Physical Review*, 106(5):893–898, June 1957. doi:10.1103/PhysRev.106.893.

[12] F. Bloch and G. Gentile. Zur Anisotropie der Magnetisierung ferromagnetischer Einkristalle. *Zeitschrift für Physik*, 70(5-6):395–408, 1931. ISSN 14346001. doi:10.1007/BF01339586.

[13] Louis Néel. Preuves expérimentales du ferromagnétisme et de l'antiferromagnétisme. *Annales de l'Institut Fourier*, 1:163–183, 1949. doi:10.5802/aif.13.

[14] I. Dzyaloshinsky. A thermodynamic theory of "weak" ferromagnetism of antiferromagnetics. *Journal of Physics and Chemistry of Solids*, 4(4):241–255, January 1958. doi:10.1016/0022-3697(58)90076-3.

[15] Tôru Moriya. Anisotropic superexchange interaction and weak ferromagnetism. *Phys. Rev.*, 120:91–98, Oct 1960. doi:10.1103/PhysRev.120.91.

[16] E. Schrödinger. Quantisierung als eigenwertproblem. *Annalen der Physik*, 384(4): 361–376, 1926. doi:10.1002/andp.19263840404.

[17] Attila Szabo and Neil S. Ostlund. *Modern Quantum Chemistry: Introduction to Advanced Electronic Structure Theory*. Dover Publications, Inc., Mineola, first edition, 1996.

[18] M. Born and R. Oppenheimer. Zur quantentheorie der molekeln. *Annalen der Physik*, 389(20):457–484, 1927. doi:10.1002/andp.19273892002.

[19] H Hellmann. *Einführung in die Quantenchemie*. Franz Duetsche, Leipzig, 1937. doi:/10.1002/ange.19410541109.

[20] R. P. Feynman. Forces in molecules. *Phys. Rev.*, 56:340–343, Aug 1939. doi:10.1103/PhysRev.56.340.

[21] D. R. Hartree. The wave mechanics of an atom with a non-coulomb central field. part i. theory and methods. *Mathematical Proceedings of the Cambridge Philosophical Society*, 24(1):89–110, 1928. doi:10.1017/S0305004100011919.

[22] J. C. Slater. The Self Consistent Field and the Structure of Atoms. *Physical Review*, 32(3):339–348, September 1928. doi:10.1103/PhysRev.32.339.

[23] L. H. Thomas. The calculation of atomic fields. *Mathematical Proceedings of the Cambridge Philosophical Society*, 23(5):542–548, 1927. doi:10.1017/S0305004100011683.

[24] E. Fermi. Un metodo statistico per la determinazione di alcune prioprietà dell'atomo. *Accademia Nazionale dei Lincei*, 6:602–607, 1927.

[25] P. Hohenberg and W. Kohn. Inhomogeneous electron gas. *Phys. Rev.*, 136:B864–B871, Nov 1964. doi:10.1103/PhysRev.136.B864.

[26] W. Kohn and L. J. Sham. Self-consistent equations including exchange and correlation effects. *Phys. Rev.*, 140:A1133, 1965. doi:10.1103/PhysRev.140.A1133.

[27] D. M. Ceperley and B. J. Alder. Ground state of the electron gas by a stochastic method. *Phys. Rev. Lett.*, 45:566–569, Aug 1980. doi:10.1103/PhysRevLett.45.566.

[28] J. P. Perdew and Alex Zunger. Self-interaction correction to density-functional approximations for many-electron systems. *Phys. Rev. B*, 23:5048–5079, May 1981. doi:10.1103/PhysRevB.23.5048.

[29] John P. Perdew and Yue Wang. Accurate and simple analytic representation of the electron-gas correlation energy. *Phys. Rev. B*, 45:13244–13249, Jun 1992. doi:10.1103/PhysRevB.45.13244.

[30] S. H. Vosko, L. Wilk, and M. Nusair. Accurate spin-dependent electron liquid correlation energies for local spin density calculations: a critical analysis. *Canadian Journal of Physics*, 58(8):1200–1211, 1980. doi:10.1139/p80-159.

[31] John P. Perdew, Adrienn Ruzsinszky, Jianmin Tao, Viktor N. Staroverov, Gustavo E. Scuseria, and Gábor I. Csonka. Prescription for the design and selection of density functional approximations: More constraint satisfaction with fewer fits. *The Journal of Chemical Physics*, 123(6):062201, 2005. doi:10.1063/1.1904565.

[32] John P. Perdew, Kieron Burke, and Matthias Ernzerhof. Generalized gradient approximation made simple. *Phys. Rev. Lett.*, 77:3865–3868, Oct 1996. doi:10.1103/PhysRevLett.77.3865.

[33] Jianmin Tao, John P. Perdew, Viktor N. Staroverov, and Gustavo E. Scuseria. Climbing the density functional ladder: Nonempirical meta–generalized gradient approximation designed for molecules and solids. *Phys. Rev. Lett.*, 91:146401, Sep 2003. doi:10.1103/PhysRevLett.91.146401.

[34] Vladimir I Anisimov, F Aryasetiawan, and A I Lichtenstein. First-principles calculations of the electronic structure and spectra of strongly correlated systems: the lda+u method. *Journal of Physics: Condensed Matter*, 9(4):767–808, jan 1997. doi:10.1088/0953-8984/9/4/002.

[35] Vladimir I. Anisimov, Jan Zaanen, and Ole K. Andersen. Band theory and mott insulators: Hubbard u instead of stoner i. *Phys. Rev. B*, 44:943–954, Jul 1991. doi:10.1103/PhysRevB.44.943.

[36] J. Hubbard and Brian Hilton Flowers. Electron correlations in narrow energy bands. *Proceedings of the Royal Society of London. Series A. Mathematical and Physical Sciences*, 276(1365):238–257, 1963. doi:10.1098/rspa.1963.0204.

[37] R. M. Sternheimer. Electronic polarizabilities of ions from the hartree-fock wave functions. *Phys. Rev.*, 96:951–968, Nov 1954. doi:10.1103/PhysRev.96.951.

[38] R. Sternheimer. On nuclear quadrupole moments. *Phys. Rev.*, 84:244–253, Oct 1951. doi:10.1103/PhysRev.84.244.

[39] R. M. Sternheimer and H. M. Foley. Nuclear quadrupole coupling in the li_2 molecule. *Phys. Rev.*, 92:1460–1468, Dec 1953. doi:10.1103/PhysRev.92.1460.

[40] Xavier Gonze. Adiabatic density-functional perturbation theory. *Phys. Rev. A*, 52:1096–1114, Aug 1995. doi:10.1103/PhysRevA.52.1096.

[41] Xavier Gonze. Perturbation expansion of variational principles at arbitrary order. *Phys. Rev. A*, 52:1086–1095, Aug 1995. doi:10.1103/PhysRevA.52.1086.

[42] N. David Mermin. Thermal properties of the inhomogeneous electron gas. *Phys. Rev.*, 137:A1441–A1443, Mar 1965. doi:10.1103/PhysRev.137.A1441.

[43] Erich Runge and E. K. U. Gross. Density-functional theory for time-dependent systems. *Phys. Rev. Lett.*, 52:997–1000, Mar 1984. doi:10.1103/PhysRevLett.52.997.

[44] H. J. Xiang, E. J. Kan, Su-Huai Wei, M.-H. Whangbo, and X. G. Gong. Predicting the spin-lattice order of frustrated systems from first principles. *Phys. Rev. B*, 84: 224429, Dec 2011. doi:10.1103/PhysRevB.84.224429.

[45] D. Šabani, C. Bacaksiz, and M. V. Milošević. Ab initio methodology for magnetic exchange parameters: Generic four-state energy mapping onto a heisenberg spin hamiltonian. *Phys. Rev. B*, 102:014457, Jul 2020. doi:10.1103/PhysRevB.102.014457.

[46] Hongjun Xiang, Changhoon Lee, Hyun-Joo Koo, Xingao Gong, and Myung-Hwan Whangbo. Magnetic properties and energy-mapping analysis. *Dalton Trans.*, 42 (4):823–853, 2013. doi:10.1039/C2DT31662E. Publisher: The Royal Society of Chemistry.

[47] E. F. Bertaut. *Magnetism*, volume 3. Academic Press, 1963.

[48] A.I. Liechtenstein, M.I. Katsnelson, V.P. Antropov, and V.A. Gubanov. Local spin density functional approach to the theory of exchange interactions in ferromagnetic metals and alloys. *Journal of Magnetism and Magnetic Materials*, 67(1):65–74, 1987. ISSN 0304-8853. doi:10.1016/0304-8853(87)90721-9.

[49] M. I. Katsnelson and A. I. Lichtenstein. First-principles calculations of magnetic interactions in correlated systems. *Phys. Rev. B*, 61:8906–8912, Apr 2000. doi:10.1103/PhysRevB.61.8906.

[50] Dm. M. Korotin, V. V. Mazurenko, V. I. Anisimov, and S. V. Streltsov. Calculation of exchange constants of the heisenberg model in plane-wave-based methods using the green's function approach. *Phys. Rev. B*, 91:224405, Jun 2015. doi:10.1103/PhysRevB.91.224405.

[51] Xu He, Nicole Helbig, Matthieu J. Verstraete, and Eric Bousquet. Tb2j: A python package for computing magnetic interaction parameters. *Computer Physics Communications*, 264:107938, 2021. ISSN 0010-4655. doi:10.1016/j.cpc.2021.107938.

[52] Nicola Marzari and David Vanderbilt. Maximally localized generalized wannier functions for composite energy bands. *Phys. Rev. B*, 56:12847–12865, Nov 1997. doi:10.1103/PhysRevB.56.12847.

[53] Arash A. Mostofi, Jonathan R. Yates, Giovanni Pizzi, Young-Su Lee, Ivo Souza, David Vanderbilt, and Nicola Marzari. An updated version of wannier90: A tool for obtaining maximally-localised wannier functions. *Computer Physics Communications*, 185(8):2309 – 2310, 2014. ISSN 0010-4655. doi:10.1016/j.cpc.2014.05.003.

[54] Eric Bousquet and Andres Cano. Non-collinear magnetism in multiferroic perovskites. *Journal of physics. Condensed matter : an Institute of Physics journal*, 28:123001, 02 2016. doi:10.1088/0953-8984/28/12/123001.

[55] J. L. Ribeiro and L. G. Vieira. Landau model for the phase diagrams of the orthorhombic rare-earth manganites $r\mathrm{mno}_3$ (r = Eu, gd, tb, dy, ho). *Phys. Rev. B*, 82:064410, Aug 2010. doi:10.1103/PhysRevB.82.064410.

[56] T. Kimura, T. Goto, H. Shintani, K. Ishizaka, T. Arima, and Y. Tokura. Magnetic control of ferroelectric polarization. *Nature*, 426(6962):55–58, 2003. ISSN 00280836. doi:10.1038/nature02018.

[57] T. Kimura. Spiral magnets as magnetoelectrics. *Annual Review of Materials Research*, 37(1):387–413, 2007. doi:10.1146/annurev.matsci.37.052506.084259.

[58] M. Tokunaga, Y. Yamasaki, Y. Onose, M. Mochizuki, N. Furukawa, and Y. Tokura. Novel multiferroic state of $\mathrm{eu}_{1-x}\mathbf{y}_x\mathrm{mno}_3$ in high magnetic fields. *Phys. Rev. Lett.*, 103:187202, Oct 2009. doi:10.1103/PhysRevLett.103.187202.

[59] Nobuo Furukawa and Masahito Mochizuki. Roles of bond alternation in magnetic phase diagram of rmno3. *Journal of the Physical Society of Japan*, 79(3):033708, 2010. doi:10.1143/JPSJ.79.033708.

[60] Andrei Malashevich and David Vanderbilt. First principles study of improper ferroelectricity in tbmno$_3$. *Phys. Rev. Lett.*, 101:037210, Jul 2008. doi:10.1103/PhysRevLett.101.037210.

[61] Taka-hisa Arima. Spin-driven ferroelectricity and magneto-electric effects in frustrated magnetic systems. *Journal of the Physical Society of Japan*, 80(5):052001, 2011. doi:10.1143/JPSJ.80.052001.

[62] Yoshinori Tokura, Shinichiro Seki, and Naoto Nagaosa. Multiferroics of spin origin. *Reports on Progress in Physics*, 77(7):076501, jul 2014. doi:10.1088/0034-4885/77/7/076501.

[63] T. Goto, T. Kimura, G. Lawes, A. P. Ramirez, and Y. Tokura. Ferroelectricity and giant magnetocapacitance in perovskite rare-earth manganites. *Phys. Rev. Lett.*, 92:257201, Jun 2004. doi:10.1103/PhysRevLett.92.257201.

[64] J. Hemberger, F. Schrettle, A. Pimenov, P. Lunkenheimer, V. Yu. Ivanov, A. A. Mukhin, A. M. Balbashov, and A. Loidl. Multiferroic phases of eu$_{1-x}$y$_x$Mno$_3$. *Phys. Rev. B*, 75:035118, Jan 2007. doi:10.1103/PhysRevB.75.035118.

[65] D. O'Flynn, C. V. Tomy, M. R. Lees, A. Daoud-Aladine, and G. Balakrishnan. Multiferroic properties and magnetic structure of sm$_{1-x}$y$_x$mno$_3$. *Phys. Rev. B*, 83:174426, May 2011. doi:10.1103/PhysRevB.83.174426.

[66] I. Fina, V. Skumryev, D. O'Flynn, G. Balakrishnan, and J. Fontcuberta. Phase coexistence and magnetically tuneable polarization in cycloidal multiferroics. *Phys. Rev. B*, 88:100403, Sep 2013. doi:10.1103/PhysRevB.88.100403.

[67] Na Zhang, Shuai Dong, and Jun-Ming Liu. Ferroelectricity generated by spin-orbit and spin-lattice couplings in multiferroic dymno3. *Frontiers of Physics*, 7, 08 2011. doi:10.1007/s11467-011-0225-9.

[68] Xiang Li, Chengliang Lu, Jiyan Dai, Shuai Dong, Yan Chen, Ni Hu, Guangheng Wu, Meifeng Liu, Z. Yan, and Jun-Ming Liu. Novel multiferroicity in gdmno3 thin films with self-assembled nano-twinned domains. *Scientific reports*, 4:7019, 11 2014. doi:10.1038/srep07019.

[69] M. Hepting, M. Minola, A. Frano, G. Cristiani, G. Logvenov, E. Schierle, M. Wu, M. Bluschke, E. Weschke, H.-U. Habermeier, E. Benckiser, M. Le Tacon, and B. Keimer. Tunable charge and spin order in prnio$_3$ thin films and superlattices. *Phys. Rev. Lett.*, 113:227206, Nov 2014. doi:10.1103/PhysRevLett.113.227206.

[70] Gianluca Giovannetti, Sanjeev Kumar, Daniel Khomskii, Silvia Picozzi, and Jeroen van den Brink. Multiferroicity in rare-earth nickelates $r$nio$_3$. *Phys. Rev. Lett.*, 103: 156401, Oct 2009. doi:10.1103/PhysRevLett.103.156401.

[71] Devendra Kumar, K. P. Rajeev, J. A. Alonso, and M. J. Martínez-Lope. Spin-canted magnetism and decoupling of charge and spin ordering in ndnio$_3$. *Phys. Rev. B*, 88:014410, Jul 2013. doi:10.1103/PhysRevB.88.014410.

[72] M. Reehuis, C. Ulrich, K. Prokeš, S. Mat'aš, J. Fujioka, S. Miyasaka, Y. Tokura, and B. Keimer. Structural and magnetic phase transitions of the orthovanadates $r$vo$_3$ (r= dy, ho, er) as seen via neutron diffraction. *Phys. Rev. B*, 83:064404, Feb 2011. doi:10.1103/PhysRevB.83.064404.

[73] S. Miyasaka, Y. Okimoto, M. Iwama, and Y. Tokura. Spin-orbital phase diagram of perovskite-type $r$vo$_3$ (r = rare-earth ion or y). *Phys. Rev. B*, 68:100406, Sep 2003. doi:10.1103/PhysRevB.68.100406.

[74] M. H. Sage, G. R. Blake, C. Marquina, and T. T. M. Palstra. Competing orbital ordering in rVo$_3$ compounds: High-resolution x-ray diffraction and thermal expansion. *Phys. Rev. B*, 76:195102, Nov 2007. doi:10.1103/PhysRevB.76.195102.

[75] M. Skoulatos, S. Toth, B. Roessli, M. Enderle, K. Habicht, D. Sheptyakov, A. Cervellino, P. G. Freeman, M. Reehuis, A. Stunault, G. J. McIntyre, L. D. Tung, C. Marjerrison, E. Pomjakushina, P. J. Brown, D. I. Khomskii, Ch. Rüegg, A. Kreyssig, A. I. Goldman, and J. P. Goff. Jahn-teller versus quantum effects in the spin-orbital material luvo$_3$. *Phys. Rev. B*, 91:161104, Apr 2015. doi:10.1103/PhysRevB.91.161104.

[76] Andrzej M Oleś. Fingerprints of spin–orbital entanglement in transition metal oxides. *Journal of Physics: Condensed Matter*, 24(31):313201, jul 2012. doi:10.1088/0953-8984/24/31/313201.

[77] Carl W. Turner, Malcolm F. Collins, and J.E. Greedan. Magnetic structures of the rare earth orthotitanites rtio3; r = tb, dy, tm and yb. *Journal of Magnetism and Magnetic Materials*, 23(3):265–273, 1981. ISSN 0304-8853. doi:10.1016/0304-8853(81)90046-9.

[78] A. C. Komarek, H. Roth, M. Cwik, W.-D. Stein, J. Baier, M. Kriener, F. Bourée, T. Lorenz, and M. Braden. Magnetoelastic coupling in rTio$_3$ (r = La, Nd, Sm, Gd, Y) investigated with diffraction techniques and thermal expansion measurements. *Phys. Rev. B*, 75:224402, Jun 2007. doi:10.1103/PhysRevB.75.224402.

[79] S. Geller. Crystal structure of gadolinium orthoferrite, gdfeo3. *Journal of Applied Physics*, 24:1236 – 1239, 10 1956. doi:10.1063/1.1742746.

[80] Yusuke Tokunaga, Nobuo Furukawa, Hideaki Sakai, Yasujiro Taguchi, Taka Hisa Arima, and Yoshinori Tokura. Composite domain walls in a multiferroic

perovskite ferrite. *Nature Materials*, 8(7):558–562, 2009. ISSN 14764660. doi:10.1038/nmat2469.

[81] Yamaguchi. Theory of spin reorientation in rare-earth orthochromites and orthoferrites. *Journal of Physics and Chemistry of Solids*, 35(4):479–500, jan 1974. doi:10.1016/S0022-3697(74)80003-X.

[82] Tsuyoshi Yamaguchi and Kunirô Tsushima. Magnetic symmetry of rare-earth orthochromites and orthoferrites. *Physical Review B*, 8(11):5187–5198, 1973. ISSN 01631829. doi:10.1103/PhysRevB.8.5187.

[83] Y. Tokunaga, S. Iguchi, T. Arima, and Y. Tokura. Magnetic-field-induced ferroelectric state in DyFeO3. *Physical Review Letters*, 101(9):3–6, 2008. ISSN 00319007. doi:10.1103/PhysRevLett.101.097205.

[84] Igor A. Kornev, S. Lisenkov, R. Haumont, B. Dkhil, and L. Bellaiche. Finite-temperature properties of multiferroic bifeo3. *Phys. Rev. Lett.*, 99:227602, Nov 2007. doi:10.1103/PhysRevLett.99.227602.

[85] P. Hermet, M. Goffinet, J. Kreisel, and Ph. Ghosez. Raman and infrared spectra of multiferroic bismuth ferrite from first principles. *Phys. Rev. B*, 75:220102, Jun 2007. doi:10.1103/PhysRevB.75.220102.

[86] A. M. Glazer. The classification of tilted octahedra in perovskites. *Acta Crystallographica Section B*, 28(11):3384–3392, 1972. doi:10.1107/S0567740872007976.

[87] Alain Mercy, Jordan Bieder, Jorge Íñiguez, and Philippe Ghosez. Structurally triggered metal-insulator transition in rare-earth nickelates. *Nature Communications*, 8, 11 2017. doi:10.1038/s41467-017-01811-x.

[88] Michael Marcus Schmitt, Yajun Zhang, Alain Mercy, and Philippe Ghosez. Electron-lattice interplay in lamno$_3$ from canonical jahn-teller distortion notations. *Phys. Rev. B*, 101:214304, Jun 2020. doi:10.1103/PhysRevB.101.214304.

[89] T. Arima, T. Goto, Y. Yamasaki, S. Miyasaka, K. Ishii, M. Tsubota, T. Inami, Y. Murakami, and Y. Tokura. Magnetic-field-induced transition in the lattice modulation of colossal magnetoelectric gdmno3 and tbmno3 compounds. *Phys. Rev. B*, 72:100102, Sep 2005. doi:10.1103/PhysRevB.72.100102.

[90] Hong Jian Zhao, Yurong Yang, Wei Ren, Ai Jie Mao, Xiang Ming Chen, and Laurent Bellaiche. Creating multiferroics with large tunable electrical polarization from paraelectric rare-earth orthoferrites. *Journal of Physics Condensed Matter*, 26(47), 2014. ISSN 1361648X. doi:10.1088/0953-8984/26/47/472201.

[91] Pittala Suresh, K. Vijaya Laxmi, A. K. Bera, S. M. Yusuf, Bheema Lingam Chittari, Jeil Jung, and P. S. Anil Kumar. Magnetic ground state of the multiferroic hexagonal LuFe O3. *Physical Review B*, 97(18):1–12, 2018. ISSN 24699969. doi:10.1103/PhysRevB.97.184419.

[92] R. L. White. Review of recent work on the magnetic and spectroscopic properties of the rare-earth orthoferrites. *Journal of Applied Physics*, 40(3):1061–1069, 1969. ISSN 00218979. doi:10.1063/1.1657530.

[93] Louis Néel. Sur l'interprétation des propriétés magnétiques des ferrites de terres rares. *Comptes Rendus Hebdomadaires Des Seances De L Academie Des Sciences*, 239(1):8–11, 1954.

[94] I. E. DZIALOSHINSKII. Thermodynamic Theory of "Weak" Ferromagnetism In Antiferromagnetic Substances. *SOVIET PHYSICS JETP*, 5(6):1259–1272, 1957.

[95] R. M. Bozorth. Origin of weak ferromagnetism in rare-earth orthoferrites. *Physical Review Letters*, 1(10):362–363, 1958. ISSN 00319007. doi:10.1103/PhysRevLett.1.362.

[96] D. Treves and S. Alexander. Observation of antisymmetric exchange interaction in yttrium orthoferrite. *Journal of Applied Physics*, 33(3):1133–1134, 1962. ISSN 00218979. doi:10.1063/1.1728631.

[97] L. Bellaiche, Zhigang Gui, and Igor A. Kornev. A simple law governing coupled magnetic orders in perovskites. *Journal of Physics Condensed Matter*, 24(31):0–6, 2012. ISSN 09538984. doi:10.1088/0953-8984/24/31/312201.

[98] Carlo Weingart, Nicola Spaldin, and Eric Bousquet. Noncollinear magnetism and single-ion anisotropy in multiferroic perovskites. *Phys. Rev. B*, 86:094413, Sep 2012. doi:10.1103/PhysRevB.86.094413.

[99] Hong Jian Zhao, Jorge Íñiguez, Xiang Ming Chen, and L. Bellaiche. Origin of the magnetization and compensation temperature in rare-earth orthoferrites and orthochromates. *Physical Review B*, 93(1):1–5, 2016. ISSN 24699969. doi:10.1103/PhysRevB.93.014417.

[100] Zhiqiang Zhou, Li Guo, Haixia Yang, Qiang Liu, and Feng Ye. Hydrothermal synthesis and magnetic properties of multiferroic rare-earth orthoferrites. *Journal of Alloys and Compounds*, 583:21–31, 2014. ISSN 09258388. doi:10.1016/j.jallcom.2013.08.129.

[101] L. T. Tsymbal, Ya. B. Bazaliy, V. N. Derkachenko, V. I. Kamenev, G. N. Kakazei, F. J. Palomares, and P. E. Wigen. Magnetic and structural properties of spin-reorientation transitions in orthoferrites. *Journal of Applied Physics*, 101(12): 123919, 2007. doi:10.1063/1.2749404.

[102] Evan Constable, D. L. Cortie, Joseph Horvat, R. A. Lewis, Zhenxiang Cheng, Guochu Deng, Shixun Cao, Shujuan Yuan, and Guohong Ma. Complementary terahertz absorption and inelastic neutron study of the dynamic anisotropy contribution to zone-center spin waves in a canted antiferromagnet NdFe O3. *Physical Review B - Condensed Matter and Materials Physics*, 90(5):1–9, 2014. ISSN 1550235X. doi:10.1103/PhysRevB.90.054413.

[103] E. M. Gyorgy, J. P. Remeika, and F. B. Hagedorn. Magnetic behavior of some orthoferrites in the anisotropy change region. *Journal of Applied Physics*, 39(2): 1369–1370, 1968. doi:10.1063/1.1656308.

[104] H. Horner and C. M. Varma. Nature of spin-reorientation transitions. *Phys. Rev. Lett.*, 20:845–846, Apr 1968. doi:10.1103/PhysRevLett.20.845.

[105] K. B. Aring and A. J. Sievers. Role of the ytterbium spins in the spin reorientation in ybfeo3. *Journal of Applied Physics*, 41(3):1197–1198, 1970. ISSN 00218979. doi:10.1063/1.1658877.

[106] Yiming Cao, Maolin Xiang, Weiyao Zhao, Guohua Wang, Zhenjie Feng, Baojuan Kang, Alessandro Stroppa, Jincang Zhang, Wei Ren, and Shixun Cao. Magnetic phase transition and giant anisotropic magnetic entropy change in tbfeo3 single crystal. *Journal of Applied Physics*, 119:063904, 02 2016. doi:10.1063/1.4941105.

[107] J. R. Shane. Resonance frequencies of the orthoferrites in the spin reorientation region. *Phys. Rev. Lett.*, 20:728–732, Apr 1968. doi:10.1103/PhysRevLett.20.728.

[108] R. M. White, R. J. Nemanich, and Conyers Herring. Light scattering from magnetic excitations in orthoferrites. *Phys. Rev. B*, 25:1822–1836, Feb 1982. doi:10.1103/PhysRevB.25.1822.

[109] J. F. Scott. Soft-mode spectroscopy: Experimental studies of structural phase transitions. *Rev. Mod. Phys.*, 46:83–128, Jan 1974. doi:10.1103/RevModPhys.46.83.

[110] Enyu Li, Zhenjie Feng, Baojuan Kang, Jincang Zhang, Wei Ren, and Shixun Cao. Spin switching in single crystal PrFeO3 and spin configuration diagram of rare earth orthoferrites. *Journal of Alloys and Compounds*, 811:152043, 2019. ISSN 09258388. doi:10.1016/j.jallcom.2019.152043.

[111] A S Moskvin and E V Sinitsyn. Antisymmetric exchange and four-sublattice model of orthoferrites. *Fiz. Tverd Tela*, 17(I), 1975.

[112] A. S. Moskvin and I. G. Bostrem. Special features of the excahnge interactions in orthoferrite-orthochromites. *Fiz. Tverd. Tela (Leningrad)*, 19:2616–2626, 1977.

[113] L. T. Tsymbal, Ya B. Bazaliy, G. N. Kakazei, F. J. Palomares, and P. E. Wigen. Magnetic hysteresis in ErFeO 3 near the low temperature erbium ordering transition. *IEEE Transactions on Magnetics*, 44(11 PART 2):2933–2935, 2008. ISSN 00189464. doi:10.1109/TMAG.2008.2001338.

[114] Shuai Dong, Jun Ming Liu, Sang Wook Cheong, and Zhifeng Ren. Multiferroic materials and magnetoelectric physics: Symmetry, entanglement, excitation, and topology. *Advances in Physics*, 64(5-6):519–626, 2015. ISSN 14606976. doi:10.1080/00018732.2015.1114338.

[115] Minhyea Lee. Disordered exchange is biased. *Nature Physics*, 17(4):434–435, 2021. ISSN 17452481. doi:10.1038/s41567-020-01127-6.

[116] I. Fita, A. Wisniewski, R. Puzniak, V. Markovich, and G. Gorodetsky. Exchange-bias reversal in magnetically compensated ErFe O3 single crystal. *Physical Review B*, 93(18):1–5, 2016. ISSN 24699969. doi:10.1103/PhysRevB.93.184432.

[117] I. Fita, A. Wisniewski, R. Puzniak, E. E. Zubov, V. Markovich, and G. Gorodetsky. Common exchange-biased spin switching mechanism in orthoferrites. *Physical Review B*, 98(9):1–7, 2018. ISSN 24699969. doi:10.1103/PhysRevB.98.094421.

[118] L. D. Landau and E. M. Lifshits. The electrodynamics of continuous media (2nd revised and enlarged edition). *Moscow Izdatel Nauka Teoreticheskaia Fizika*, 8, January 1982.

[119] Pierre Curie. Sur la symétrie dans les phénomènes physiques, symétrie d'un champ électrique et d'un champ magnétique. *J. Phys. Theor. Appl.*, 3(1):393–415, 1894. doi:10.1051/jphystap:018940030039300.

[120] W. F. Brown, R. M. Hornreich, and S. Shtrikman. Upper bound on the magnetoelectric susceptibility. *Phys. Rev.*, 168:574–577, Apr 1968. doi:10.1103/PhysRev.168.574.

[121] N. A. Spaldin and R. Ramesh. Advances in magnetoelectric multiferroics. *Nature Materials*, 18(3):203–212, 2019. ISSN 14764660. doi:10.1038/s41563-018-0275-2.

[122] Nicola A. Spaldin. Multiferroics beyond electric-field control of magnetism. *Proceedings of the Royal Society A: Mathematical, Physical and Engineering Sciences*, 476(2233), 2020. ISSN 14712946. doi:10.1098/rspa.2019.0542.

[123] D N Astrov. The magnetoelectric effect in antiferromagnetics. *Journal of Experimental and Theoretical Physics*, 38(3):984–985, 1960. ISSN 0038-5646.

[124] Manfred Fiebig. Revival of the magnetoelectric effect. *Journal of Physics D: Applied Physics*, 38(8), 2005. ISSN 00223727. doi:10.1088/0022-3727/38/8/R01.

[125] K. F. Wang, J. M. Liu, and Z. F. Ren. Multiferroicity: The coupling between magnetic and polarization orders. *Advances in Physics*, 58(4):321–448, 2009. ISSN 00018732. doi:10.1080/00018730902920554.

[126] J. Wang, J. B. Neaton, H. Zheng, V. Nagarajan, S. B. Ogale, B. Liu, D. Viehland, V. Vaithyanathan, D. G. Schlom, U. V. Waghmare, N. A. Spaldin, K. M. Rabe, M. Wuttig, and R. Ramesh. Epitaxial BiFeO3 multiferroic thin film heterostructures. *Science*, 299(5613):1719–1722, 2003. ISSN 00368075. doi:10.1126/science.1080615.

[127] Jacek C. Wojdeł and Jorge Íñiguez. Ab initio indications for giant magnetoelectric effects driven by structural softness. *Phys. Rev. Lett.*, 105:037208, Jul 2010. doi:10.1103/PhysRevLett.105.037208.

[128] Eric Bousquet and Nicola Spaldin. Induced magnetoelectric response in Pnma perovskites. *Physical Review Letters*, 107(19):1–5, 2011. ISSN 10797114. doi:10.1103/PhysRevLett.107.197603.

[129] Temuujin Bayaraa, Yurong Yang, Meng Ye, and L. Bellaiche. Giant linear magnetoelectric effect at the morphotropic phase boundary of epitaxial srbamno3 films. *Phys. Rev. B*, 103:L060103, Feb 2021. doi:10.1103/PhysRevB.103.L060103.

[130] R. O. Cherifi, V. Ivanovskaya, L. C. Phillips, A. Zobelli, I. C. Infante, E. Jacquet, V. Garcia, S. Fusil, P. R. Briddon, N. Guiblin, A. Mougin, A. A. Ünal, F. Kronast, S. Valencia, B. Dkhil, A. Barthélémy, and M. Bibes. Electric-field control of magnetic order above room temperature. *Nature Materials*, 13(4):345–351, 2014. ISSN 14764660. doi:10.1038/nmat3870.

[131] Hans Schmid. Multi-ferroic magnetoelectrics. *Ferroelectrics*, 162(1):317–338, 1994.

[132] Daniel Khomskii. Classifying multiferroics: Mechanisms and effects. *Physics*, 2, 2009. ISSN 1943-2879. doi:10.1103/physics.2.20.

[133] L. C. Chapon, G. R. Blake, M. J. Gutmann, S. Park, N. Hur, P. O. Radaelli, and S. W. Cheong. Structural anomalies and multiferroic behavior in magnetically frustrated TbMn2O5. *Physical Review Letters*, 93(17):10–13, 2004. ISSN 00319007. doi:10.1103/PhysRevLett.93.177402.

[134] M. Kenzelmann, A. B. Harris, S. Jonas, C. Broholm, J. Schefer, S. B. Kim, C. L. Zhang, S. W. Cheong, O. P. Vajk, and J. W. Lynn. Magnetic inversion symmetry breaking and ferroelectricity in TbMnO3. *Physical Review Letters*, 95(8):27–30, 2005. ISSN 00319007. doi:10.1103/PhysRevLett.95.087206.

[135] Jungho Ryu, Shashank Priya, Kenji Uchino, and Hyoun-ee Kim. Magnetoelectric Effect in Composites of Magnetostrictive and Piezoelectric Materials. *Journal of Electroceramics*, 8:107–119, 2002. doi:10.1023/A:1020599728432.

[136] Carlos A. F. Vaz, Jason Hoffman, Charles H. Ahn, and Ramamoorthy Ramesh. Magnetoelectric coupling effects in multiferroic complex oxide composite structures. *Advanced Materials*, 22(26-27):2900–2918, 2010. doi:10.1002/adma.200904326.

[137] Alessandro Stroppa, Martijn Marsman, Georg Kresse, and Silvia Picozzi. The multiferroic phase of DyFeO3: An ab initio study. *New Journal of Physics*, 12, 2010. ISSN 13672630. doi:10.1088/1367-2630/12/9/093026.

[138] La Chen, Tongwei Li, Shixun Cao, Shujuan Yuan, Feng Hong, and Jincang Zhang. The role of 4f-electron on spin reorientation transition of NdFeO 3: A first principle study. *Journal of Applied Physics*, 111(10), 2012. ISSN 00218979. doi:10.1063/1.4716187.

[139] Hong Jian Zhao, L. Bellaiche, Xiang Ming Chen, and Jorge Íñiguez. Improper electric polarization in simple perovskite oxides with two magnetic sublattices. *Nature Communications*, 8:1–11, 2017. ISSN 20411723. doi:10.1038/ncomms14025.

[140] Jung Hoon Lee, Young Kyu Jeong, Jung Hwan Park, Min Ae Oak, Hyun Myung Jang, Jong Yeog Son, and James F. Scott. Spin-canting-induced improper ferroelectricity and spontaneous magnetization reversal in SmFeO3. *Physical Review Letters*, 107(11):1–5, 2011. ISSN 00319007. doi:10.1103/PhysRevLett.107.117201.

[141] C. Y. Kuo, Y. Drees, M. T. Fernández-Díaz, L. Zhao, L. Vasylechko, D. Sheptyakov, A. M.T. Bell, T. W. Pi, H. J. Lin, M. K. Wu, E. Pellegrin, S. M. Valvidares, Z. W. Li, P. Adler, A. Todorova, R. Küchler, A. Steppke, L. H. Tjeng, Z. Hu, and A. C. Komarek. K=0 magnetic structure and absence of ferroelectricity in SmFeO3. *Physical Review Letters*, 113(21):1–5, 2014. ISSN 10797114. doi:10.1103/PhysRevLett.113.217203.

[142] K. Dey, A. Indra, S. Mukherjee, S. Majumdar, J. Strempfer, O. Fabelo, E. Mossou, T. Chatterji, and S. Giri. Natural ferroelectric order near ambient temperature in the orthoferrite HoFeO3. *Physical Review B*, 100(21):1–6, 2019. ISSN 24699969. doi:10.1103/PhysRevB.100.214432.

[143] Taro Nakajima, Yusuke Tokunaga, Yasujiro Taguchi, Yoshinori Tokura, and Taka Hisa Arima. Piezomagnetoelectric Effect of Spin Origin in Dysprosium Orthoferrite. *Physical Review Letters*, 115(19):1–5, 2015. ISSN 10797114. doi:10.1103/PhysRevLett.115.197205.

[144] D. Treves. Studies on orthoferrites at the weizmann institute of science. *Journal of Applied Physics*, 36:1033 – 1039, 04 1965. doi:10.1063/1.1714088.

[145] Ya. B. Bazaliy, L. T. Tsymbal, G. N. Kakazei, A. I. Izotov, and P. E. Wigen. Spin-reorientation in erfeo3: Zero-field transitions, three-dimensional phase diagram, and anisotropy of erbium magnetism. *Phys. Rev. B*, 69:104429, Mar 2004. doi:10.1103/PhysRevB.69.104429.

[146] Alexey Kimel, Andrei Kirilyuk, Artem Tsvetkov, R Pisarev, and Th Rasing. Laser-induced ultrafast spin reorientation in the antiferromagnet tmfeo3. *Nature*, 429: 850–3, 07 2004. doi:10.1038/nature02659.

[147] N. Shamir, H. Shaked, and S. Shtrikman. Magnetic structure of some rare-earth orthochromites. *Phys. Rev. B*, 24:6642–6651, Dec 1981. doi:10.1103/PhysRevB.24.6642.

[148] Bibhuti. B. Dash and S. Ravi. Structural, magnetic and electrical properties of fe substituted gdcro3. *Solid State Sciences*, 83:192–200, 2018. ISSN 1293-2558. doi:10.1016/j.solidstatesciences.2018.07.018.

[149] A. M. Vibhakar, D. D. Khalyavin, P. Manuel, J. Liu, A. A. Belik, and R. D. Johnson. Spontaneous Rotation of Ferrimagnetism Driven by Antiferromagnetic Spin Canting. *Physical Review Letters*, 124(12):127201, 2020. ISSN 10797114. doi:10.1103/PhysRevLett.124.127201.

[150] A.K. Zvezdin and V.M. Matveev. Theory of the magnetic properties of dysprosium orthoferrite. *Zhurnal Ehksperimental*, 77:1076–1086, 1979.

[151] Natalya S. Fedorova, Claude Ederer, Nicola A. Spaldin, and Andrea Scaramucci. Biquadratic and ring exchange interactions in orthorhombic perovskite manganites. *Phys. Rev. B*, 91:165122, 2015. doi:10.1103/PhysRevB.91.165122.

[152] Jacek C Wojdel, Patrick Hermet, Mathias P Ljungberg, Philippe Ghosez, and Jorge Iniguez. First-principles model potentials for lattice-dynamical studies: general methodology and example of application to ferroic perovskite oxides. *Journal of Physics: Condensed Matter*, 25(30):305401, jul 2013. doi:10.1088/0953-8984/25/30/305401.

[153] Pablo Garcia-Fernandez, Jacek C. Wojdel, Jorge Iniguez, and Javier Junquera. Second-principles method for materials simulations including electron and lattice degrees of freedom. *Phys. Rev. B*, 93:195137, May 2016. doi:10.1103/PhysRevB.93.195137.

[154] D. Afanasiev, J. R. Hortensius, B. A. Ivanov, A. Sasani, E. Bousquet, Y. M. Blanter, R. V. Mikhaylovskiy, A. V. Kimel, and A. D. Caviglia. Ultrafast control of magnetic interactions via light-driven phonons. *Nature Materials*, 2021. doi:https://doi.org/10.1038/s41563-021-00922-7.

[155] Jin Tang, Yajiao Ke, Wei He, Xiangqun Zhang, Wei Zhang, Na Li, Yongsheng Zhang, Yan Li, and Zhaohua Cheng. Ultrafast photoinduced multimode antiferromagnetic spin dynamics in exchange-coupled fe/rfeo3 (r = er or dy) heterostructures. *Advanced Materials*, 30(27):1706439, 2018. doi:10.1002/adma.201706439.

[156] D. M. Juraschek, M. Fechner, and N. A. Spaldin. Ultrafast structure switching through nonlinear phononics. *Phys. Rev. Lett.*, 118:054101, Jan 2017. doi:10.1103/PhysRevLett.118.054101.

[157] Rivera, J.-P. A short review of the magnetoelectric effect and related experimental techniques on single phase (multi-) ferroics. *Eur. Phys. J. B*, 71(3):299–313, 2009. doi:10.1140/epjb/e2009-00336-7.

[158] Sae Hwan Chun, Yi Sheng Chai, Yoon Seok Oh, Deepshikha Jaiswal-Nagar, So Young Haam, Ingyu Kim, Bumsung Lee, Dong Hak Nam, Kyung-Tae Ko, Jae-Hoon Park, Jae-Ho Chung, and Kee Hoon Kim. Realization of giant magnetoelectricity in helimagnets. *Phys. Rev. Lett.*, 104:037204, Jan 2010. doi:10.1103/PhysRevLett.104.037204.

[159] Yazhong Wang, Gheorghe L. Pascut, Bin Gao, Trevor A. Tyson, Kristjan Haule, Valery Kiryukhin, and Sang Wook Cheong. Unveiling hidden ferrimagnetism and giant magnetoelectricity in polar magnet Fe2Mo3O8. *Scientific Reports*, 5(July): 1–8, 2015. ISSN 20452322. doi:10.1038/srep12268.

[160] Alireza Sasani, Jorge Iñiguez, and Eric Bousquet. Magnetic phase diagram of rare-earth orthorhombic perovskite oxides. *Phys. Rev. B*, 104:064431, Aug 2021. doi:10.1103/PhysRevB.104.064431.

[161] D. N. Basov, R. D. Averitt, and D. Hsieh. Towards properties on demand in quantum materials. *Nature Materials*, 16(11):1077–1088, 2017. ISSN 14764660. doi:10.1038/NMAT5017.

[162] Lisa Dhar, John A. Rogers, and Keith A. Nelson. Time-resolved vibrational spectroscopy in the impulsive limit. *Chemical Reviews*, 94(1):157–193, 1994. doi:10.1021/cr00025a006.

[163] R. Merlin. Generating coherent thz phonons with light pulses. *Solid State Communications*, 102(2):207–220, 1997. ISSN 0038-1098. doi:10.1016/S0038-1098(96)00721-1. Highlights in Condensed Matter Physics and Materials Science.

[164] Thomas Dekorsy, Gyu Cheon Cho, and Heinrich Kurz. *Coherent phonons in condensed media*, pages 169–209. Springer Berlin Heidelberg, Berlin, Heidelberg, 2000. ISBN 978-3-540-48755-5. doi:10.1007/BFb0084242.

[165] A. A. Maradudin and R. F. Wallis. Ionic raman effect. i. scattering by localized vibration modes. *Phys. Rev. B*, 2:4294–4299, Nov 1970. doi:10.1103/PhysRevB.2.4294.

[166] R. F. Wallis and A. A. Maradudin. Ionic raman effect. ii. the first-order ionic raman effect. *Phys. Rev. B*, 3:2063–2075, Mar 1971. doi:10.1103/PhysRevB.3.2063.

[167] D. L. Mills. Ionic contributions to the Raman tensor of insulators. *Physical Review B*, 35(17):9278–9283, 1987. ISSN 01631829. doi:10.1103/PhysRevB.35.9278.

[168] M. Forst, C. Manzoni, S. Kaiser, Y. Tomioka, Y. Tokura, R. Merlin, and A. Cavalleri. Nonlinear phononics as an ultrafast route to lattice control. *Nature Physics*, 7(11):854–856, 2011. ISSN 17452473. doi:10.1038/nphys2055.

[169] Roman Mankowsky, Michael Först, and Andrea Cavalleri. Non-equilibrium control of complex solids by nonlinear phononics. *Reports on Progress in Physics*, 79(6): 064503, may 2016. doi:10.1088/0034-4885/79/6/064503.

[170] R. Mankowsky, A. Subedi, M. Forst, S. O. Mariager, M. Chollet, H. T. Lemke, J. S. Robinson, J. M. Glownia, M. P. Minitti, A. Frano, M. Fechner, N. A. Spaldin, T. Loew, B. Keimer, A. Georges, and A. Cavalleri. Nonlinear lattice dynamics as a basis for enhanced superconductivity in YBa2Cu3O6.5. *Nature*, 516(729):71–73, 2014. ISSN 14764687. doi:10.1038/nature13875.

[171] M. Forst, R. I. Tobey, S. Wall, H. Bromberger, V. Khanna, A. L. Cavalieri, Y. D. Chuang, W. S. Lee, R. Moore, W. F. Schlotter, J. J. Turner, O. Krupin, M. Trigo, H. Zheng, J. F. Mitchell, S. S. Dhesi, J. P. Hill, and A. Cavalleri. Driving magnetic order in a manganite by ultrafast lattice excitation. *Physical Review B - Condensed Matter and Materials Physics*, 84(24):1–5, 2011. ISSN 10980121. doi:10.1103/PhysRevB.84.241104.

[172] W. Hu, S. Kaiser, D. Nicoletti, C. R. Hunt, I. Gierz, M. C. Hoffmann, M. Le Tacon, T. Loew, B. Keimer, and A. Cavalleri. Optically enhanced coherent transport in YBa2 Cu3 O 6.5 by ultrafast redistribution of interlayer coupling. *Nature Materials*, 13(7):705–711, 2014. ISSN 14764660. doi:10.1038/nmat3963.

[173] D. Fausti, R. I. Tobey, N. Dean, S. Kaiser, A. Dienst, M. C. Hoffmann, S. Pyon, T. Takayama, H. Takagi, and A. Cavalleri. Light-induced superconductivity in a stripe-ordered cuprate. *Science*, 331(6014):189–191, 2011. ISSN 0036-8075. doi:10.1126/science.1197294.

[174] T. F. Nova, A. Cartella, A. Cantaluppi, M. Först, D. Bossini, R. V. Mikhaylovskiy, A. V. Kimel, R. Merlin, and A. Cavalleri. An effective magnetic field from optically driven phonons. *Nature Physics*, 13(2):132–136, 2017. ISSN 17452481. doi:10.1038/nphys3925.

[175] Alaska Subedi. Proposal for ultrafast switching of ferroelectrics using midinfrared pulses. *Physical Review B - Condensed Matter and Materials Physics*, 92(21):1–6, 2015. ISSN 1550235X. doi:10.1103/PhysRevB.92.214303.

[176] R. Mankowsky, A. Von Hoegen, M. Forst, and A. Cavalleri. Ultrafast Reversal of the Ferroelectric Polarization. *Physical Review Letters*, 118(19):1–5, 2017. ISSN 10797114. doi:10.1103/PhysRevLett.118.197601.

[177] T. F. Nova, A. S. Disa, M. Fechner, and A. Cavalleri. Metastable ferroelectricity in optically strained SrTiO3. *Science*, 364(6445):1075–1079, 2019. ISSN 10959203. doi:10.1126/science.aaw4911.

[178] J. W. McIver, B. Schulte, F. U. Stein, T. Matsuyama, G. Jotzu, G. Meier, and A. Cavalleri. Light-induced anomalous Hall effect in graphene. *Nature Physics*, 16 (1):38–41, 2020. ISSN 17452481. doi:10.1038/s41567-019-0698-y.

[179] A. Melnikov, I. Radu, U. Bovensiepen, O. Krupin, K. Starke, E. Matthias, and M. Wolf. Coherent optical phonons and parametrically coupled magnons induced by femtosecond laser excitation of the gd(0001) surface. *Phys. Rev. Lett.*, 91: 227403, Nov 2003. doi:10.1103/PhysRevLett.91.227403.

[180] Sebastian F. Maehrlein, Ilie Radu, Pablo Maldonado, Alexander Paarmann, Michael Gensch, Alexandra M. Kalashnikova, Roman V. Pisarev, Martin Wolf, Peter M. Oppeneer, Joseph Barker, and Tobias Kampfrath. Dissecting spin-phonon equilibration in ferrimagnetic insulators by ultrafast lattice excitation. *Science Advances*, 4(7), 2018. doi:10.1126/sciadv.aar5164.

[181] Ankit S. Disa, Michael Fechner, Tobia F. Nova, Biaolong Liu, Michael Först, Dharmalingam Prabhakaran, Paolo G. Radaelli, and Andrea Cavalleri. Polarizing

an antiferromagnet by optical engineering of the crystal field. *Nature Physics*, 16 (9):937–941, 2020. ISSN 17452481. doi:10.1038/s41567-020-0936-3.

[182] B. Meredig, A. Thompson, H. A. Hansen, C. Wolverton, and A. van de Walle. Method for locating low-energy solutions within dft+u. *Phys. Rev. B*, 82:195128, Nov 2010. doi:10.1103/PhysRevB.82.195128.

[183] B. Amadon, F. Jollet, and M. Torrent. gamma and beta cerium: Lda+u calculations of ground-state parameters. *Phys. Rev. B*, 77:155104, Apr 2008. doi:10.1103/PhysRevB.77.155104.

[184] Boris Dorado, Bernard Amadon, Michel Freyss, and Marjorie Bertolus. Dft+u calculations of the ground state and metastable states of uranium dioxide. *Phys. Rev. B*, 79:235125, Jun 2009. doi:10.1103/PhysRevB.79.235125.

[185] Hua Y. Geng, Ying Chen, Yasunori Kaneta, Motoyasu Kinoshita, and Q. Wu. Interplay of defect cluster and the stability of xenon in uranium dioxide from density functional calculations. *Phys. Rev. B*, 82:094106, Sep 2010. doi:10.1103/PhysRevB.82.094106.

[186] Guillermo Avendaño-Franco and Aldo H. Romero. Firefly algorithm for structural search. *Journal of Chemical Theory and Computation*, 12(7):3416–3428, 2016. doi:10.1021/acs.jctc.5b01157. PMID: 27232694.

[187] Mads Christof Weber, Mael Guennou, Hong Jian Zhao, Jorge Íñiguez, Rui Vilarinho, Abílio Almeida, Joaquim Agostinho Moreira, and Jens Kreisel. Raman spectroscopy of rare-earth orthoferrites RFeO3 (R =La, Sm, Eu, Gd, Tb, Dy). *Physical Review B*, 94(21):1–8, 2016. ISSN 24699969. doi:10.1103/PhysRevB.94.214103.

[188] D. L. Wood, J. P. Remeika, and E. D. Kolb. Optical spectra of rare-earth orthoferrites. *Journal of Applied Physics*, 41(13):5315–5322, 1970. doi:10.1063/1.1658669.

[189] T.-Y. Khim, M. J. Eom, J. S. Kim, B.-G. Park, J.-Y. Kim, and J.-H. Park. Strain control spin reorientation transition in dyfeo3/srtio3 epitaxial film. *Applied Physics Letters*, 99(7):072501, 2011. doi:10.1063/1.3623756.

[190] M. Fechner, A. Sukhov, L. Chotorlishvili, C. Kenel, J. Berakdar, and N. A. Spaldin. Magnetophononics: Ultrafast spin control through the lattice. *Phys. Rev. Materials*, 2:064401, Jun 2018. doi:10.1103/PhysRevMaterials.2.064401.

[191] Dominik M. Juraschek, Prineha Narang, and Nicola A. Spaldin. Phono-magnetic analogs to opto-magnetic effects. *Phys. Rev. Research*, 2:043035, Oct 2020. doi:10.1103/PhysRevResearch.2.043035.

[192] AM Balbashov, AA Volkov, SP Lebedev, AA Mukhin, and A S Prokhorov. High-frequency magnetic properties of dysprosium orthoferrite. *Zh. Eksp. Teor. Fiz*, 88 (March):974–987, 1985.

[193] A. Berton and B. Sharon. Specific heat of dyfeo3 from 1.2°–80°k. *Journal of Applied Physics*, 39(2):1367–1368, 1968. doi:10.1063/1.1656307.

[194] G. Kresse and J. Furthmüller. Efficiency of ab-initio total energy calculations for metals and semiconductors using a plane-wave basis set. *Computational Materials Science*, 6(1):15 – 50, 1996. ISSN 0927-0256. doi:10.1016/0927-0256(96)00008-0.

[195] G. Kresse and J. Furthmüller. Efficient iterative schemes for ab initio total-energy calculations using a plane-wave basis set. *Phys. Rev. B*, 54:11169–11186, Oct 1996. doi:10.1103/PhysRevB.54.11169.

[196] P. E. Blochl. Projector augmented-wave method. *Phys. Rev. B*, 50:17953, 1994. doi:10.1103/PhysRevB.50.17953.

[197] John P. Perdew, Adrienn Ruzsinszky, Gábor I. Csonka, Oleg A. Vydrov, Gustavo E. Scuseria, Lucian A. Constantin, Xiaolan Zhou, and Kieron Burke. Restoring the density-gradient expansion for exchange in solids and surfaces. *Phys. Rev. Lett.*, 100:136406, Apr 2008. doi:10.1103/PhysRevLett.100.136406.

[198] AI Liechtenstein, Viadimir Anisimov, and J Zaanen. Density-functional theory and strong interactions: orbital ordering in mott-hubbard insulators. *Physical Review B*, 52:5467, 1995. doi:10.1103/PhysRevB.52.R5467.

[199] R F L Evans, W J Fan, P Chureemart, T A Ostler, M O A Ellis, and R W Chantrell. Atomistic spin model simulations of magnetic nanomaterials. *Journal of Physics: Condensed Matter*, 26(10):103202, feb 2014. doi:10.1088/0953-8984/26/10/103202.

[200] R. D. King-Smith and David Vanderbilt. Theory of polarization of crystalline solids. *Phys. Rev. B*, 47:1651–1654, Jan 1993. doi:10.1103/PhysRevB.47.1651.

[201] Raffaele Resta. Macroscopic polarization in crystalline dielectrics: the geometric phase approach. *Rev. Mod. Phys.*, 66:899–915, Jul 1994. doi:10.1103/RevModPhys.66.899.

[202] X Gonze, Jean-Michel Beuken, Razvan Caracas, F Detraux, M Fuchs, G.-M Rignanese, L Sindic, Matthieu Verstraete, G Zerah, F Jollet, Marc Torrent, A Roy, Masayoshi Mikami, Ph Ghosez, Jean-Yves Raty, and D.C. Allan. First-principles computation of material properties: The abinit software project. *Computational Materials Science*, 25:478–492, 11 2002. doi:10.1016/S0927-0256(02)00325-7.

[203] Marc Torrent, François Jollet, François Bottin, Gilles Zerah, and X Gonze. Implementation of the projector augmented-wave method in the abinit code: Application to the study of iron under pressure. *Computational Materials Science*, 42: 337–351, 04 2008. doi:10.1016/j.commatsci.2007.07.020.

[204] Kevin F. Garrity, Joseph Bennett, Karin Rabe, and David Vanderbilt. Pseudopotentials for high-throughput dft calculations. *Computational Materials Science*, 81:446–452, 2014. doi:10.1016/j.commatsci.2013.08.053.

[205] M. Topsakal and R. M. Wentzcovitch. Accurate projected augmented wave (PAW) datasets for rare-earth elements (RE = La-Lu). *Computational Materials Science*, 95:263–270, 2014. ISSN 09270256. doi:10.1016/j.commatsci.2014.07.030.

[206] Atsushi Togo and Isao Tanaka. First principles phonon calculations in materials science. *Scripta Materialia*, 108, 06 2015. doi:10.1016/j.scriptamat.2015.07.021.